Title
Engineering ultrastable protein scaffold for the controlled assembly of multifunctional nano-biomaterials

Author
Lim, Samuel

Publication Date
2019

Peer reviewed|Thesis/dissertation

Engineering Ultrastable Protein Scaffold for the Controlled Assembly of Multifunctional Nano-Biomaterials

By

Samuel Lim

A dissertation submitted in partial satisfaction of the

requirements for the degree of

Doctor of Philosophy

in

Chemical Engineering

in the

Graduate Division

of the

University of California, Berkeley

Committee in charge:

Professor Douglas S. Clark, Chair
Professor Markita Landry
Professor John Dueber

Fall 2019

Engineering Ultrastable Protein Scaffold for the Controlled Assembly of Multifunctional Nano-Biomaterials

Samuel Lim

Abstract

Engineering Ultrastable Protein Scaffold for the Controlled Assembly of Multifunctional Nano-Biomaterials

by

Samuel Lim

Doctor of Philosophy in Chemical Engineering

University of California, Berkeley

Professor Douglas S. Clark, Chair

Self-assembling protein templates are of increasing interest in the field of nanoscale fabrication of biomaterials, where precise patterning of functional biomolecules, such as enzymes, is often desired. In particular, protein building blocks can be strategically chosen to exhibit desired functionality, while engineering their assembly allows for the controllable positioning of the subunits. The filamentous protein gamma-prefoldin (γPFD) from the hyperthermophilic archaeon *Methanocaldococcus jannaschii* is an excellent candidate for such a tunable scaffold. Its remarkable stability, unique modularity, and self-assembly into filaments with chaperone activity render it an ideal candidate for the bottom-up construction of novel protein nanostructures.

Our research aimed to construct functional protein biomaterials with precisely controlled nanostructures using γPFD as a building block. We engineered a versatile γPFD-based platform upon which scaffolded biocatalytic systems can be constructed in a customizable fashion. Furthermore, to gain precise positioning of functional molecules on our protein nanostructures, we developed multicomponent protein templates composed of distinct monomers that assemble in repeating orders; fusing different biomolecules to each subunit enabled periodic positioning of multiple functional features along the filament. Finally, we explored γPFD's potential to form cross-linked network, and reported a γPFD-based functional hydrogel with tunable bulk properties. Ultimately, we expect the strategies developed in our lab to provide a γPFD-based biomolecular construction toolkit, which will enhance our ability to fabricate advanced multifunctional nanobiomaterials with novel chemical, catalytic, and structural properties.

Dedication

To my parents, who encouraged me to build Lego blocks out of my imaginations without looking at the instructions.

Twenty years have passed since then and now I build nanostructures from protein blocks, but I still rely on the creativity they nurtured in me as a child.

Contents

List of Figures

List of Tables

Acknowledgments

Many people helped me to make this Ph.D. dissertation possible. First and most importantly, I would like to thank my advisor, Professor Doug Clark for his helpful advices and guidance throughout my course of research. In particular, I would like to thank him for allowing me the right amount of freedom in deciding the topic and scope of my research; I was able to pursue what I found to be interesting, through which I not only fulfilled my scientific curiosity but also learned to become an independent researcher. In addition, I would like to appreciate Professor Markita Landry and Professor John Dueber for their helpful feedbacks and comments, as well as guiding me as the dissertation committee members.

I would like to acknowledge the members of Clark Lab for their helpful discussions and advice. Specifically, I would like to thank Dominic Glover for providing advices and guidances regarding many aspects of protein science, as well as teaching me the experimental techniques. I would also like to thank Dawei Xu for many helpful insights regarding the prefoldin project, Riya Muckom for her expertise in cell culture, and Parry Grewal for his productive comments during the group meeting.

Moreover, I would like to acknowledge the undergraduate assistants, Gi Ahn Jung, Jiwoo Kim and Tiffany Kim, for their amazing works in helping me with many aspects of my experiments - I thank them not just for being highly motivated, hardworking students, but also for being wonderful friends of mine.

I would like to thank my family, mom and dad, for always believing in me and never hesitating to encourage me with their hearts. Also, I am grateful for my friends both in and out of Berkeley, for ensuring me that I am not alone whenever I had encountered difficulties. I am particularly thankful to Seung Joo Lee, for being a great coffee-mate since my first year in Berkeley - hopefully we will follow the paths of the great minds we talked at Caffe Strada.

Finally, I am grateful for the National Science Foundation (NSF) for supporting me through the Graduate Research Fellowship Program (GRFP). I would also like to recognize the U.S. Air Force Office of Scientific Research (AFOSR) for funding our research.

Chapter 1

Self-Assembling Archaeal Protein gamma-Prefoldin (γPFD)

1.1 Abstract

Molecular chaperones promote the correct folding of proteins in aggregation-prone cellular environments by stabilizing the nascent polypeptide chains and providing appropriate folding conditions. gamma-Prefoldin (γPFD) is a filamentous chaperone protein discovered from a deep-sea hyperthermophilic archaeon *Methanocaldococcus jannaschii*. γPFD is thermostable up to 97°C and is known to prevent temperature-dependent aggregation of a wide range of proteins, thereby contributing to its host organism's survivability under harsh conditions. Aside from its native function, γPFD's remarkable stability, unique modularity and self-assembly into filaments with chaperone activity render it an ideal candidate for the bottom-up construbtion of novel protein nanostructures. Using connector proteins engineered to join individual γPFD fibers together at fixed angles and orientations, various nanoscale architectures of defined lengths and shapes have been fabricated.

1.2 Molecular Chaperones and Prefoldins

Molecular chaperones

In living cells, proteins have to be accurately folded into intricate conformations to carry out the diverse functions required of cellular machineries. However, the complex nature of the inter- and intra-protein interactions, as well as the crowding of macromolecules in the cytosol, can cause the misfolding and subsequent aggregation of nascent polypeptide chains [1]. Molecular chaperones are proteins that protect nonnative proteins from undesired aggregation and promote their folding into the correct conformations. Although bacterial and eukaryotic molecular chaperone networks have diverged from each other, the central

scheme involving the ubiquitous heat-shock protein Hsp70 is largely conserved [2]. Hsp70 receives the unfolded protein from the ribosome, facilitates its folding in an ATP-dependent manner, and transfers the polypeptide to downstream chaperones such as chaperonin or Hsp90 if further assistance is required [2]. Thus, Hsp70 is considered an essential component in eukaryotic and bacterial protein folding pathways.

Alternatively, in eukaryotes and archaea, nascent polypeptides can be captured by the different type of chaperone named prefoldin (PFD) and directly transferred to a chaperonin, thus bypassing Hsp70 [2]. The nomenclature "prefoldin" was based on its ability to bind unfolded proteins and deliver them to the chaperonins where they could fold correctly [3]. Unlike Hsp70, PFD is generally not up-regulated by thermal stress [4, 5], and does not require ATP to function [6]. Moreover, many archaeal species do not express Hsp70 [7], and several hyperthermophilic archaea lack other downstream chaperones such as Hsp90, leaving chaperonin as the only element of their downstream protein folding machinery [4]. Such observations strongly suggest that the PFD-chaperonin pathway functions as the critical component of archaeal molecular chaperone systems [8].

Archaeal PFD: a hexameric complex

While eukaryotic PFDs specialize in assisting the folding of cytoskeletal proteins such as actin and tubulin, archaeal PFDs are known to have more general roles in stabilizing a broader range of nascent proteins and preventing thermally-induced aggregation [2, 9, 10]. Such versatility of archaeal PFDs resembles that of Hsp70, accounting for the observation that PFD can replace Hsp70's function as a general chaperone in archaeal species [7].

Most archaeal PFDs share the unique hexameric structure resembling a jellyfish, consisting of two and four α-type and β-type subunits, respectively. The crystal structures of PFDs from *Methanobacterium thermoautotrophicium* and *Pyrococcus horikoshii* suggest that archaeal PFDs share the common jellyfish-like hexameric quaternary structure [11, 12] The overall structure consists of a rigid double β-barrel in the center and six highly flexible coiled-coils protruding from it (Figure 1.1). These "tentacles" provide hydrophobic patches of variable size that can be used to capture a wide variety of nascent proteins, thereby contributing to the substrate diversity accommodated by PFDs [12].

The hexamer comprises two α-type subunits (αPFDs) that form the dimeric core of the jellyfish facsimile, and four additional β-type subunits (βPFDs) bound to the core. αPFD has two β-hairpin domains located between the N- and C-terminal helical coils that form an antiparallel coiled coil; βPFD shares most of the structural features with its counterpart, but has only one β-hairpin linker (Figure 1.2). The β-hairpin domains from each subunit assemble to form a double β-barrel structure with a densely packed hydrophobic core, which provides a rigid backbone onto which the flexible coiled coils are anchored [12].

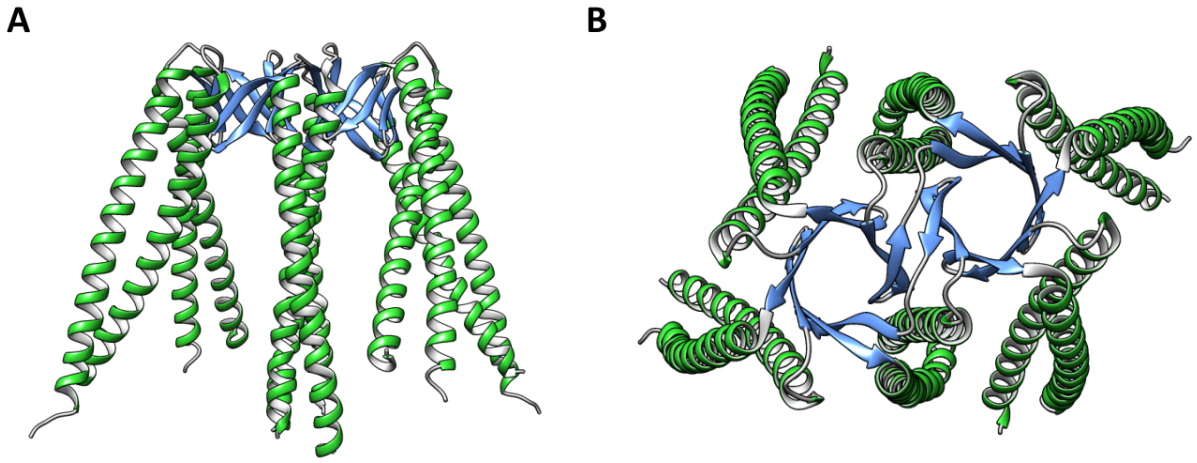

Figure 1.1: Quaternary structure of the PFD hexamer complex from *Methanobacterium thermoautotrophicum* based on the reported crystal structure (front(A) and top(B) view). Green and blue domains represent α helices and β strands, respectively.

Structural variants of archaeal PFD

Although the hexameric hetero-oligomer is the most prevalent form of PFD, homo-oligomeric assemblies have been observed as well. In particular, the crystal structure of the homo-tetramer of *T.* KS-1 PFD β subunit was reported [13]. The observed complex had a jellyfish-like structure similar to the hexameric PFD, with the central "body" formed through the symmetric assembly of the β-hairpin domains from each subunit. The tetramer could only stabilize substrates of relatively small size, probably due to the smaller size of the PFD relative to the conventional hetero-hexamer [13].

Contrary to the homo-oligomerization of the β subunit, assembly of the α subunit is further complicated by the presence of an extra hairpin linker, and can result in the formation of unique structures. The hyperthermophilic archaeon *Methanocaldococcus jannaschii* possesses an extra gene encoding an α subunit that is phylogenetically divergent from most other archaeal αPFDs [14]. Recombinant expression revealed that this unique subunit associates with neither the β subunit nor another α subunit of *M. jannaschii*, and instead forms long filaments up to several microns in length through homo-oligomeric assembly [15]. Considering such distinct characteristics, it was renamed as γPFD.

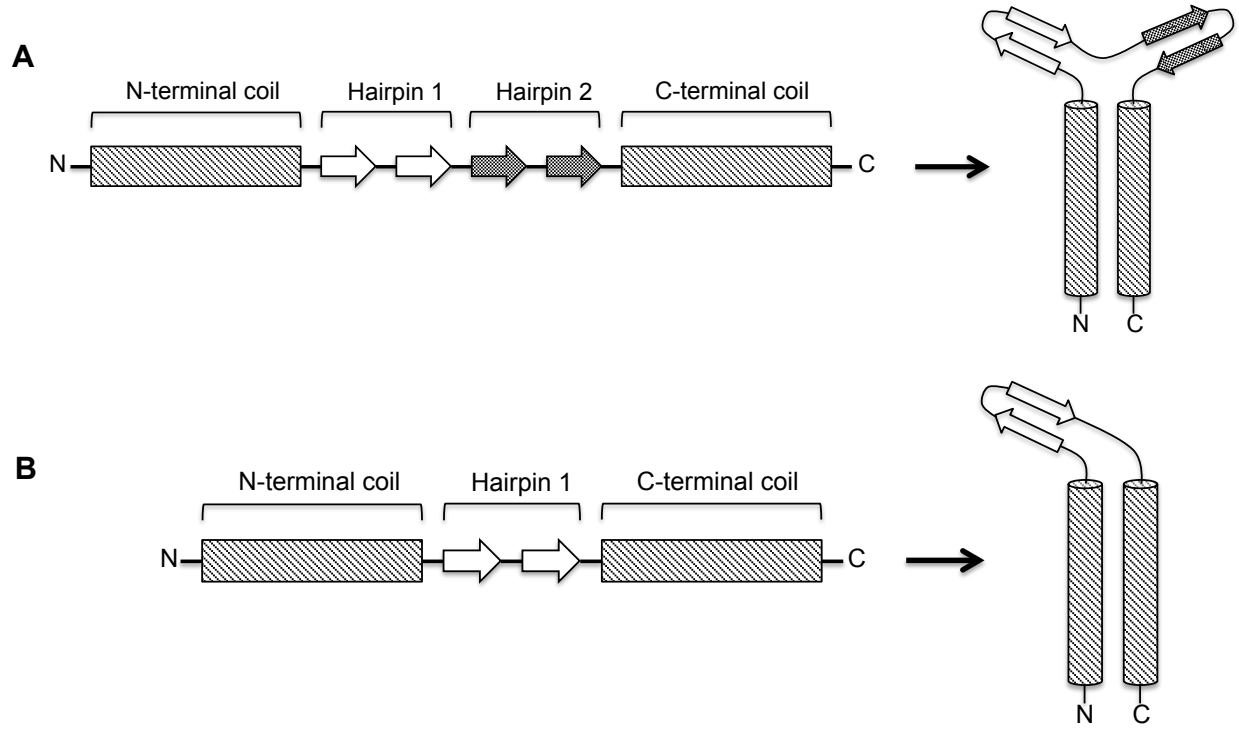

Figure 1.2: Structural comparison of αPFD and βPFD subunits. Secondary structure components of αPFD (A) and βPFD (B) are represented as cartoons where the rectangles and arrows correspond to the helical coils and β strands, respectively. αPFD has four β strands that fold into two separate hairpin structures, whereas βPFD only has two β strands that form a single hairpin.

1.3 Structure and Function of γPFD

Structure of γPFD filament

Cryo-EM observation suggests that the γPFD filament has an "oligomer-of-dimer" structure consisting of dimeric units repeated along the length of the filament (Figure 1.3). The association scheme is analogous to the conventional hexameric PFD assembly: each γPFD dimer accepts two additional γPFD dimers approaching from opposite directions through the β-barrel motif, similar to the way the αPFD dimer core accepts four βPFDs to comprise the hexamer. However, unlike βPFD, which only has one β hairpin, each γPFD has a spare association domain and thus the assembly process can occur repeatedly to extend the oligomer in linear fashion. The resulting γPFD filaments can grow up to several micrometers in length (Figure 1.4).

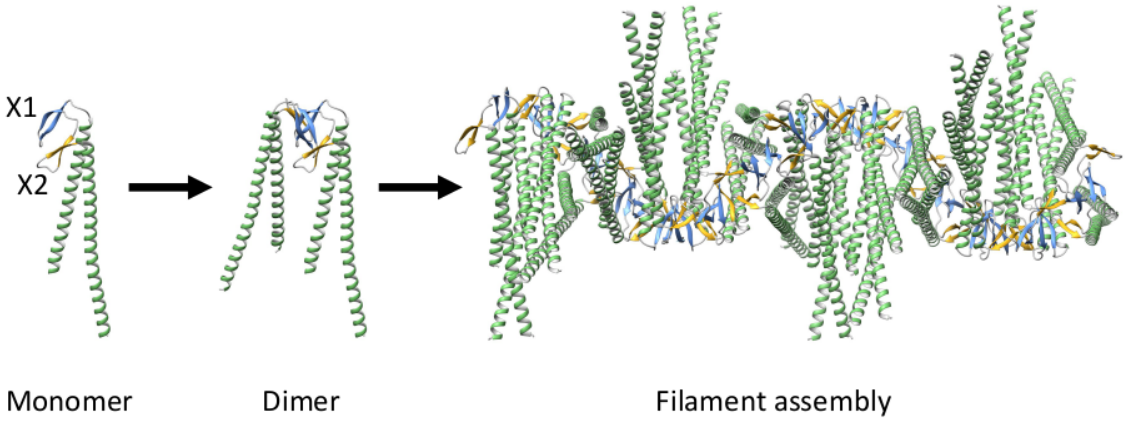

Figure 1.3: Assembly of γPFD filaments. γPFD monomer initially forms a dimer, and the dimers subsequently assemble into filaments through β bundle formation, resulting in an "oligomer-of-dimer" structure. Note that X1 (blue) β sheet is used for the initial dimerization, whereas X2 (yellow) β sheet aids in subsequent oligomerization.

Function of γPFD as a molecular chaperone

Similar to the case of hexameric PFD complex, the coiled coils of γPFD may provide the hydrophobic cavity, allowing it to function as a molecular chaperone through binding non-native proteins. A molecular dynamic study demonstrated that each coiled coil of γPFD is highly flexible, enabling the filament to potentially capture the substrates of varying sizes [16]. In addition, the simulations using unfolded citrate synthase or insulin showed a size dependence between the substrate and the number of interacting coiled coils; to confirm such *in silico* analysis, experimental results confirmed that at least six to eight γPFD subunits are required for γPFD to prevent thermally induced protein aggregations [16].

Interestingly, γPFD is upregulated in response to heat shock unlike other PFD subunits of *M. jannaschii* [15]. Moreover, the secondary structure of γPFD is stable up to 97°C, whereas the αPFD denatures at 85°C [15]. These observations indicate that the presence of γPFD allow the temperature-dependent employment of diverse PFD variants that have different roles [8]. Thus, γPFD may help achieve the greater flexibly in the host organism's ability to respond to a fluctuating environment, thereby contributing to the remarkable survivability of *M. jannaschii* under extremely high temperatures.

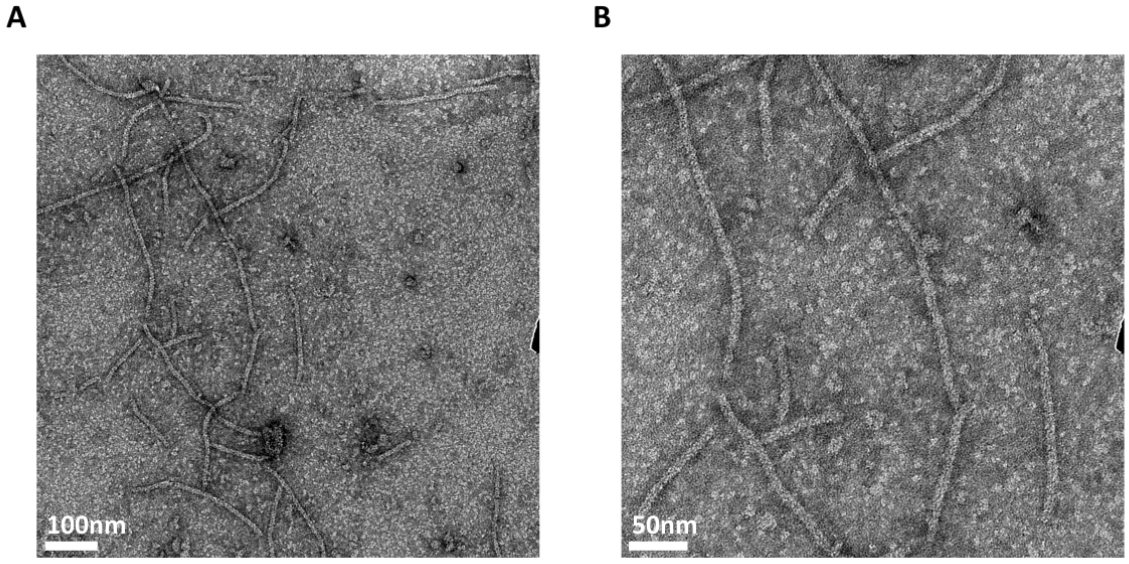

Figure 1.4: TEM images of assembled γPFD filaments under different magnifications. Scale bar = 100nm and 50nm in (A) and (B), respectively.

1.4 Controlled Assembly of γPFD

The unique structure and assembly of PFD complexes offer applications as architectural templates upon which to position functional molecules in complex arrangements. As the β-sheet oligomerization domains of PFDs are separate from the coiled-coil domain, each domain can be modified independently for expanded function [17]. Thus, the filaments of γPFD have been engineered to create a biomolecular construction kit for the fabrication of complex geometrical structures [18].

Controlling γPFD filament length

As an initial step in engineering shapes, control over γPFD filament assembly was achieved through the creation of a capping protein called TERM, which stands for *Thermophilic Extension Resistant Mutant* [19]. This protein was created by mutating one of the β-sheets of γPFD to prevent filament elongation but still enable γPFD binding through the remaining functional β-sheet. Incubating TERM with γPFD during filament assembly results in TERM incorporating into nascent filaments, thereby preventing further elongation. Using this approach, the overall length distribution of filaments can be controlled by varying the molar ratio of TERM to γPFD, with smaller filaments produced when greater amounts of TERM are present [16, 19]. For instance, the 50:1 mixture of γPFD and TERM yielded

filaments with narrow length distribution and average length of 49nm, whereas the wild-type γPFD was 127nm in average length with much broader length distribution [19].

Geometrical assembly of γPFD using connector proteins

The TERM subunit was subsequently used to build connector proteins to join individual filaments together at specific angles (Figure 1.5A) [18]. A two-way connector was created by fusing two TERM subunits together through their helical regions. The use of TERM ensures that γPFD filament growth only occurs in a single direction from each TERM subunit in the fusion. In addition, a three-way connector was created by fusing a trimerization domain called foldon to TERM as a method to join three individual γPFD filaments. These connector proteins were able link multiple filaments into geometrically-defined structures, for example, the assembly of filaments into "pinwheel-like" structures, and self-closing loops(Figure 1.5B, 1.5C).

To gain a greater control over the assembly process, the β-sheet protein-protein interface of γPFD was redesigned to create specific binding partners. Heterodimeric interactions were created in γPFD subunits by replacing one of the β-sheets with helical domains that associate together as heterodimer coiled-coils. The resulting pair of proteins bound each other with high specificity while also functioning as a TERM to incorporate and cap filaments. Inclusion of the foldon trimerization domain enabled the creation of a three-way connector that assembles with filaments capped with the opposing helical sequence into geometrical shapes (Fig. 6). These branched templates could be a first step in creating self-closing structural compartments [20].

1.5 Existing Applications of γPFD Nanostructures

The filamentous and malleable structure of the γPFD makes it a particularly attractive template to build functional materials. Furthermore, the high thermal stability of γPFD may enable its use in a range of processing conditions that are beyond the limits imposed by the labile nature of many biomolecules [21, 22]. The inherent chaperone activity may also confer stabilization to molecules attached to the γPFD templates.

One approach has been to use the natural affinity of the γPFD to various metals ions such as gold, platinum, and silver to create electrically conductive nanowires [22, 23]. Such biotemplating process required high temperature, thereby demonstrating the advantage of using a thermostable scaffold. In addition, γPFD with further enhanced stability was engineered through increasing the hydrophobicity of the α-helices; this variant remained stable at temperatures above 100°C, and allowed for the synthesis of platinum nanowires at unprecedented temperature [23]. Alternatively, gold nanoparticles can be aligned along the γPFD filament and grown into continuous metallic nanowires [18]. These nanowires were

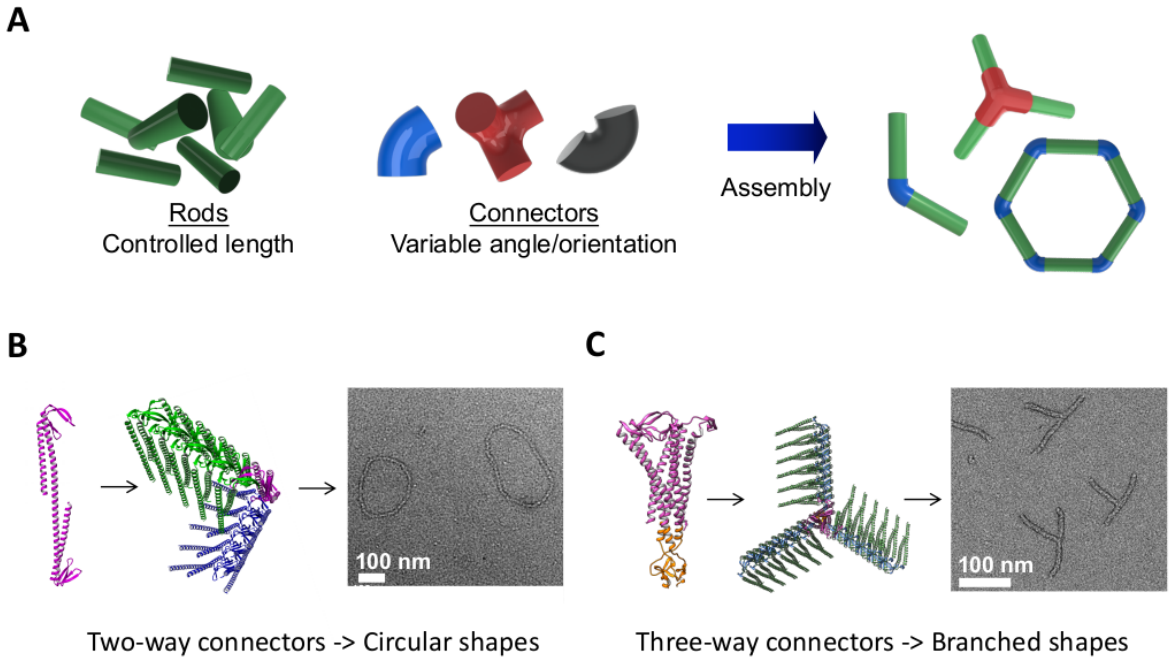

Figure 1.5: Geometrical assembly of γPFD filaments. (A) Cartoon schematic showing the concept of using connector proteins to build γPFD-based nanostructures. (B) Design of the two-way connector and subsequent assembly of closed loop structures. Interlocking filaments and connector parts can be assembled together into ordered shapes as shown by transmission electron microscopy. (C) Design of the three-way connector and subsequent assembly of "pinwheel-like" structures. Scale bars = 100 nm.

significantly more conductive than gold nanowires templated on other biopolymers such as actin or DNA.

1.6 Potential Expansion of γPFD Toolkit

As mentioned in previous sections, γPFD has proven useful as a self-assembling template for the design of nanostructures, and has been applied for a number of applications as well. Yet, there exist a numerous potential ways to further expand this γPFD-based toolkit to achieve more precisely controlled assembly, as well as broader range of applications. Among them, we focused on three major aims as presented below.

Engineering biocatalytic γPFD nanofibers with enhanced performances

γPFD nanowires with diverse functionalities can be formed through incorporating functional cues along the filament. In particular, scaffolding enzymes is a promising biomimetic methodology to create catalytic nanofibers, with potentially improved performances. Thus, we aimed to create a γPFD-based versatile enzyme scaffolding platform that can conveniently immobilize enzymes of interest in customizable combinations.

Patterned assembly of γPFD subunits using novel interaction domains

Due to the homologous nature of the γPFD subunits, their self-assembly occurs without directionality and thus the functional molecules such as enzymes can only be positioned at random along filaments. This limitation can be overcome by the engineering of hetero-oligomeric filaments. We aimed to redesign the β-sheet assembly interfaces of γPFD with helical coils that only bind specific counterparts, allowing the creation of multi-subunit system that assembles in a programmable pattern.

Synthesis of γPFD-based functional hydrogel with tunable properties

Hydrogels are widely used as biomaterials because of their stability under aqueous conditions, versatility in fabrication, and tunable mechanical properties. In particular, protein-based hydrogels have recently gained increasing attention because the peptide motifs or protein domains can be easily incorporated into gel building blocks to engineer the hydrogels with additional functions such as fluorescence or enzymatic activity. We aimed to explore γPFD's potential to form cross-linked network to construct functional biomaterial with tunable bulk properties.

1.7 References

1. Hartl, F. U. & Hayer-Hartl, M. Molecular chaperones in the cytosol: from nascent chain to folded protein. *Science* **295,** 1852–1858 (2002).
2. Balchin, D., Hayer-Hartl, M. & Hartl, F. U. In vivo aspects of protein folding and quality control. *Science* **353,** aac4354 (2016).
3. Vainberg, I. E. *et al.* Prefoldin, a chaperone that delivers unfolded proteins to cytosolic chaperonin. *Cell* **93,** 863–873 (1998).
4. Laksanalamai, P., Whitehead, T. A. & Robb, F. T. Minimal protein-folding systems in hyperthermophilic archaea. *Nature Reviews Microbiology* **2,** 315 (2004).
5. Shockley, K. R. *et al.* Heat shock response by the hyperthermophilic archaeon Pyrococcus furiosus. *Appl. Environ. Microbiol.* **69,** 2365–2371 (2003).
6. Leroux, M. R. *et al.* MtGimC, a novel archaeal chaperone related to the eukaryotic chaperonin cofactor GimC/prefoldin. *The EMBO journal* **18,** 6730–6743 (1999).
7. Leroux, M. R. Protein folding and molecular chaperones in archaea. *Advances in applied microbiology* **50,** 219–277 (2001).
8. Ohtaki, A., Noguchi, K. & Yohda, M. Structure and function of archaeal prefoldin, a co-chaperone of group II chaperonin. *Frontiers in bioscience (Landmark edition)* **15,** 708–717 (2010).
9. Lim, S., Glover, D. J. & Clark, D. S. in *Prefoldins: the new chaperones* 11–23 (Springer, 2018).
10. Sahlan, M. & Yohda, M. in *Thermophilic Microbes in Environmental and Industrial Biotechnology* 375–394 (Springer, 2013).
11. Ohtaki, A. *et al.* Structure and molecular dynamics simulation of archaeal prefoldin: the molecular mechanism for binding and recognition of nonnative substrate proteins. *Journal of molecular biology* **376,** 1130–1141 (2008).
12. Siegert, R., Leroux, M. R., Scheufler, C., Hartl, F. U. & Moarefi, I. Structure of the molecular chaperone prefoldin: unique interaction of multiple coiled coil tentacles with unfolded proteins. *Cell* **103,** 621–632 (2000).
13. Kida, H. *et al.* Structural and molecular characterization of the prefoldin β subunit from Thermococcus strain KS-1. *Journal of molecular biology* **383,** 465–474 (2008).
14. Boonyaratanakornkit, B. B. *et al.* Transcriptional profiling of the hyperthermophilic methanarchaeon Methanococcus jannaschii in response to lethal heat and non-lethal cold shock. *Environmental microbiology* **7,** 789–797 (2005).
15. Whitehead, T. A., Boonyaratanakornkit, B. B., Höllrigl, V. & Clark, D. S. A filamentous molecular chaperone of the prefoldin family from the deep-sea hyperthermophile Methanocaldococcus jannaschii. *Protein science* **16,** 626–634 (2007).

16. Glover, D. J. & Clark, D. S. Oligomeric assembly is required for chaperone activity of the filamentous γ-prefoldin. *The FEBS journal* **282,** 2985–2997 (2015).

17. Whitehead, T. A., Je, E. & Clark, D. S. Rational shape engineering of the filamentous protein γ prefoldin through incremental gene truncation. *Biopolymers: Original Research on Biomolecules* **91,** 496–503 (2009).

18. Glover, D. J., Giger, L., Kim, S. S., Naik, R. R. & Clark, D. S. Geometrical assembly of ultrastable protein templates for nanomaterials. *Nature communications* **7,** 11771 (2016).

19. Whitehead, T. A., Meadows, A. L. & Clark, D. S. Controlling the Self-Assembly of a Filamentous Hyperthermophilic Chaperone by an Engineered Capping Protein. *Small* **4,** 956–960 (2008).

20. Glover, D. J. & Clark, D. S. Protein calligraphy: a new concept begins to take shape. *ACS central science* **2,** 438–444 (2016).

21. Bando, K. *et al.* Bio-supramolecular photochirogenesis with molecular chaperone: enantiodifferentiating photocyclodimerization of 2-anthracenecarboxylate mediated by prefoldin. *Photochemical & Photobiological Sciences* **9,** 655–660 (2010).

22. Slocik, J. M., Kim, S. N., Whitehead, T. A., Clark, D. S. & Naik, R. R. Biotemplated metal nanowires using hyperthermophilic protein filaments. *Small* **5,** 2038–2042 (2009).

23. Glover, D. J., Giger, L., Kim, J. R. & Clark, D. S. Engineering protein filaments with enhanced thermostability for nanomaterials. *Biotechnology journal* **8,** 228–236 (2013).

Chapter 2

Engineering Biocatalytic γPFD Nanofibers with Enhanced Performances

2.1 Abstract

Precisely organized enzyme complexes are often found in nature to support complex metabolic reactions in a highly efficient and specific manner. Scaffolding enzymes on artificial materials has thus gained attention as a promising biomimetic strategy to design biocatalytic systems with enhanced productivity. Although both nucleic acids and proteins have been used as enzyme-positioning templates, the conjugation chemistries are often complex as well as enzyme-specific. This chapter discusses the creation of a versatile scaffolding platform that can immobilize enzymes on customizable γPFD nanofibers. γPFD is genetically engineered to display an array of peptide tags, which can specifically and stably bind enzymes containing the counterpart domain through simple *in vitro* mixing. Successful immobilization of proteins along the filamentous template in tunable density was first verified using fluorescent proteins. Then, two different model enzymes, glucose oxidase (GOX) and horseradish peroxidase (HRP), were used to demonstrate that scaffold attachment could enhance the intrinsic catalytic activity of the immobilized enzymes. We envision the strategy described here may provide a generally applicable methodology for the scaffolded assembly of multi-enzymatic complexes for use in biocatalysis.

2.2 Introduction

Nature often takes advantage of spatially organized enzymatic systems to carry out metabolic reactions in a highly efficient and specific manner [1, 2]. Notably, enzymes can form precisely ordered complexes with the aid of macromolecular scaffolds, as demonstrated

in bacterial cellulosome or plant cytochrome P450 enzymes [3, 4]. Such multi-enzyme clusters have been suggested to facilitate sequential reactions through substrate channeling, during which the intermediate species processed by the upstream enzymes are efficiently transferred to the downstream enzymes due to their high local concentrations, among other possible mechanisms [1, 5, 6].

With continuing interest in biocatalysis as an environmentally-friendly alternative to conventional chemical synthesis, diverse attempts have been made to imitate naturally occurring enzyme complexes to achieve enhanced productivity [7]. Templates based on nucleic acids have been widely employed to co-immobilize enzymes that carry out multi-step reactions, taking advantage of well-established DNA methodologies. Enzyme cascades reconstituted on precisely designed DNA scaffolds with diverse geometries have demonstrated improved catalytic activities and enzyme stabilities [8–10]. However, nucleic acid-based scaffolds are limited by their high cost of synthesis as well as difficulties with integrating enzymes without compromising their bioactivities [11]. Using protein-based scaffolds is an attractive alternative strategy, since proteins can be mass produced from microbial hosts, conveniently engineered through genetic modification, and can spontaneously conjugate with enzymes through specific molecular recognition [12]. Therefore, diverse protein assemblies have been used to support the immobilization of both single-type enzymes and multi-enzyme cascades [13–16]. Yet, the designs used for previously described protein templates were largely case-specific in terms of the type of enzyme employed, the binding stoichiometry, and the conjugation method. Thus, it is desirable to develop a versatile scaffolding platform that can be used to immobilize a broad range of enzymes in convenient and customizable fashion.

Self-assembling proteins such as γPFD are particularly attractive as enzyme immobilization platforms because each building block, genetically engineered to contain specific conjugation sites, can spontaneously form regular structures with known symmetries and dimensions [17, 18]. In this chapter, We report the customizable *in vitro* immobilization of enzymes on a γPFD-based template in a convenient and rapid fashion using a protein-peptide bioconjugation reaction [19]. We first demonstrate controlled scaffolding of proteins along the PFD filament using a fluorescent protein pair, and subsequently use the enzymes glucose oxidase (GOX) and horseradish peroxidase (HRP) to study the effect of scaffolding on their activities.

2.3 Methods

Protein expression and purification

The genes encoding γPFD-SpyTag, mCerulean3-SpyCatcher, mVenus-SpyCatcher and SpyCatcher-Cysteine were synthesized as gBlocks gene fragments (Integrated DNA Technologies) and were inserted into the multiple cloning site of the pET-19b plasmid (Novagen) using the Gibson Assembly (New England Biolabs). The assembled plasmids were trans-

formed into T7 Express competent cells (New England Biolabs), which were grown in 37C in Terrific Broth (IBI Scientific) containing 100 μg mL^{-1} ampicillin until OD 600 reached 0.6.

Protein expression was subsequently induced at 25°C for an additional 15 hours by adding 0.1 mM IPTG. The cells were harvested by centrifugation at 6000 x g for 10 minutes, suspended in phosphate buffer with 50 mM NaH_2PO_4, 100 mM NaCl, pH 8.0, lysed by French press, and additionally centrifuged at 22,000 x g for 50 minutes to collect the soluble lysate. γPFD-SpyTag was expressed without any purification tag, and was purified by hydrophobic interaction chromatography by increasing the NaCl concentration of the lysate to 1 M, passing through a column packed with Toyopearl Butyl 650C resin (TOSOH Bioscience), and eluting with a gradient from 1 M to 100 mM NaCl. All other proteins containing the 6xHis purification tags were purified by binding to Ni-NTA resin (Life Technologies) via gentle inversion for 3 hours at 4°C, washing five times with 50 mM NaH_2PO_4, 20 mM imidazole, 1 M NaCl, pH 8.0, and eluting with a gradient from 20 mM to 1 M imidazole. Purified protein fractions were inspected using SDS-PAGE and SimplyBlue staining (Invitrogen), and the fractions containing the pure proteins were dialyzed overnight against several changes of dialysis buffer (50 mM NaH_2PO_4, 100 mM NaCl, pH 7.4). For storage, the purified proteins were concentrated using Amicon Ultra 15-mL centrifugal columns (30 kDa MWCO, Milipore) and lyophilized for storage at -20°C. For the purification of SpyCatcher-Cysteine, 5 mM DTT was added to all buffers used before the dialysis step.

Assembly of fluorescent proteins on scaffold and FRET assay

Fluorescent proteins were assembled on the scaffold by in vitro mixing of γPFD-SpyTag, mCerulean3-SpyCatcher and mVenus-SpyCatcher. The three components were mixed in phosphate buffer containing 50 mM NaH_2PO_4, 100 mM NaCl, pH 7.4 at varying total fluorescent protein-to-scaffold ratios to achieve a final concentration of 2.5 M for both mCerulean3-SpyCatcher and mVenus-SpyCatcher and 0-160 μM for γPFD-SpyTag. Concentration of each protein was determined by the Bradford assay using BSA standard. After incubation at RT for 1 hour, isopeptide bond formation was confirmed by SDS-PAGE; for detailed analysis of the gels, band intensities were quantified by densitometry using ImageJ. Assembled scaffolds were transferred to a black 96-well plate to measure the fluorescence using a Spectramax M2 plate reader (Molecular Devices). The fluorescence was measured using a 412-nm excitation, 430-nm cutoff filter and emission scan of 450-600 nm. Subsequently, ratiometric FRET was calculated by dividing the 475-nm mCerulean emission peak intensity by the 528-nm mVenus emission peak intensity.

Creation of SpyCatcher-HRP and SpyCatcher-GOX

100 M GOX (from *Aspergillus niger*, Sigma-Aldrich) was first reacted with 2 mM sulfo-SMCC (Abcam) for 1 hour in 50 mM NaH_2PO_4, 100 mM NaCl, pH 7.0 in order to create maleimide-activiated GOX; excess sulfo-SMCC was removed through buffer exchange using

Amicon Ultra 0.5-mL centrifugal columns (30 kDa MWCO, Milipore) following the incubation. Then, 10 μM SpyCatcher-cysteine was incubated with 100 M maleimide-activated GOX for 1 hour in 50 mM NaH_2PO_4, 100 mM NaCl, pH 7.0 to create SpyCatcher-GOX. Subsequently, the reaction mixture was incubated with Ni-NTA resin at 4°C for 1 hour, washed five times at 50 mM NaH_2PO_4, 20 mM imidazole, 1 M NaCl, pH 8.0, and eluted with 50 mM NaH_2PO_4, 1 M imidazole, 1 M NaCl, pH 8.0 to remove excess unreacted GOX. The eluted SpyCatcher-GOX went through buffer exchange at 50 mM NaH_2PO_4, 100 mM NaCl, pH 7.4 and was stored at -20C for further use. Similarly, 100 μM Maleimide-activated HRP (Thermo Fisher Scientific) was incubated with 10 M SpyCatcher-cysteine for 1 hour in 50 mM NaH_2PO_4, 100 mM NaCl, pH 7.0 to create SpyCatcher-HRP; the reaction mixture was purified and stored using the same procedure as SpyCatcher-GOX. The concentrations of GOX and HRP were determined by measuring their absorbances at 280 and 450 nm, respectively, using the extinction coefficients of 2.67 x 105 and 2.61 x 104 M^{-1} cm^{-1}, respectively.

Assembly of enzymes on scaffold and catalytic activity assays

Enzymes were assembled on the scaffold by in vitro mixing of γPFD-SpyTag, SpyCatcher-GOX and/or SpyCatcher-HRP in a buffer containing 50 mM NaH_2PO_4, 100 mM NaCl, pH 7.4 at RT for 1 hour. For the single-type immobilization of each enzyme, 1 μM enzyme was mixed with 0-32 μM of scaffold; for the co-immobilization, 1 μM SpyCatcher-GOX and 1 μM SpyCatcher-HRP were mixed with 0, 16, 32, 64 μM of scaffold. Concentration of scaffold was determined by the Bradford assay using BSA standard, while the concentration of each enzyme was determined by measuring the absorbances at 280 and 450 nm. After incubation at RT for 1 hour, isopeptide bond formation was confirmed by SDS-PAGE; for the detailed analysis of the gel, the intensity of each band was quantified by densitometry using ImageJ. For the HRP activity assay, the final reaction mixture contained 11.3 pM HRP (either free or scaffolded), 0.8 mM TMB and 4 mM H_2O_2 in 50 mM NaH_2PO_4, 100 mM NaCl, pH 5.5 and the absorbance at 652 nm was measured. For the GOX activity assay, the final reaction mixture contained 1 nM GOX (either free or scaffolded), 1 nM free HRP, 0.8 mM TMB and 10 mM H2O2 in 50 mM NaH_2PO_4, 100 mM NaCl, pH 5.5 and the absorbance at 652 nm was measured. For the co-immobilized enzymes, scaffold containing 1 nM of each enzyme was mixed with 0.8 mM TMB and 10 mM H_2O_2. Kinetic assays of HRP and GOX variants were conducted using the same conditions as above, while varying the H2O2 concentration from 0-4 mM for the former and varying the glucose concentration from 2.5-80 mM for the latter. The kinetic constants were determined by constructing Lineweaver-Burk plots.

TEM imaging

Assembled scaffolds were imaged by transmission electron microscopy (TEM) using a Tecnai 12 120KV (FEI Company) and images were captured by a Gatan Ultrascan 1000 digital micrograph. TEM samples were prepared by depositing the scaffolds diluted to the

final concentration of 2.5 M onto 400 mesh carbon/formvar coated copper grids (Electron Microscopy Sciences) and subsequently staining with 2 percent uranyl acetate solution.

2.4 Results

Design of γPFD-based protein scaffolding platform

Our aim was to create a versatile γPFD-based template that can be universally used as a platform to scaffold diverse proteins or enzymes of interest with a minimal need for modification. To this end, direct genetic fusion of the target proteins to the γPFD monomer was undesirable because it can potentially interrupt the enzyme folding or the filament assembly, thereby creating a need for case-specific optimization. Instead, we employed a protein-peptide bioconjugation pair to design a system composed of a common γPFD template displaying an array of peptide binding sites, and the target proteins fused to the recognition domain. Each component can be expressed in a separate batch, without disrupting the enzyme activity or the filament formation, and subsequently assemble together through *in vitro* mixing, with the stoichiometry controlled through varying the amounts of each component in the mixture (Figure 2.1).

To achieve rapid formation of the stable bioconjugation products, we chose the SpyTag-SpyCatcher pair developed by Howarth *et al* [20]. The SpyTag peptide (1.1kDa) and SpyCatcher protein (12kDa) were generated by splitting the isopeptide bond-forming CnaB2 domain of the fibronectin-binding protein (FbaB) from *Streptococcus pyogenes*. The SpyTag and SpyCatcher pair covalently attach spontaneously through the highly specific isopeptide bond formation between the Asp117 residue of SpyTag and the Lys31 residue of SpyCatcher [20, 21]. SpyTag peptide was genetically fused to the C-terminal end of the γPFD monomer to create γPFD-SpyTag that has its binding sites at the tip of each subunit's coiled coil. Since the spacing between the adjacent dimer units in assembled γPFD filaments is known to be 2.3nm, the designed template will display the SpyTag sites at the same intermolecular spacing [22].

Demonstrating controlled immobilization of proteins on γPFD scaffold using a fluorescent protein pair

We verified our γPFD system's ability to scaffold target proteins of interest using the fluorescent proteins mCerulean3 and mVenus containing the SpyCatcher domain. When placed in nanometer-scale proximity (¡10nm), the energy from excited mCerulean3 can directly transfer to mVenus through Forster resonance energy transfer (FRET), resulting in decreased mCerulean3 emission and increased mVenus emission. Since the distance between each subunit in assembled γPFD is close enough to allow for FRET, we expected to observe the corresponding shift in fluorescence emission spectra upon successful co-assembly of both

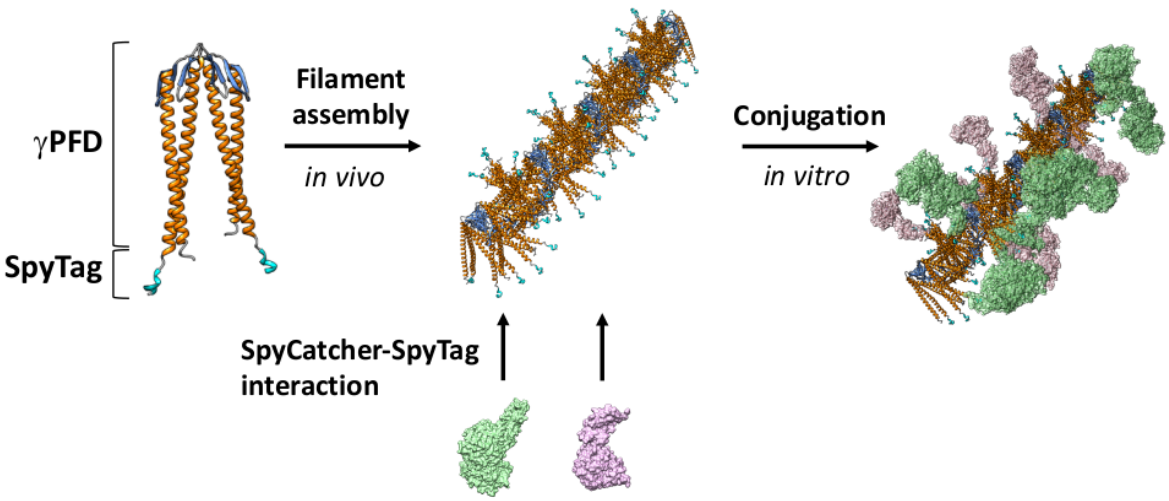

Figure 2.1: Cartoon scheme of the customizable scaffolding of cargo proteins on the γPFD template. Specifically, γPFD subunits genetically fused to SpyTag peptide are expressed and assembled into filaments displaying an array of binding sites *in vivo* within the *E. coli* host cells. Subsequently, any proteins or enzymes containing the SpyCatcher domain can be immobilized on the scaffold through simple *in vitro* mixing.

types of proteins on the γPFD template. Further, increasing the amount of scaffold relative to the fluorescent proteins would lead to sparser positioning and a subsequent decrease in FRET intensity (Figure 2.2A).

The SpyCatcher domain was genetically fused to the C-terminal end of each fluorescent protein to create mCerulean3-SpyCatcher and mVenus-SpyCatcher, which were then expressed and purified from an *E. coli* host; a 6x histidine (6xHis) tag was added to the N-terminus of both proteins to allow for easy purification by metal affinity chromatography. To assemble the fluorescent protein-immobilized templates with tunable density of the displayed proteins, γPFD-SpyTag was mixed with mCerulean3-SpyCatcher and mVenus-SpyCatcher in varying stoichiometry; the ratio of the total fluorescent protein to γPFD-SpyTag was varied from 1:1 to 1:32, while using the equivalent molar amounts of mCerulean3-SpyCatcher and mVenus-SpyCatcher. SDS-PAGE results after 1-hour incubation confirmed binding between the γPFD-SpyTag subunit and the SpyCatcher-bound fluorescent proteins through isopeptide bond formation, as indicated by the upward shifts of mCerulean3-SpyCatcher and mVenus-SpyCatcher bands (Figure 2.2B). Notably, when equal amounts of the fluorescent proteins and the scaffolds were mixed (mCerulean3-SpyCatcher:mVenus-SpyCatcher:γPFD-

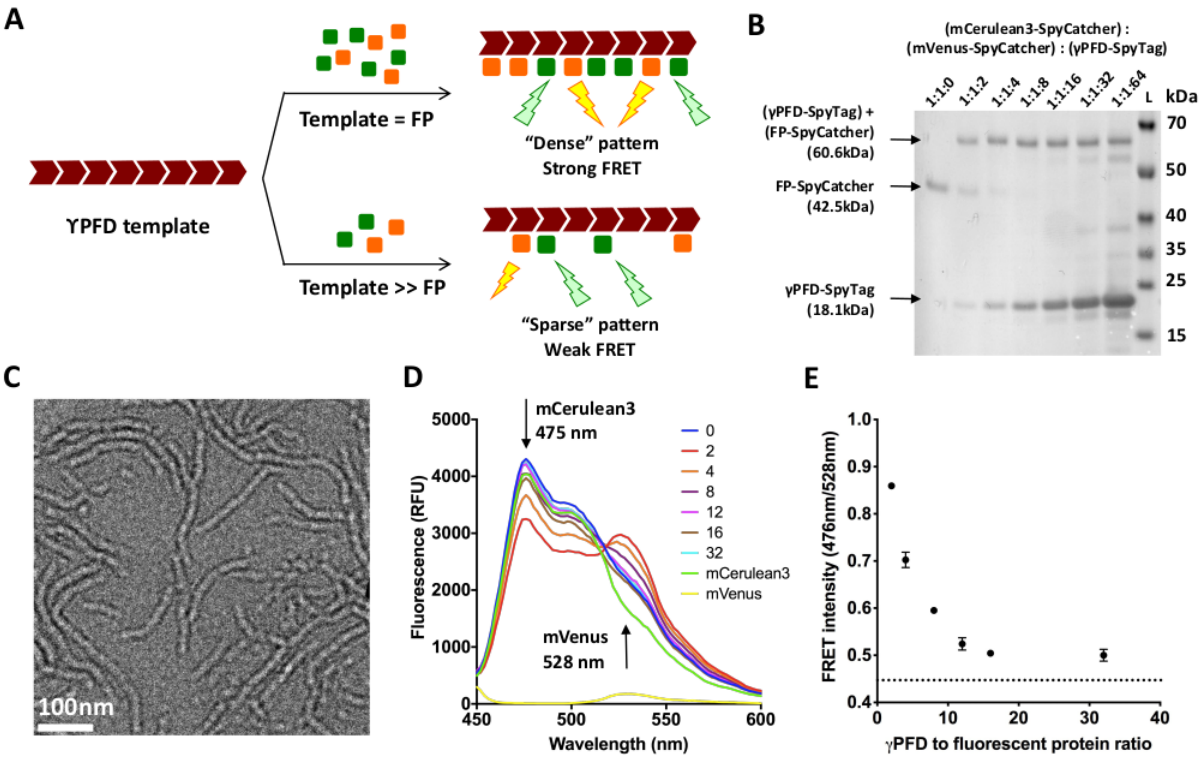

Figure 2.2: (A) Cartoon scheme depicting the tunable density of scaffolded fluorescent proteins (FP) along the γPFD filament. (B) Assembly of mCerulean3-SpyCatcher and mVenus-SpyCatcher on γPFD-SpyTag at varying molar ratios from 1:1:0 to 1:1:64; each well of SDS-PAGE was loaded with 1 μM, 1 μM, and 0-64 μM of the three components, respectively. Attachment via covalent bond formation is verified through the upward shift of the FP-Spycatcher band. At 1:1:2, unbound fluorescent protein-SpyCatcher band is observed. Note that mCerulean3-SpyCatcher and mVenus-SpyCatcher have almost identical molecular weights, and the corresponding band is indicated as FP-SpyCatcher in the figure. (C) TEM image of γPFD-SpyTag filaments assembled with SpyCatcher-mCerulean3 and SpyCatcher-mVenus at 1:1:4 ratio (scale bar = 100 nm). (D) Fluorescence emission spectra of γPFD-fluorescent protein complexes assembled at varying molar ratios. (E) Ratiometric FRET intensity of γPFD-fluorescent protein complexes assembled at varying molar ratios. Dotted line represents the value measured from a control experiment containing free SpyCatcher-bound fluorescent proteins.

SpyTag = 1:1:2), the conjugation efficiency was only ∼70% (densitometry analysis; data not shown). This could be attributed to either the limited binding efficiency of the SpyCatcher-SpyTag system [20], or steric hindrance from dense attachment of the proteins along the filament. On the other hand, when excess scaffold was used, isopeptide bond formation proceeded to completion, indicating that all of the fluorescent proteins were bound to the template. Moreover, the TEM images confirmed that the attachment of cargo proteins does not disrupt the PFD filament structure (Figure 2.2C).

Having confirmed the successful formation of the γPFD-fluorescent protein complexes, we examined the FRET response of each mixture assembled at varying scaffold-to-fluorescent protein ratios. As expected, increasing the amount of the scaffold proteins led to the reduction in FRET intensity as the fluorescent proteins are spaced farther apart on average. When two-fold excess of γPFD-SpyTag was used, a clear decrease in mCerulean3 emission peak at 475 nm and increase in mVenus emission peak at 528 nm was observed upon excitation at 412 nm; such shift was no longer observed as the amount of scaffold was increased up to 32-fold excess, indicating negligible FRET (Figure 2.2D, 2.2E). The above results demonstrate that our γPFD scaffolding system can be used to stably and rapidly co-immobilize multiple proteins, and that the average spacing between the attached proteins can be conveniently controlled by changing the stoichiometry of each component.

Modifying HRP and GOX for conjugation

The applicability of our system for the immobilization of catalytic systems was demonstrated using HRP and GOX as model enzymes. HRP and GOX comprise an enzymatic reaction tandem in which GOX oxidizes glucose to gluconic acid at the expense of converting oxygen to hydrogen peroxide (H_2O_2), and HRP subsequently uses H_2O_2 to oxidize its substrates such as 3,3',5,5'-tetramethylbenzidine (TMB); the distinct blue color of the diimine product allows for the easy quantification of the reaction using colorimetry (Figure 2.3A). Thiol-maleimide chemistry was employed to create the enzymes containing the SpyCatcher domain. The SpyCatcher protein containing a cysteine residue at the C-terminal end and a 6xHis tag at the N-terminal end was genetically created, expressed and purified; since there is no cysteine residue in native SpyCatcher, the engineered C-terminal end will be the only possible reaction site. Maleimide-activated GOX was generated by reacting GOX with the bifunctional linker sulfosuccinimidyl 4-(N-maleimidomethyl) cyclohexane-1-carboxylate (sulfo-SMCC), which converts amine residues on the enzyme surface to maleimide motifs. Maleimide-activated HRP, generated using the same chemistry, was commercially available and used as purchased. Subsequently, SpyCatcher-HRP and SpyCatcher-GOX were created by reacting thiol-containing SpyCatcher and maleimide-activated enzymes (Figure 2.3B). In order to minimize the conjugation of multiple SpyCatcher domains to a single enzyme, 10-fold molar excess of the maleimide-activated enzymes was used. The conjugation products were then purified using Ni-NTA resin, which selectively binds the desired fusion enzymes containing the SpyCatcher domain with an N-terminal 6x His tag.

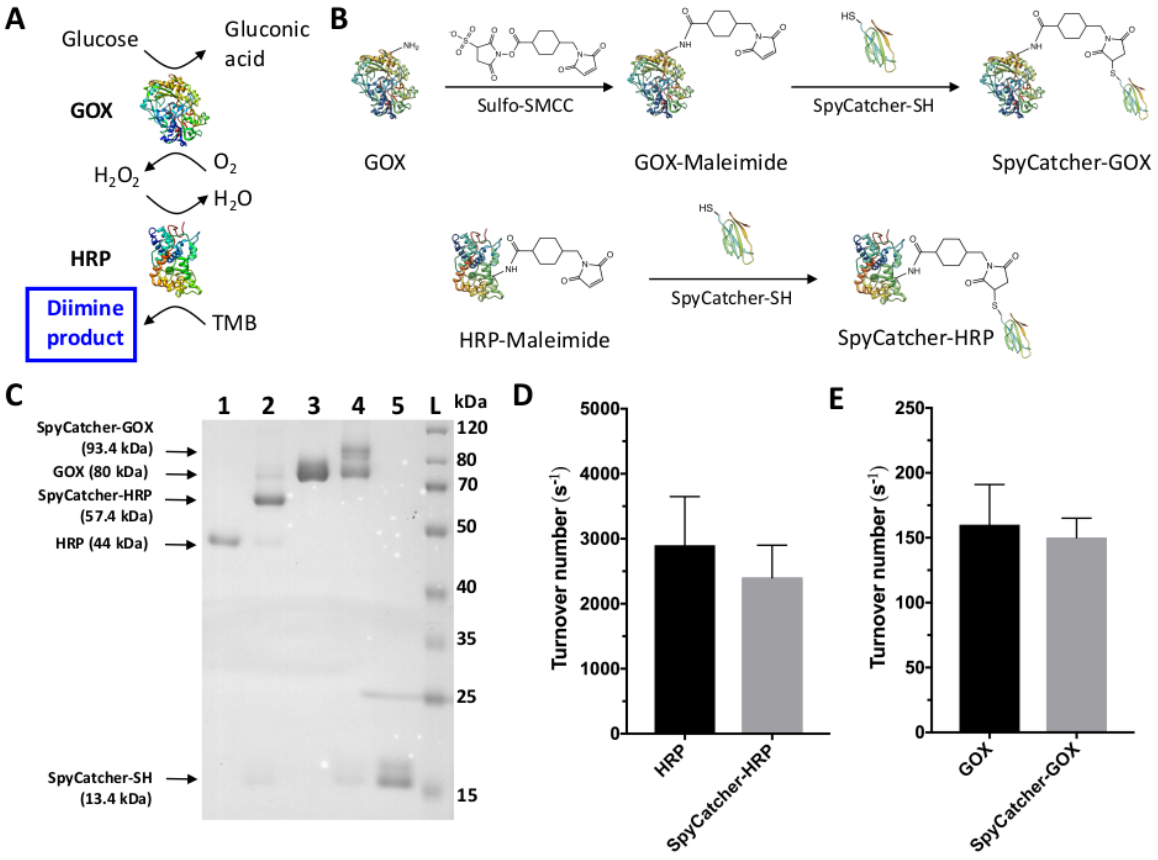

Figure 2.3: (A) Schematic showing the GOX-HRP sequential reaction. (B) Schematic showing each step required to create SpyCatcher-GOX (top) and SpyCatcher-HRP (bottom) (C) SDS-PAGE showing unmodified HRP (lane 1), SpyCatcher-HRP (lane 2), unmodified GOX (lane 3), SpyCatcher-GOX (lane 4) and SpyCatcher-cysteine (lane 5); each lane was loaded with 2 μM of protein. Note that SpyCatcher-GOX showed two bands corresponding to SpyCatcher-GOX and unmodified GOX, indicating that most of the GOX dimers had been modified to contain only one SpyCatcher domain. (D) Comparison of turnover numbers (k_{cat}) of HRP and SpyCatcher-HRP. (E) Comparison of turnover numbers (k_{cat}) of GOX and SpyCather-GOX. All of the experiments in (d) and (e) were performed at least three times, and the error bars represent the SD.

SDS-PAGE showed upward band shifts indicative of successful conjugation for both HRP and GOX (Figure 2.3C). SpyCatcher-GOX showed two bands of almost the same intensity corresponding to SpyCatcher-GOX and unmodified GOX (densitometry analysis; data not shown), indicating that most GOX dimers had been modified to contain only one SpyCatcher domain; such dimers composed of one modified monomer and one unmodified monomer would dissociate under the denaturing conditions of SDS-PAGE and yield two bands with the different molecular weights observed.

The effect of SpyCatcher attachment on the catalytic activity of each enzyme was determined by kinetic measurements. The turnover number (k_{cat}) was 2,900 ± 800 s^{-1} and 2,400 ± 500 s^{-1} for HRP and SpyCatcher-HRP, respectively, whereas no significant change in K_M was observed (0.9 ± 0.2 mM and 1.0 ± 0.2 mM for HRP and SpyCatcher-HRP, respectively; Figure 2.3D, S2). The kinetics of GOX were measured in a coupled reaction with HRP considering that the former is rate limiting if equivalent amounts are used, and the latter is easier to quantify through the colorimetric method. The turnover number and KM were 160 ± 30 s^{-1} and 21 ± 4 mM, respectively, for GOX, and 150 ± 20 s^{-1} and 21 ± 2 mM, respectively, for SpyCatcher-GOX, indicating that the catalytic activity of GOX was not affected by the addition of SpyCatcher (Figure 2.3e, S3a). Furthermore, the turnover number of GOX was smaller than that of HRP by an order of magnitude, confirming the expectation that glucose oxidation is the rate-limiting step in the GOX-HRP reaction cascade. Overall, the above results verified that addition of the SpyCatcher domain had at most only a minor effect on the activities of HRP and GOX.

Effect of scaffolding on catalytic activity of HRP

The γPFD-SpyTag template enables the immobilization of either GOX or HRP individually, as well as their simultaneous co-immobilization on the same filament scaffold. Thus, we separately evaluated the effect of attaching each enzyme to γPFD and the effect of positioning sequential enzymes in proximity.

Conjugation of SpyCatcher-HRP to the γPFD-SpyTag template was verified using enzyme-to-scaffold ratios ranging from 1:1 to 1:32. SDS-PAGE showed almost complete attachment of SpyCatcher-HRP to the scaffold upon 1 hour of incubation, as demonstrated by the upward protein-band shifts, when 8-fold or higher stoichiometric excess of γPFD-SpyTag was used (Figure 2.4A). At lower ratios, incomplete conjugation was observed as indicated by the presence of remaining unbound SpyCatcher-HRP bands. Densitometry analysis of the SDS-PAGE gel supported the above observations (Figure S2.4A). By comparison, the fluorescent proteins required only a two-fold excess of γPFD-SpyTag to achieve complete conjugation. It is possible that the larger size of the HRP enzyme compared to that of the fluorescent proteins imposed higher steric limits that only allowed relatively sparser positioning of SpyCatcher-HRP along the filament. In addition, the TEM image demonstrated that the enzyme attachment did not disrupt the filament structure (Figure 2.4B).

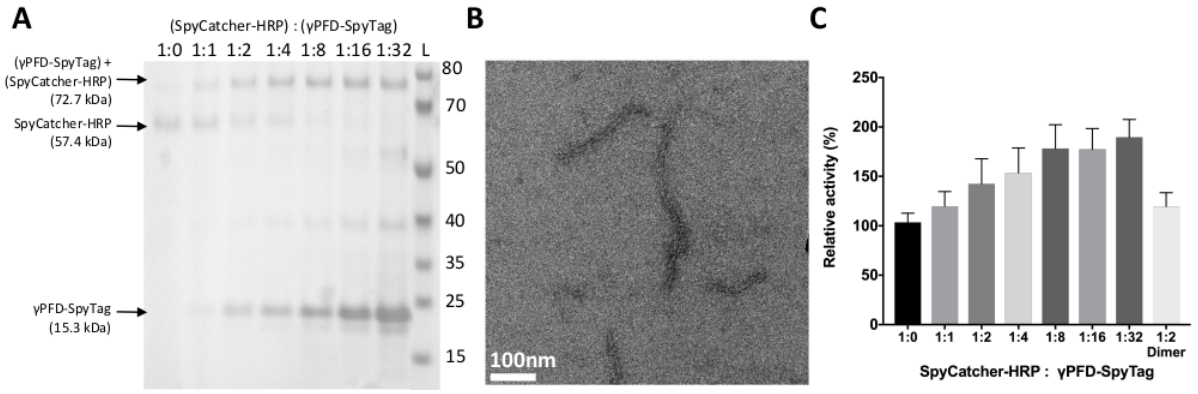

Figure 2.4: Scaffolding of SpyCatcher-HRP and its effect on catalytic activity. (A) Assembly of SpyCatcher-HRP on γPFD-SpyTag at varying molar ratios from 1:0 to 1:32; each lane was loaded with 1 μM of SpyCatcher-HRP and 0-32 μM of γPFD-SpyTag. Attachment via covalent bond formation is verified through the upward shift of the SpyCatcher-HRP band. Note that complete conjugation is observed at a ratio of 1:8 or higher. (B) TEM image of γPFD-SpyTag filaments assembled with SpyCatcher-HRP at 1:8 ratio (scale bar = 100 nm). (C) Comparison of relative specific catalytic activities of SpyCatcher-HRP assembled with γPFD-SpyTag at varying molar ratios from 1:0 to 1:32, or with dimeric γPFD-SpyTag at 1:2 ratio. Activities were measured in a reaction mixture containing 11.3 pM SpyCatcher-HRP enzyme, 0.8 mM TMB and 4 mM H_2O_2 in 50 mM NaH_2PO_4, 100 mM NaCl, pH 5.5. 100% relative activity corresponds to the activity of free SpyCatcher-HRP. The error bars represent the standard deviation (SD) from at least three independent experiments.

Subsequently, we compared the activities of γPFD-HRP complexes assembled at varying stoichiometric ratios, using 11.3 pM of SpyCatcher-HRP, 0.8 mM TMB and 4 mM H_2O_2. For the templates assembled at enzyme-to-scaffold ratios of 1:8, 1:16 and 1:32, at which all the enzymes were conjugated to the scaffold, an $\sim$80% increase of activity was observed; the enhancement was smaller at lower stoichiometric ratios (Figure 2.4C). These results demonstrated that the scaffolding of SpyCatcher-HRP on γPFD-SpyTag enhanced the enzyme's catalytic activity. Further, the extent of enhancement remained roughly constant as the enzyme-to-scaffold ratio increased from 1:8 to 1:32, indicating that positioning SpyCatcher-HRP enzymes farther from each other has an insignificant effect. The smaller increase of activity at lower enzyme-to-scaffold ratios is likely due to incomplete conjugation of SpyCatcher-HRP to γPFD-SpyTag. As a control experiment, HRP enzymes without the SpyCatcher domain were mixed with γPFD-SpyTag at varying stoichiometric ratios from 1:1 to 1:32. Although modest increases in activity between 10% to $\sim$25% were observed, the enhancement factors observed upon adding HRP were smaller than for SpyCatcher-

HRP at all enzyme-to-scaffold ratios examined, indicating that direct conjugation of the enzyme to the γPFD template plays an important role in improving the catalytic activity of SpyCatcher-HRP (Figure S2.5A).

We also investigated whether conjugating enzymes to a γPFD dimeric subunit can improve enzymatic activity in a manner similar to the filamentous scaffold. We have described previously a variant of γPFD that only assembles as a dimer (TERM as mentioned in previous section). We genetically fused SpyTag to the C-terminal end of this variant; once expressed, the assembled dimer could bind up to two SpyCatcher-modified enzymes. When a two-fold excess of dimeric γPFD-SpyTag was mixed with SpyCatcher-HRP, complete conjugation was observed via SDS-PAGE (Figure S2.6A). Rate measurements revealed that attaching SpyCatcher-HRP to the γPFD-SpyTag dimer leads to a relatively small increase (∼20%) in activity, again highlighting the need for the filamentous scaffold to achieve maximum activity enhancement.

Effect of scaffolding on catalytic activity of GOX

In a similar manner, we conjugated SpyCatcher-GOX to the γPFD-SpyTag scaffold and investigated the subsequent effect on catalytic activity. SDS-PAGE confirmed the extent of conjugation between the two components at ratios from 1:1 to 1:32. When 4-fold or higher stoichiometric excess of scaffold was used, the band corresponding to SpyCatcher-GOX shifted upward, indicating complete conjugation (Figure 2.5A). In contrast, unbound SpyCatcher-GOX was evident at lower ratios of 1:1 and 1:2. Densitometry analysis of the SDS-PAGE gel (Figure S4b) confirmed these visual observations. As with SpyCatcher-HRP, the filaments were undisturbed by attachment of the enzyme, as shown by the TEM image (Figure 2.5B).

We then assembled SpyCatcher-GOX and γPFD-SpyTag at varying stoichiometric ratios and measured the resulting activities. When the enzymes and the scaffolds were assembled at ratios of 1:4, 1:8, 1:16 and 1:32, all of the enzyme was bound to the template (Figure 2.5C) and its activity was enhanced by ∼50%. At ratios of 1:1 and 1:2, the increase in activity was smaller, which could be due to incomplete conjugation. In addition, no enhancement of activity was observed in a control experiment, in which GOX enzymes without SpyCatcher were mixed with γPFD-SpyTag at varying ratios from 1:1 to 1:32 (Figure S2.5B). These results confirm the importance of scaffolding and the insignificance of inter-enzyme spacing in the enhancement effect. Moreover, attaching SpyCatcher-GOX to the dimeric γPFD-SpyTag (at a molar ratio 1:2, with complete conjugation verified through SDS-PAGE; Figure S2.6B) led to a ∼25% increase in activity, implicating the filamentous template's role in the greater catalytic activity. It is noteworthy that the overall kinetic effects of scaffolding observed for GOX were similar to those observed for HRP.

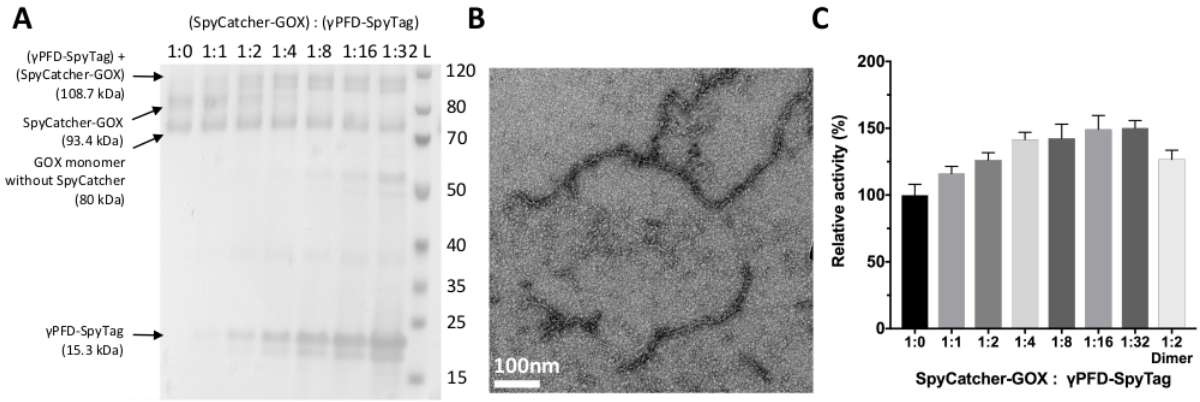

Figure 2.5: Scaffolding of SpyCatcher-GOX and its effect on catalytic activity. (A) Assembly of SpyCatcher-GOX on γPFD-SpyTag at varying molar ratios from 1:0 to 1:32; each lane was loaded with 1 μM of SpyCatcher-GOX and 0-32 μM of γPFD-SpyTag. Attachment via covalent bond formation is verified through the upward shift of the band corresponding to SpyCatcher-GOX. Note that the unmodified monomeric GOX band does not shift, and that complete conjugation is observed at ratio of 1:4 or higher. (B) TEM image of γPFD-SpyTag filaments assembled with SpyCatcher-GOX at 1:4 ratio (scale bar = 100 nm). (C) Comparison of relative catalytic activities of SpyCatcher-GOX assembled with γPFD-SpyTag at varying molar ratios from 1:0 to 1:32, or with dimeric γPFD-SpyTag at 1:2 ratio. Activities were measured in a reaction mixture containing 1 nM GOX enzyme, 1 nM free HRP, 0.8 mM TMB and 10 mM glucose in 50 mM NaH_2PO_4, 100 mM NaCl, pH 5.5. 100% relative activity corresponds to the activity of free SpyCatcher-GOX. The error bars represent the standard deviation (SD) from at least three independent experiments.

Effect of co-immobilizing HRP and GOX

The dual-enzyme GOX-HRP cascade was constituted on γPFD-SpyTag by mixing in vitro equivalent molar amounts of SpyCatcher-HRP and SpyCatcher-GOX with varying amounts of the scaffold. Considering that SpyCatcher-HRP required at least 8-fold molar excess of γPFD-SpyTag to achieve complete conjugation, we tested the total enzyme (SpyCatcher-HRP + SpyCatcher-GOX)-to-scaffold ratios of 1:8, 1:16 and 1:32. SDS-PAGE verified almost complete conjugation of both enzymes to γPFD-SpyTag filaments (Figure S2.7).

At a 1:8 assembly ratio, the two enzymes will be separated on average by four adjacent γPFD-SpyTag dimer units, which corresponds to the distance of ∼9nm along the filament. However, due to the conformational flexibility of the Gly-Ser linker (GGGSC) connecting SpyCatcher and enzyme domains, the actual inter-enzyme distance may vary. For higher

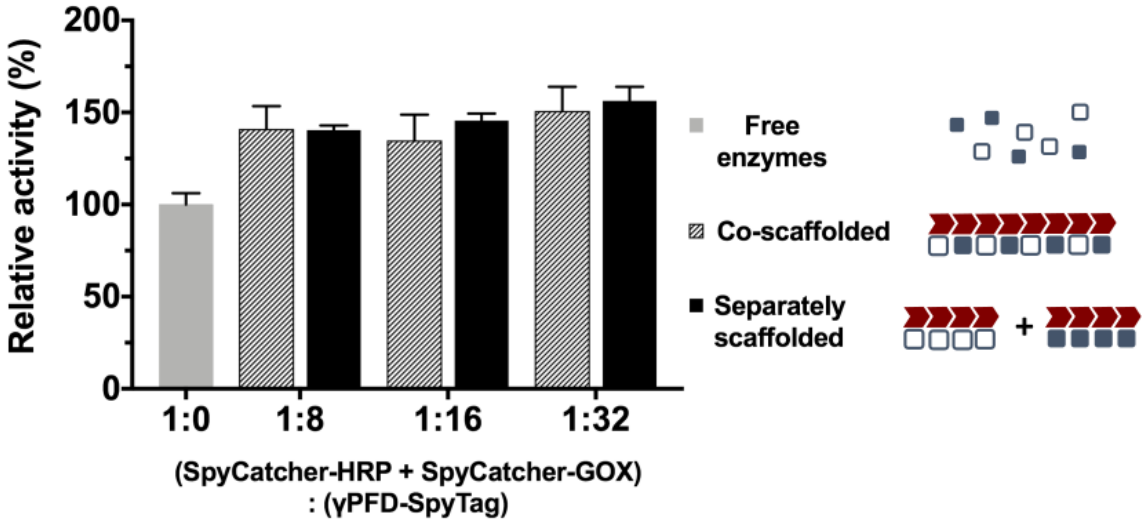

Figure 2.6: Co-immobilizing SpyCatcher-HRP and SpyCatcher-GOX. The figure provides a comparison of overall catalytic activities measured for free, co-immobilized, and separately immobilized SpyCatcher-HRP and SpyCatcher-GOX enzymes. Enzymes were assembled with scaffold at varying ratios of 1:8, 1:16 and 1:32 for both co-immobilized and separately immobilized cases. Activities were measured in a reaction mixture containing 1 nM SpyCatcher-GOX, 1 nM SpyCatcher-HRP, 0.8 mM TMB and 10 mM glucose in 50 mM NaH_2PO_4, 100 mM NaCl, pH 5.5. 100% relative activity corresponds to the activity of free SpyCatcher-GOX and SpyCatcher-HRP. Cartoon scheme is attached to help visualize each condition. The error bars represent the standard deviation (SD) from at least three independent experiments.

assembly ratios of 1:16 and 1:32, the two enzymes will be separated on average by eight and sixteen dimers, respectively, corresponding to distances of ∼18nm and ∼37nm along the filament, although these distances may deviate in a manner similar to the 1:8 ratio case.

The catalytic activities of the dual enzyme cascades were determined toward 10 mM glucose and 0.8 mM TMB by colorimetrically measuring the rate at which the substrate TMB gets converted to the diimine product. As a control, γPFD scaffolds containing only one type of enzyme (γPFD-SpyTag-SpyCatcher-HRP and γPFD-SpyTag-SpyCatcher-GOX complexes) were separately assembled and subsequently mixed together to measure the overall activity; the final reaction mixture contained the same amounts of each enzyme (1 nM) assembled on separate filaments at the same enzyme-to-scaffold ratio compared to the co-immobilized reference experiment, with the only difference being the physical separation of

SpyCatcher-HRP and SpyCatcher-GOX from each other.

All of the assembled enzyme complexes exhibited a ∼50% increase in catalytic activity compared to the non-scaffolded free enzymes (Figure 2.6). Furthermore, at all ratios, activity enhancements of the co-immobilized scaffolds were not significantly different from those of the separately assembled controls (P value ¿ 0.05 from the Student's T-test). Such results suggest that placing SpyCatcher-HRP and SpyCatcher-GOX in physical proximity through co-immobilization does not have a significant effect on the overall activity of the enzymatic cascade, and that the observed increase in activity can be attributed to the enhancement of each enzyme, particularly the rate-limiting SpyCatcher-GOX enzyme, through the scaffolding. Further supporting this view is that the 50% increase in the overall activity of the cascade reaction is consistent with the activity enhancement from scaffolding SpyCatcher-GOX alone, as described in the previous section.

2.5 Discussion

Table 2.1 provides a comprehensive comparison of the kinetic constants of both HRP and GOX enzymes under various conditions including native, SpyCatcher-modified, scaffolded to the filamentous γPFD-SpyTag, and conjugated to the dimeric γPFD-SpyTag. Markedly increased k_{cat} values were obtained for both enzymes upon attachment to the filament, indicating that scaffolding on the γPFD-SpyTag template leads to the enhancements in intrinsic catalytic activities of SpyCatcher-HRP and SpyCatcher-GOX. However, conjugating enzymes to the dimeric γPFD-SpyTag only resulted in a relatively small increase in k_{cat}, revealing that the filamentous structure of the template is required for the full catalytic enhancement effect. In contrast, for both enzymes, K_M values were not significantly affected by the scaffolding and were comparable within experimental errors.

Although it is difficult to provide a clear-cut explanation of the observed kinetic effects of scaffolding enzymes on γPFD-SpyTag, a number of studies have reported enhanced catalysis from immobilizing a single type of enzyme on nanoscale templates [23]. In particular, GOX has exhibited increased enzymatic activity when scaffolded on viral capsids and apoferritin or gold nanoparticles [24–26]. Such improvements in GOX activity have been attributed to favorable conformational changes upon interaction with the support materials [27]. Similarly, HRP immobilized on ZnO nanocrystals showed a clear dependence of catalytic activity on the template morphology, highlighting the effect of microenvironment near the scaffold [28].

It has been shown previously that γPFD can interact with a broad range of nonnative proteins to capture and stabilize them using its coiled coil domains, and that filamentous assembly is required for such activity [29]. Thus, it is possible that γPFD-SpyTag interacts with the attached enzymes in a similar manner to provide favorable conditions for their catalysis. Such speculation also explains the inability of the γPFD-SpyTag dimer to enhance the activity of the bound enzymes as opposed to the filament. However, a detailed mechanistic

	HRP	SpyCatcher-HRP	SpyCatcher-HRP + γPFD scaffold	SpyCatcher-HRP + γPFD dimer
$k_{cat}(s^{-1})$	2,900 ± 800	2,400 ± 500	4,700 ± 900	2,900 ± 1,500
K_M(mM)	0.9 ± 0.2	1.0 ± 0.2	1.1 ± 0.2	0.8 ± 0.2
	GOX	SpyCatcher-GOX	SpyCatcher-GOX + γPFD scaffold	SpyCatcher-GOX + γPFD dimer
$k_{cat}(s^{-1})$	160 ± 30	150 ± 20	210 ± 20	180 ± 10
K_M(mM)	21 ± 4	21 ± 2	18 ± 2	17 ± 2

Table 2.1 Kinetic constants measured for HRP and GOX enzymes under various conditions including native, SpyCatcher-modified, scaffolded to γPFD-SpyTag filament (assembled at enzyme-to-scaffold ratios of 1:8 and 1:4, for HRP and GOX, respectively), and scaffolded to γPFD-Spytag dimer (assembled at 1:2 ratio). For the scaffolded enzymes, the minimum enzyme-to-scaffold ratios required for the complete conjugation were used.

study is required to draw definitive conclusions.

Our scaffolding system allows the positioning of enzymes in nanometer-scale proximity along the filamentous template. Placing sequential enzymes close together has been suggested in some cases to enhance the activity of the reaction cascade through substrate channeling [6, 7]. However, co-immobilizing SpyCatcher-HRP and SpyCatcher-GOX together on γPFD-SpyTag did not further accelerate the sequential reaction beyond the enhancement level observed from the single-type immobilization of each enzyme, indicating no significant channeling had occurred. One possibility is that the distance between the active sites of adjacent SpyCatcher-HRP and SpyCatcher-GOX is not sufficiently close to allow channeling to occur. Furthermore, recent studies suggest that the activity enhancements from co-immobilizing cascade enzymes on scaffolds can be attributed to the favorable microenvironment near the scaffold or the increased local concentration of enzymes through agglomerate formation, rather than the direct proximity between adjacent enzymes [30–32]. Thus, the absence of both channeling and a proximity-dependence of co-immobilized enzyme activity in our system is consistent with the picture emerging from the literature.

It is noteworthy that although the γPFD template can localize a large number of enzymes along the filament in high density, rate enhancement of a multi-step reaction may be limited due to its linear geometry. Because enzymes are aligned in one dimension, reaction intermediates processed by upstream enzymes must diffuse in the direction of the filament in order to benefit from the co-immobilized downstream enzymes. Thus, a system that can scaffold enzymes not only in high density but also in 2-D or 3-D spatial arrangements may facilitate cascade reactions more effectively by increasing the likelihood of randomly diffusing intermediates encountering subsequent enzymes [33]. A promising future direction will be to cross-link the filament templates to induce the formation of larger enzyme-scaffold complexes in which multiple types of enzymes are clustered together in high local density.

We note that a self-assembling protein-based scaffolding system utilizing conjugation chemistry in a manner similar to our work has been reported very recently [34]. In that work, co-immobilizing two sequential dehydrogenase enzymes reduced the time required to reach the final conversion yield of the product, an effect attributed to increased enzyme stability over the 48-hour reaction period. By comparison, here we demonstrate that the γPFD filament template enhances the catalytic activities of the scaffolded HRP and GOX based on their initial reaction kinetics. Such differences indicate that different protein scaffolds can vary in the manner they interact with the immobilized enzymes to affect their performances, and that our γPFD-based scaffolding platform may offer the unique advantage of improving the intrinsic catalytic properties of certain enzymes.

2.6 Conclusion

In this chapter, we described a versatile protein-based platform that allows scaffolding of enzymes in customizable fashion. We chose the ultrastable self-assembling γPFD protein and genetically fused a peptide tag to each subunit to create PFD filaments displaying an array of binding sites; the resulting template could scaffold any protein or enzyme of interest containing a specific binding domain in tunable stoichiometry through *in vitro* mixing. We first verified successful immobilization using fluorescent proteins. A tunable FRET response between the fluorescent proteins bound to the scaffold showed that the target proteins could be placed in high density along the filament, and that their average spacing could be controlled by varying the protein-to-scaffold stoichiometry.

Next, we used two different enzymes, HRP and GOX, to investigate the effect of scaffolding on their catalytic performances; enzyme-to-scaffold ratios were varied to determine the stoichiometry required to achieve complete conjugation for each enzyme. Single-type enzyme immobilization of HRP and GOX produced catalytic activity enhancements of ∼80% and ∼50%, respectively. Detailed kinetic analysis revealed that upon complete scaffolding, k_{cat} values markedly increased whereas K_M remained unchanged for both enzymes. Reconstituting the GOX-HRP reaction cascade by co-immobilizing both enzymes led to ∼50%

activity enhancement relative to the free enzymes; thus, there was no evidence of proximity-dependent substrate channeling between HRP and GOX. Taken together, the results suggest that the filamentous γPFD scafford provides a favorable microenvironment for the bound enzymes, which enhances their intrinsic catalytic activities but does not promote direct channeling of the reaction intermediate between them.

The γPFD-based system provides a robust scaffold for enzyme immobilization along protein nanofibers. In addition, a unique ability of γPFD to interact with diverse protein substrates may improve the intrinsic activity of the bound enzymes, at least in some cases. The γPFD scaffolding platform should thus be generally useful for preparing biocatalytic nanofibers containing single or multiple enzymes aligned in close proximity, with activities that equal or exceed those of the free enzymes.

2.7 References

1. Küchler, A., Yoshimoto, M., Luginbühl, S., Mavelli, F. & Walde, P. Enzymatic reactions in confined environments. *Nature Nanotechnology* **11,** 409 (2016).
2. Conrado, R. J., Varner, J. D. & DeLisa, M. P. Engineering the spatial organization of metabolic enzymes: mimicking nature's synergy. *Current opinion in biotechnology* **19,** 492–499 (2008).
3. Agapakis, C. M., Boyle, P. M. & Silver, P. A. Natural strategies for the spatial optimization of metabolism in synthetic biology. *Nature chemical biology* **8,** 527 (2012).
4. Gou, M., Ran, X., Martin, D. W. & Liu, C.-J. The scaffold proteins of lignin biosynthetic cytochrome P450 enzymes. *Nature plants* **4,** 299 (2018).
5. Castellana, M. *et al.* Enzyme clustering accelerates processing of intermediates through metabolic channeling. *Nature biotechnology* **32,** 1011 (2014).
6. Wheeldon, I. *et al.* Substrate channelling as an approach to cascade reactions. *Nature chemistry* **8,** 299 (2016).
7. Lin, J.-L., Palomec, L. & Wheeldon, I. Design and analysis of enhanced catalysis in scaffolded multienzyme cascade reactions. *Acs Catalysis* **4,** 505–511 (2014).
8. Wilner, O. I. *et al.* Enzyme cascades activated on topologically programmed DNA scaffolds. *Nature nanotechnology* **4,** 249 (2009).
9. Fu, J., Liu, M., Liu, Y., Woodbury, N. W. & Yan, H. Interenzyme substrate diffusion for an enzyme cascade organized on spatially addressable DNA nanostructures. *Journal of the American Chemical Society* **134,** 5516–5519 (2012).
10. Zhao, Z. *et al.* Nanocaged enzymes with enhanced catalytic activity and increased stability against protease digestion. *Nature communications* **7,** 10619 (2016).
11. Pinheiro, A. V., Han, D., Shih, W. M. & Yan, H. Challenges and opportunities for structural DNA nanotechnology. *Nature nanotechnology* **6,** 763 (2011).
12. Glover, D. J. & Clark, D. S. Protein calligraphy: a new concept begins to take shape. *ACS central science* **2,** 438–444 (2016).
13. Dueber, J. E. *et al.* Synthetic protein scaffolds provide modular control over metabolic flux. *Nature biotechnology* **27,** 753 (2009).
14. You, C., Myung, S. & Zhang, Y.-H. P. Facilitated substrate channeling in a self-assembled trifunctional enzyme complex. *Angewandte Chemie International Edition* **51,** 8787–8790 (2012).
15. Liu, F., Banta, S. & Chen, W. Functional assembly of a multi-enzyme methanol oxidation cascade on a surface-displayed trifunctional scaffold for enhanced NADH production. *Chemical Communications* **49,** 3766–3768 (2013).

16. Visser, F., Müller, B., Rose, J., Prüfer, D. & Noll, G. A. Forizymes–functionalised artificial forisomes as a platform for the production and immobilisation of single enzymes and multi-enzyme complexes. *Scientific reports* **6,** 30839 (2016).

17. Luo, Q., Hou, C., Bai, Y., Wang, R. & Liu, J. Protein assembly: Versatile approaches to construct highly ordered nanostructures. *Chemical reviews* **116,** 13571–13632 (2016).

18. Nguyen, P. Q., Botyanszki, Z., Tay, P. K. R. & Joshi, N. S. Programmable biofilm-based materials from engineered curli nanofibres. *Nature communications* **5,** 4945 (2014).

19. Lim, S., Jung, G. A., Glover, D. J. & Clark, D. S. Enhanced Enzyme Activity through Scaffolding on Customizable Self-Assembling Protein Filaments. *Small* **15,** 1805558 (2019).

20. Zakeri, B. *et al.* Peptide tag forming a rapid covalent bond to a protein, through engineering a bacterial adhesin. *Proceedings of the National Academy of Sciences* **109,** E690–E697 (2012).

21. Reddington, S. C. & Howarth, M. Secrets of a covalent interaction for biomaterials and biotechnology: SpyTag and SpyCatcher. *Current opinion in chemical biology* **29,** 94–99 (2015).

22. Glover, D. J., Giger, L., Kim, S. S., Naik, R. R. & Clark, D. S. Geometrical assembly of ultrastable protein templates for nanomaterials. *Nature communications* **7,** 11771 (2016).

23. Ding, S., Cargill, A. A., Medintz, I. L. & Claussen, J. C. Increasing the activity of immobilized enzymes with nanoparticle conjugation. *Current Opinion in Biotechnology* **34,** 242–250 (2015).

24. Patel, A. N. *et al.* Scaffolding of enzymes on virus nanoarrays: effects of confinement and virus organization on biocatalysis. *Small* **13,** 1603163 (2017).

25. Zhang, Y. *et al.* Apoferritin nanoparticle: a novel and biocompatible carrier for enzyme immobilization with enhanced activity and stability. *Journal of Materials Chemistry* **21,** 17468–17475 (2011).

26. Pandey, P. *et al.* Application of thiolated gold nanoparticles for the enhancement of glucose oxidase activity. *Langmuir* **23,** 3333–3337 (2007).

27. Johnson, B. J., Algar, W. R., Malanoski, A. P., Ancona, M. G. & Medintz, I. L. Understanding enzymatic acceleration at nanoparticle interfaces: approaches and challenges. *Nano Today* **9,** 102–131 (2014).

28. Zhang, Y., Wu, H., Huang, X., Zhang, J. & Guo, S. Effect of substrate (ZnO) morphology on enzyme immobilization and its catalytic activity. *Nanoscale research letters* **6,** 450 (2011).

29. Glover, D. J. & Clark, D. S. Oligomeric assembly is required for chaperone activity of the filamentous γ-prefoldin. *The FEBS journal* **282,** 2985–2997 (2015).

30. Idan, O. & Hess, H. Origins of activity enhancement in enzyme cascades on scaffolds. *ACS nano* **7,** 8658–8665 (2013).

31. Chado, G. R., Stoykovich, M. P. & Kaar, J. L. Role of dimension and spatial arrangement on the activity of biocatalytic cascade reactions on scaffolds. *ACS Catalysis* **6,** 5161–5169 (2016).

32. Zhang, Y., Tsitkov, S. & Hess, H. Proximity does not contribute to activity enhancement in the glucose oxidase–horseradish peroxidase cascade. *Nature communications* **7,** 13982 (2016).

33. Lee, H., DeLoache, W. C. & Dueber, J. E. Spatial organization of enzymes for metabolic engineering. *Metabolic engineering* **14,** 242–251 (2012).

34. Zhang, G., Quin, M. B. & Schmidt-Dannert, C. Self-assembling protein scaffold system for easy in vitro coimmobilization of biocatalytic cascade enzymes. *ACS Catalysis* **8,** 5611–5620 (2018).

Appendix

2.A Supporting Figures for Chapter 2

γPFD-SpyTag (18.1 kDa)

MVNEVIDINEAVRAYIAQIEGLRAEIGRLDATIATLRQSLATLKSLKTLGEGKTVLVPVGSIAQVEM
KVEKMDKVVVSVGQNISAELEYEEALKYIEDEIKKLLTFRLVLEQAIAELYAKIEDLIAEAQQTSEEE
KAEEEENEEKAEGSAHIVMVDAYKPTK

Dimeric γPFD-SpyTag (17.9 kDa)

MVNEVIDINEAVRAYIAQIEGLRAEIGRLDATIATLRQSLATLKSLKTLGEGKTVLVPVGSIAQVEM
KVEKMDKVVVAAAAAAAAELEYEEALKYIEDEIKKLLTFRLVLEQAIAELYAKIEDLIAEAQQTSEE
EKAEEEENEEKAEGSAHIVMVDAYKPTK

mCerulean3-SpyCatcher (42.3 kDa)

MGHMHHHHHHGGVSKGEELFTGVVPILVELDGDVNGHKFSVSGEGEGDATYGKLTLKFICTTG
KLPVPWPTLVTTLSWGVQCFARYPDHMKQHDFFKSAMPEGYVQERTIFFKDDGNYKTRAEVK
FEGDTLVNRIELKGIDFKEDGNILGHKLEYNAIHGNVYITADKQKNGIKANFGLNCNIEDGSVQL
ADHYQQNTPIGDGPVLLPDNHYLSTQSKLSKDPNEKRDHMVLLEFVTAAGITLGMDELYKGSG
GGSDYDIPTTENLYFQGAMVDTLSGLSSEQGQSGDMTIEEDSATHIKFSKRDEDGKELAGATME
LRDSSGKTISTWISDGQVKDFYLYPGKYTFVETAAPDGYEVATAITFTVNEQGQVTVNGKATKG
DAHI

mVenus-SpyCatcher (42.5 kDa)

MGHMHHHHHHGGVSKGEELFTGVVPILVELDGDVNGHKFSVSGEGEGDATYGKLTLKLICTTG
KLPVPWPTLVTTLGYGLQCFARYPDHMKQHDFFKSAMPEGYVQERTIFFKDDGNYKTRAEVKF
EGDTLVNRIELKGIDFKEDGNILGHKLEYNYNSHNVYITADKQKNGIKANFKIRHNIEDGGVQLA
DHYQQNTPIGDGPVLLPDNHYLSYQSKLSKDPNEKRDHMVLLEFVTAAGITLGMDELYKGSGG
GSDYDIPTTENLYFQGAMVDTLSGLSSEQGQSGDMTIEEDSATHIKFSKRDEDGKELAGATMEL
RDSSGKTISTWISDGQVKDFYLYPGKYTFVETAAPDGYEVATAITFTVNEQGQVTVNGKATKGD
AHI

SpyCatcher-Cysteine (13.4 kDa)

MGHHHHHHGSAMVDTLSGLSSEQGQSGDMTIEEDSATHIKFSKRDEDGKELAGATMELRDSS
GKTISTWISDGQVKDFYLYPGKYTFVETAAPDGYEVATAITFTVNEQGQVTVNGKATKGGGSC

Figure S2.1: Amino acid sequences of the recombinant proteins

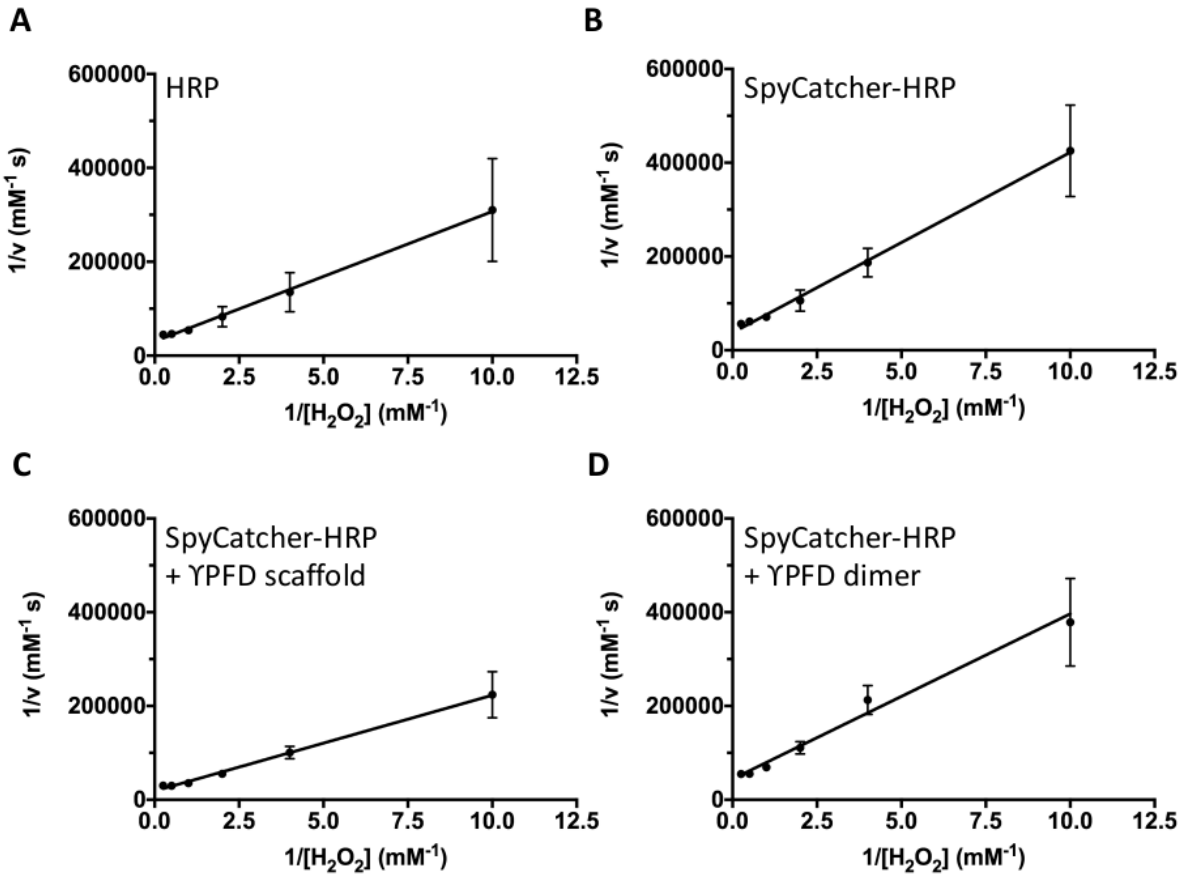

Figure S2.2: (A) Native HRP (B) SpyCatcher-HRP (C) SpyCatcher-HRP scaffolded to γPFD-SpyTag filament at enzyme-to-scaffold ratio of 1:8 (D) SpyCatcher-HRP scaffolded to γPFD-SpyTag dimer at enzyme-to-scaffold ratio of 1:2

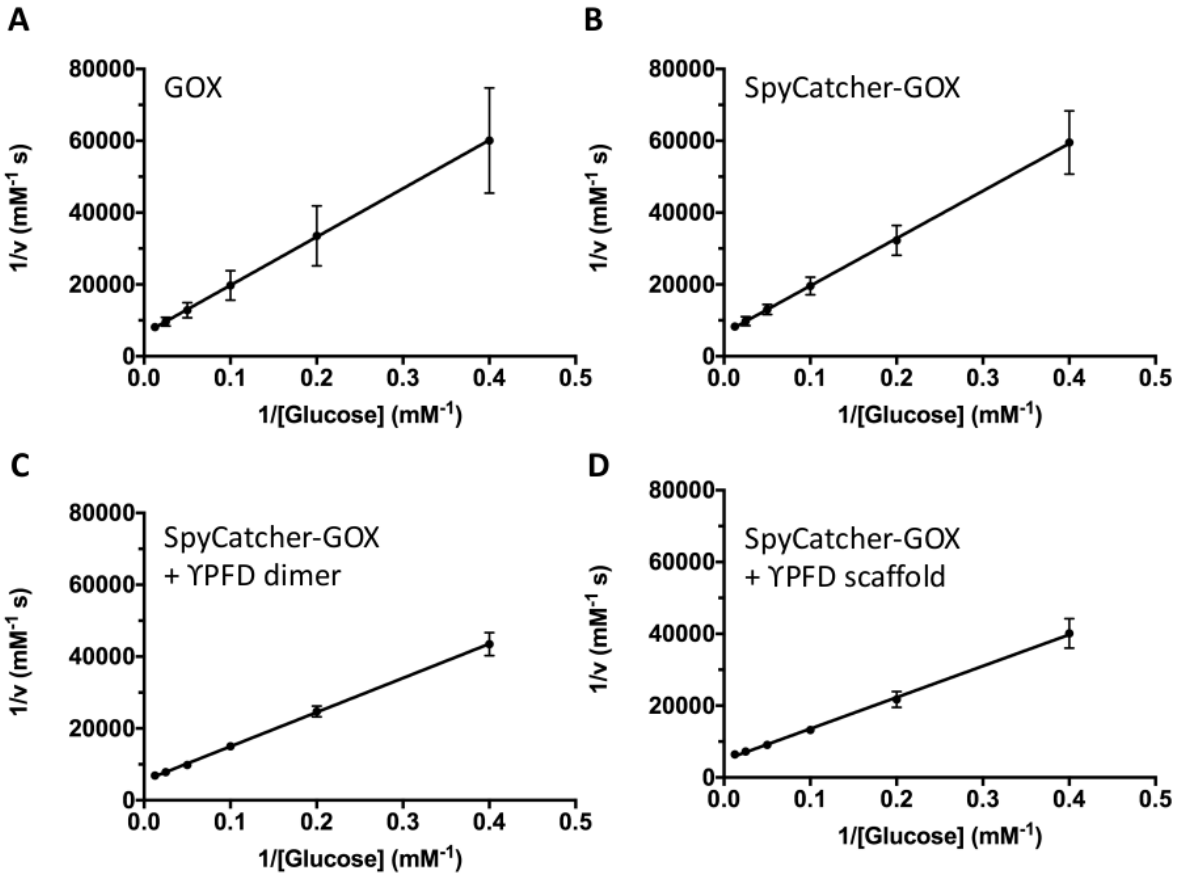

Figure S2.3: (A) Native GOX (B) SpyCatcher-GOX (C) SpyCatcher-GOX scaffolded to γPFD-SpyTag filament at enzyme-to-scaffold ratio of 1:4 (D) SpyCatcher-GOX scaffolded to γPFD-SpyTag dimer at enzyme-to-scaffold ratio of 1:2

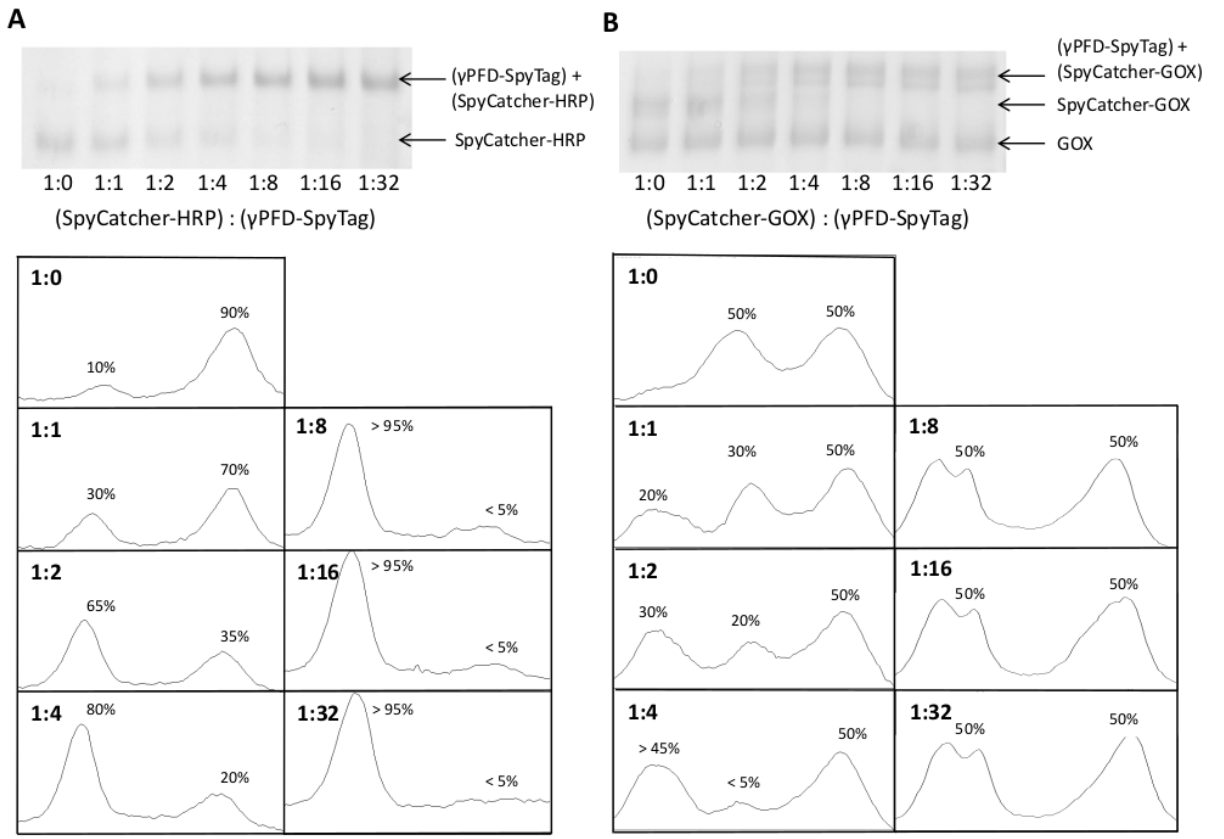

Figure S2.4: Densitometry analysis was used to quantify the degree of conjugation reaction between SpyCatcher-bound enzymes and γPFD-SpyTag scaffold. (A) SDS-PAGE of the SpyCatcher-HRP assembled with γPFD-SpyTag at varying molar ratios from 1:0 to 1:32 (top) and the relative intensity of the bands corresponding to the enzymes bound (SpyCatcher-HRP + γPFD-SpyTag) and unbound (SpyCatcher-HRP) to the scaffold calculated using densitometry (bottom). Almost complete conjugation was observed at a ratio of 1:8 or higher. (B) SDS-PAGE of the SpyCatcher-GOX assembled with γPFD-SpyTag at varying molar ratios from 1:0 to 1:32 (top) and the relative intensity of the bands corresponding to the enzymes bound (SpyCatcher-GOX + γPFD-SpyTag) and unbound (SpyCatcher-GOX) to the scaffold calculated using densitometry (bottom). Almost complete conjugation was observed at a ratio of 1:4 or higher. Note that the band representing GOX without SpyCatcher did not shift, and the relative intensity was 50% for all ratios.

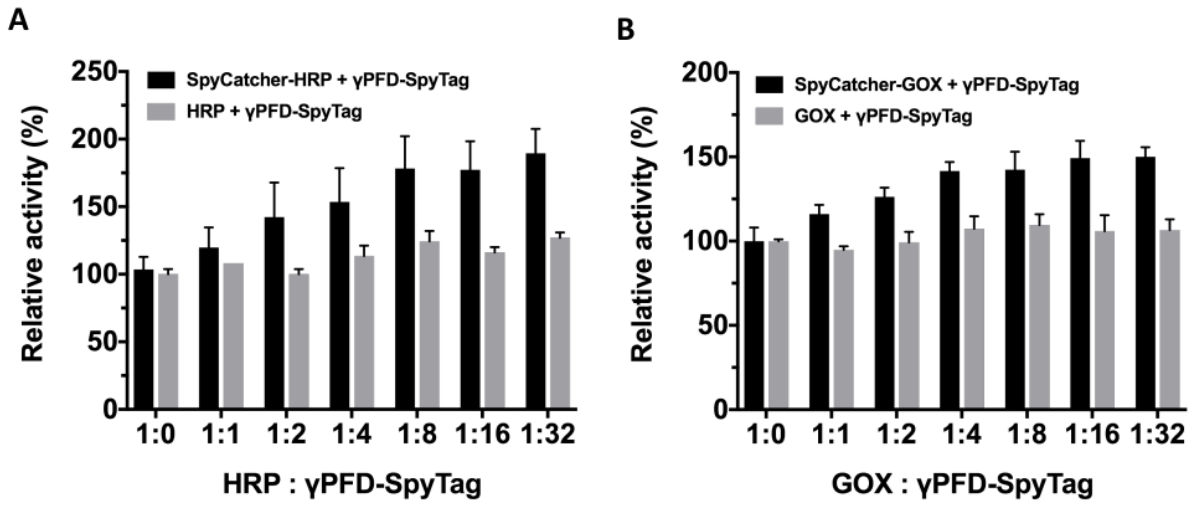

Figure S2.5: HRP and GOX enzymes without SpyCatcher domain were mixed with γPFD-SpyTag at varying molar ratios to investigate whether γPFD-SpyTag can enhance the catalytic activities of enzymes without direct covalent conjugation. (A) Relative activities of SpyCatcher-HRP assembled on γPFD-SpyTag or HRP simply mixed with γPFD-SpyTag were measured at varying enzyme-to-scaffold ratios from 1:0 to 1:32. For each case, 100% relative activity corresponds to the activity measured using SpyCatcher-HRP or HRP enzyme without adding scaffold (1:0 ratio). (B) Relative activities of SpyCatcher-GOX assembled on γPFD-SpyTag or GOX simply mixed with γPFD-SpyTag were measured at varying enzyme-to-scaffold ratios from 1:0 to 1:32. For each case, 100% relative activity corresponds to the activity measured using SpyCatcher-GOX or GOX enzyme without adding scaffold (1:0 ratio). All of the above experiments were performed at least three times, and the error bars represent the SD.

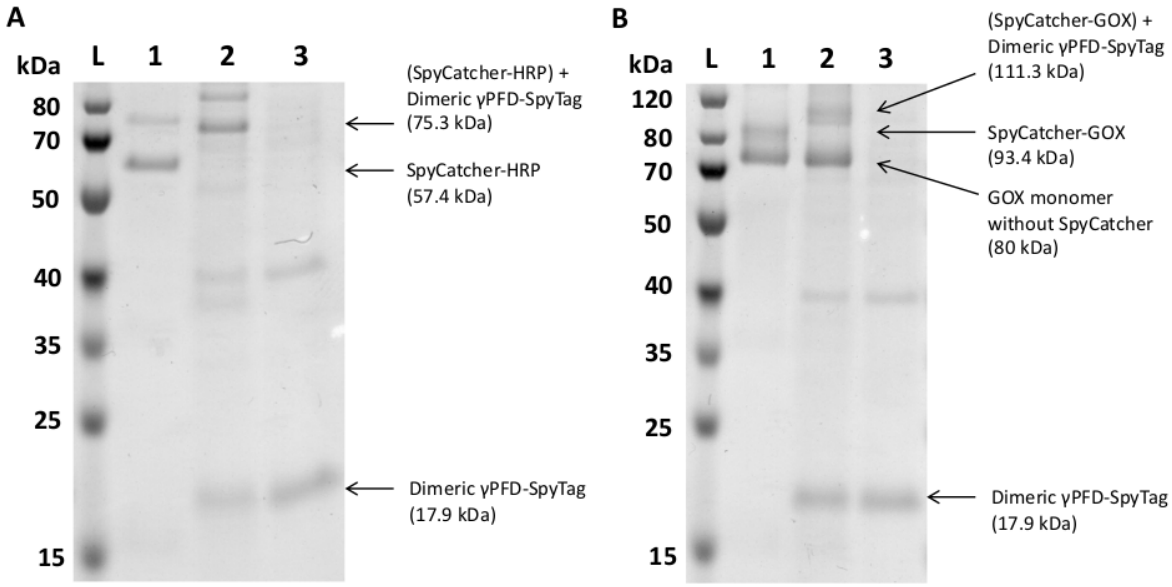

Figure S2.6: Conjugation of (A) SpyCatcher-HRP and (B) SpyCatcher-GOX with 2-fold molar excess of dimeric γPFD-SpyTag was verified by the upward shifts of the band in SDS-PAGE. Each subunit of the dimeric γPFD-SpyTag has molecular weight of 17.9 kDa, which is slightly smaller than that of the filament-forming γPFD-SpyTag (18.1 kDa). Note that the dimeric γPFD-SpyTag contained a small impurity that appeared near 40 kDa in the gel.

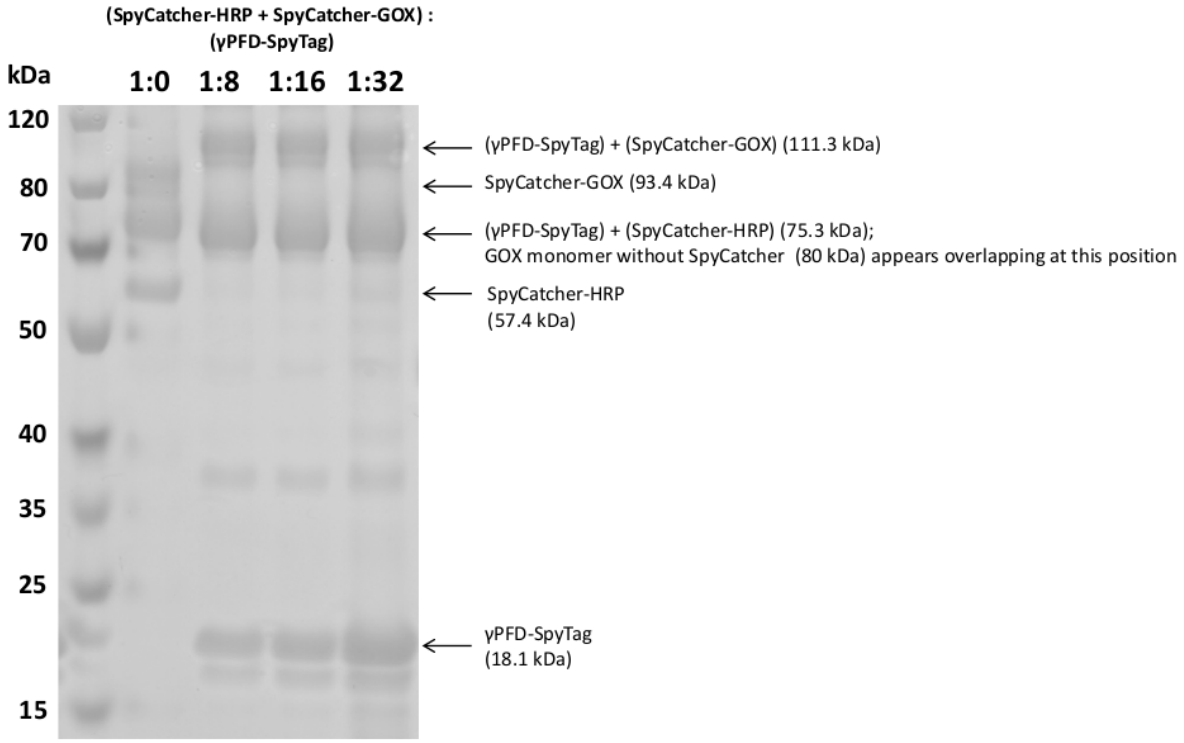

Figure S2.7: Co-immobilization of SpyCatcher-HRP and SpyCatcher-GOX on γPFD-SpyTag at varying total enzyme-to-scaffold ratios of 1:0, 1:8, 1:16 and 1:32; for all ratios, equivalent amounts of both enzymes were used. The bands corresponding to GOX monomer without SpyCatcher (80 kDa) and SpyCatcher-HRP bound to γPFD-SpyTag (75.3 kDa) appeared overlapping and were difficult to differentiate one from another. Regardless, disappearance of SpyCatcher-HRP band as well as SpyCatcher-GOX band indicated that at all three ratios, conjugation reaction went to near completion.

Chapter 3

Patterned assembly of γPFD subunits using novel interaction domains

3.1 Abstract

Exploiting the ability of proteins to self-assemble into architectural templates may provide novel routes for the positioning of functional molecules in nanotechnology. In this chapter we describe the engineering of multicomponent protein templates composed of distinct monomers that assemble in repeating orders into a dynamic functional structure. This was achieved by redesigning the protein-protein interfaces of γPFD with helical sequences to create unique subunits that assemble through orthogonal coiled-coils into filaments up to several hundred nanometers in length. Subsequently, it was demonstrated that functional proteins could be fused to the subunits to achieve ordered alignment along filaments. Importantly, the multicomponent filaments had molecular chaperone activity and could prevent other proteins from thermal-induced aggregation, a potentially useful property for the scaffolding of enzymes. The design described here is presented as proof-of-concept for the creation of modular templates that could potentially be used to position functional molecules, stabilize other proteins such as enzymes, and enable controlled assembly of nanostructures with unique topologies.

3.2 Introduction

The construction of nanoscale devices requires the placement of functional molecules in specific arrangements with nanometer precision. Nature has met this challenge of nanofabrication by exploiting the remarkable ability of proteins to self-assemble into ordered and intricate nanostructures such the icosahedral lattices of viral capsids and cellular scaffolding provided by cytoskeletal proteins. Repurposed natural protein assemblies have been used as templates for nanotechnology; however, these top-down approaches are limited in terms of

engineerability and adaptability [1]. As an alternative, protein assemblies can serve as inspiration to build novel templates for the positioning of molecules that also possess genetically encoded functionality and molecular recognition capabilities.

The construction of protein templates relies upon engineering the interfaces between individual protein subunits to drive self-assembly into specific functional structures. One approach that has had notable success uses the simple but well understood structural elements of coiled coils to create complex assemblies. Coiled-coil domains are intertwined helical sequences that associate together by hydrophobic and electrostatic interactions in seven-residue repeats conventionally labelled abcdefg, with the hydrophobic residues typically located in the a and d positions [2]. These protein domains are attractive interfaces for engineering nanostructures as the rules governing coiled-coil assembly are well understood, which has facilitated the rational and computational design of de novo coiled-coils [3–8]. These engineered coiled-coils have been used to build novel structures and scaffolds, including fibers [9, 10], nanotubes [11], molecular motors [12], and geometrical structures such as triangles [13], tetrahedrons [14], and cages [15]. In addition to creating structures, *de novo* coiled-coil interfaces may also be incorporated into other functional proteins to potentially create scaffolds that impart useful mechanical, enzymatic, or protective properties on templated materials.

As described in Chapter 1, engineered coiled-coil interfaces have recently been used build connector parts that can control the assembly of γPFD into branched assemblies such as the pinwheel shapes. Herein, we expanded the design of the γPFD interface to create unique modular subunits that assemble in repeating orders, thereby producing heteromeric filaments [16, 17]. We exploited the modularity of multiple orthogonal coiled-coils to create a two-component assembly (A-B-A-B- etc.) that was shown to form filaments of several hundred nanometers in length. A ratiometric FRET assay was used to study the assembly and spacing of molecules along the filament. Further, the assembled two-component filament had molecular chaperone activity and could reduce aggregation of a heat-labile protein. The creation of these multicomponent modular assemblages that can spatially control the localization of functional molecules opens new directions in bio- and nano-materials design, enzyme and metabolic engineering, and molecular delivery.

3.3 Methods

Protein design and production

The EE and KK subunits were created by replacing both the X1 and X2 β-sheets in the γPFD subunit with either the E-coil or K-coil helical sequences[16] separated by Gly-Gly-Ser spacer sequence repeats. DNA encoding the engineered subunits was synthesized as gBlocks Gene Fragments (IDT) and inserted into the multiple cloning site of the plasmid pET-19b (Novagen) by the Gibson reaction. Plasmid DNAs encoding engineered subunits or the wild-

type γPFD were transformed into BL21 T7 Express (NEB) and grown at 37°C in lysogeny broth (LB) containing 100 μg mL^{-1} ampicillin to A600=0.6. Protein expression was induced at 24°C for 15 h with addition of 0.1 mM IPTG. Cells were harvested by centrifugation at 6000g for 20 min and lysed by two passes through a French press. Wild-type γPFD was purified as described in Chapter 2. The engineered subunits were purified by binding to Ni-NTA resin (Life Technologies), washed with 50 mM NaH_2PO_4, 20 mM imidazole and 1 M NaCl, pH 8.0, and eluted using a gradient of 50 mM to 1 M of imidazole in 50 mM NaH_2PO_4 and 1 M NaCl, pH 8.0. The purity of eluted protein fractions was determined by visual inspection of an SDS-PAGE gel stained with SimplyBlue (Invitrogen). Fractions containing pure protein were dialyzed overnight against several changes of dialysis buffer (20 mM NaH_2PO_4, 100 mM NaCl, pH 7.5), concentrated using Amicon Ultra centrifugal columns (Millipore), and lyophilized for storage.

Protein modelling

Atomistic models of the engineered heterodimer coiled-coils were created using CCbuilder 2.0 using standard parameters [18]. Subsequently, the strength of interactions between the helices in each modelled coiled-coil was examined using CoilCheck+ using standard parameters26, which measures the strength of interactions between helices involved in coiled-coils. Iterative threading was performed using the I-TASSER server [19] to model the structure of the engineered subunits.

Protein refolding and filament assembly

Lyophilized protein stocks were solubilized in 8 M guanidinium-HCl, 10 mM NaH_2PO_4, pH 8.0 and protein concentration determined using the Bradford assay. Filaments were assembled by mixing together subunits in varying ratios and refolded by either rapid dilution as used previously for γPFD or by step-wise reduction in the concentration of guanidinium-HCl. The samples were dialyzed against buffers that contained 8 to 0 M guanidinium-HCl and 20 mM NaH_2PO_4, 100 mM NaCl, pH 7.4 using 2 h incubations for each step. The guanidinium-HCl concentration was reduced by 1 M for each step until a buffer containing no guanidinium-HCl was obtained, which was incubated for an additional 24 h at 25°C to facilitate filament assembly.

Imaging and quantification of filaments

Filaments were imaged by transmission electron microscopy (TEM) using a Tecnai 12 120KV (FEI) and images captured by a Gatan Ultrascan 1000 digital micrograph. Samples were prepared by diluting the various refolded proteins in PBS at 1.2 μM, deposited onto 400-mesh carbon/formvar coated copper grids (Electron Microscopy Sciences), and stained with 2% uranyl acetate. Filament lengths in the digitized TEM images were quantified using

the ImageJ public-domain software (U.S. National Institutes of Health) and Student's t-tests performed to determine statistical significance.

Circular dichroism

Protein supersecondary structure was examined by far-UV circular dichroism (CD) on a Jasco J-810 spectropolarimeter (Jasco Cooperation). Refolded proteins were dialysed against 20 mM NaH_2PO_4, pH 8.0, and diluted to a final concentration of 10 μM. The CD spectra were obtained by averaging three wavelength scans from 200 to 260 nm in 0.5 nm steps with a signal averaging time of 2 s and a bandwidth of 1 nm at 25°C in a cuvette with a path length of 1 mm. All samples were recovered, and protein concentration verified by Bradford assay.

FRET filament assembly assay

The assembly and spacing of EE and KK subunits in filaments were examined using a FRET assay. The fluorescent fusion proteins EE-mCerulean3 and KK-mVenus were combined with varying ratios of the EE and KK proteins to achieve a final concentration of 1 μM for both the EE-mCerulean3 and KK-mVenus and 0-16 μM for both the EE and KK proteins. Subsequently, the subunits were assembled into filaments by refolding by step-wise reduction in the concentration of guanidinium-HCl by dialysis against 50 mM Tris-HCl pH 7.5, 18 mM NaCl, 8 mM KCl, 400 mM L-arginine, 1 M guanidinium-HCl, 1 mM EDTA, 10% glycerol, 5 mM dithiothreitol, followed by a 24 h incubation at 25°C. Control samples of EE-mCerulean3 or KK-mVenus alone were also refolded. The refolded proteins were transferred to the wells of a black 96-well plate and fluorescence measured in a SpectraMax plate reader (Molecular Devices) using a 400-nm excitation, 420-nm cutoff filter, and emission scan of 450-600 nm. A buffer blank was subtracted from all samples, and the fluorescence from the KK-mVenus control subtracted from samples to compensate for the minimal excitation of mVenus. The FRET efficiency was calculated using the equation:

$$E = \frac{I_{\mathrm{AD}}\epsilon_{\mathrm{A}} - I_{\mathrm{A}}\epsilon_{\mathrm{A}}}{I_{\mathrm{A}}\epsilon_{\mathrm{D}}}$$

where I_{AD} and I_A are the intensities of mVenus acceptor in the presence and absence of the mCerulean3 donor, respectively, and ϵ_D and ϵ_A are the reported extinction coefficients of the mCerulean3 (40,00 M^{-1} cm^{-1}) and mVenus (92,200 M^{-1} cm^{-1}) [20]. Fluorescent spectra were integrated using a—e Spectral Software 1.2 (FluorTools). Subsequently, the distance between mCerulean3 and the mVenus (R) was calculated using the equation:

$$R = R_0 \sqrt[6]{\frac{1-E}{E}}$$

with E being the measured FRET efficiency and R_0 being the reported Forster distance of 5.71 nm of the mCerulean3 and mVenus pair [20]. Ratiometric FRET activity was calculated in each sample by dividing the 475 nm mCerulean3 emission peak by the 528 nm emission peak of mVenus.

Chaperone assay

The ability of the engineered heteromeric filaments to reduce the aggregation of citrate synthase (CS) was examined through a chaperone assay. Briefly, filaments were diluted in 40 mM HEPES-KOH, pH 7.2 to a concentration of 2 μM. The samples were degassed for 20 min and CS from porcine heart (Sigma-Aldrich) added to a final concentration of 1 μM. Thermal aggregation of CS at 45°C was monitored by measuring turbidity at 500 nm with a Lambda UV-Vis spectrometer (PerkinElmer) over 25 min. The absorbance of a buffer only control was subtracted from all samples.

Dynamic light scattering

Dynamic light scattering (DLS) was performed on a Malvern Instruments Zetasizer Nano ZS. Protein samples were freshly prepared prior to the measurements. A minimum of 6 scans were taken for each measurement and a minimum of 6 measurements were taken for each sample.

Atomic force microscopy

Atomic force microscopy (AFM) measurements were performed on a standard AFM instrument (MFP-3D Asylum Research, Oxford Instruments) equipped with an acoustic isolation chamber (AEK 2002). The EE-KK fiber was dispersed on a pre-cleaned silicon substrate for 5 min and washed with DI water before measurement. Measurements were performed at room temperature employing an Al (100) coated silicon cantilever with the bare silicon tip (AC240TS-R3, Asylum Research, Oxford Instruments). Measurements were performed at a low scan rate of 0.2 Hz and with a resolution of 256-by-256 pixel. During the whole scanning process, ambient light was minimized by the AFM isolation chamber, while a low-intensity $\sim$ 5 mW infrared (IR) diode (860 nm) was used to detect probe deflection.

3.4 Results

Redesigning γPFD assembly interfaces

It has been previously demonstrated that the X2 β-sheet of γPFD can be replaced with helical sequences to create binding-partners that associate through coiled-coil interactions[21]. We began by expanding this approach by replacing both the X1 and X2 β-sheet

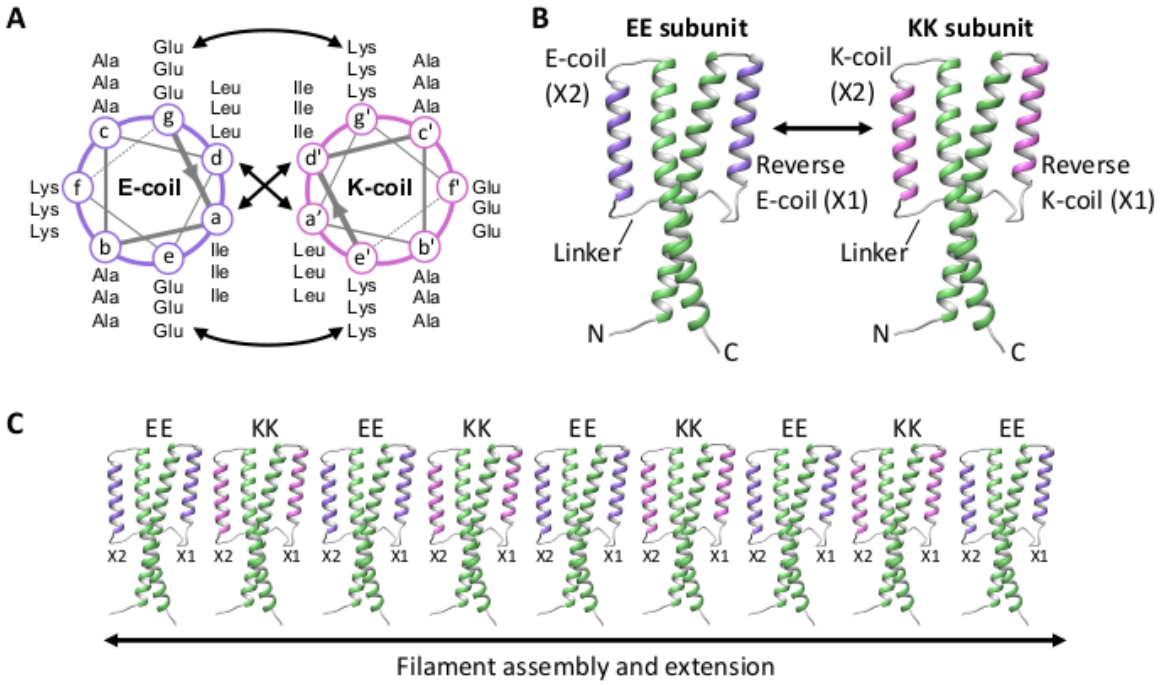

Figure 3.1: Redesign of the γPFD interface to create ordered heteromeric filaments. (A) Helical wheel representation of the E-coil and K-coil heterodimer, in which the coiled-coil is viewed as a cross-section (three letter amino acid code). The inter-helical hydrophobic interactions (a-d', d-a') and electrostatic interactions (g-g', e-e') are denoted with arrows. (B) Replacement of both β-sheet domains in the γPFD subunit with either E-coil or K-coil in place of the X2 β-sheet and either the reversed E-coil or reversed K-coil in place of the X1 β-sheet, creating the subunits "EE" and "KK", respectively. The N- and C-terminus of the subunits are shown. (C) Hypothetical model showing the individual EE and KK subunits oligomerizing into heteromeric filaments through the E-coil/K-coil coiled-coil interactions.

of γPFD with helical sequences to create subunits that should assemble in repeating orders. The helices of the heterodimer E3/K3 coiled-coil were chosen to replace the β-sheets to create specific binding partners. The E3/K3 coiled-coil consists of two oppositely charged helical domains (E-coil and K-coil), which are rich in glutamic acid and lysine residues, respectively [22]. The presence of the oppositely charged glutamic acid and lysine results in strong and specific interhelical electrostatic interactions, which also prevent the E-coil and K-coil from homodimerization (Figure 3.1A).

In our design, the individual subunits are required to interact through antiparallel coiled-coils. This is to insure the coiled-coil backbone of the γPFD in each subunit is orientated in the same direction for chaperone functionality. The E- and K-coil inherently form parallel coiled-coils [22]; however, it has previously been shown that reversing the sequence of either E-coil or K-coil can generate a dimeric antiparallel coiled-coil [23, 24]. We took advantage of this strategy and introduced either a reversed E-coil or a reversed K-coil in place of the X1 β-sheet and either the original E-coil or K-coil in the X2 position, creating the subunits "EE" and "KK", respectively. The two introduced helical sequences were joined through a flexible glycine-serine linker.

To gain insight into the potential structure of the EE and KK subunits, iterative threading was performed using the I-TASSER server [19]. The predicted protein models had the coiled-coils of the wildtype γPFD but the E- or K-coil in place of the β-sheets, with an engineered helix in the X1 position extending downwards and an engineered helix in the X2 position extending upwards joined through the flexible linker (Figure 3.1B). The subunits should oligomerize into heteromeric filaments through the formation of antiparallel coiled-coils between the introduced helices in the subunits (Figure 3.1C). This assembly should also result in coiled-coils of the γPFD protruding outwards for potential chaperone activity.

Two-component filament assembly

The engineered protein subunits were expressed natively in *E. coli* and purified using affinity chromatography. To control the assembly process, the EE and KK subunits were first denatured in 8 M guanidinium-HCl and mixed together in an equimolar concentration. Denaturing the subunits also enables fluorescent variants to be included in subsequent experiments for incorporation into filaments. The proteins were refolded and assembled into filaments over a 24-h period by slowly reducing the concentration of guanidinium-HCl.

Secondary structure comparison of the individual EE and KK subunit by circular dichroism showed that the proteins were structurally similar to γPFD and predominately helical with minima near 208 and 222 nm (Figure 3.2). The large coiled-coil backbone of γPFD in each subunit is likely contributing most of the helical signal; however, it was possible to observe an increase in the ellipticity ratio of $[\theta]222$ over $[\theta]208$ when equimolar ratios of EE and KK subunits were combined and refolded together (Table S3.1). This change in

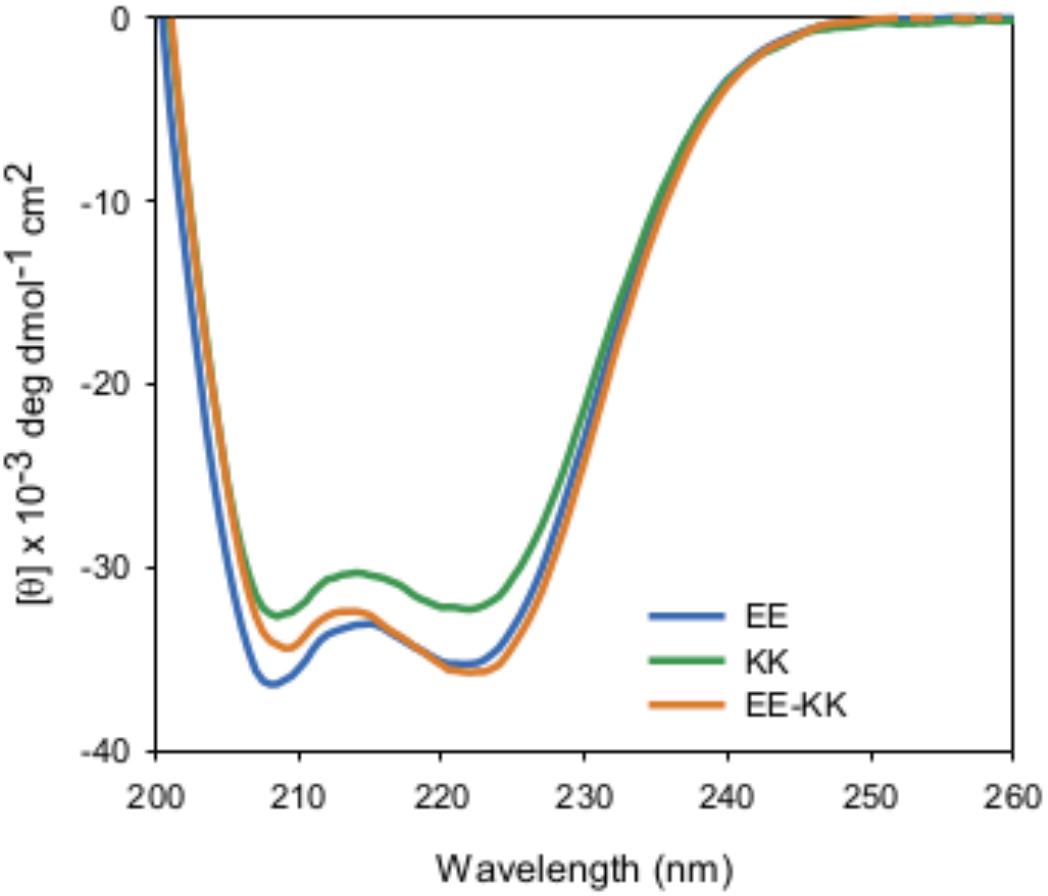

Figure 3.2: Interaction of the E-coil and K-coil helical domains in the EE and KK subunits. Circular dichroism spectra of the EE and KK subunits alone or assembled as EE-KK filaments. Total protein concentrations in each sample was 10 μM.

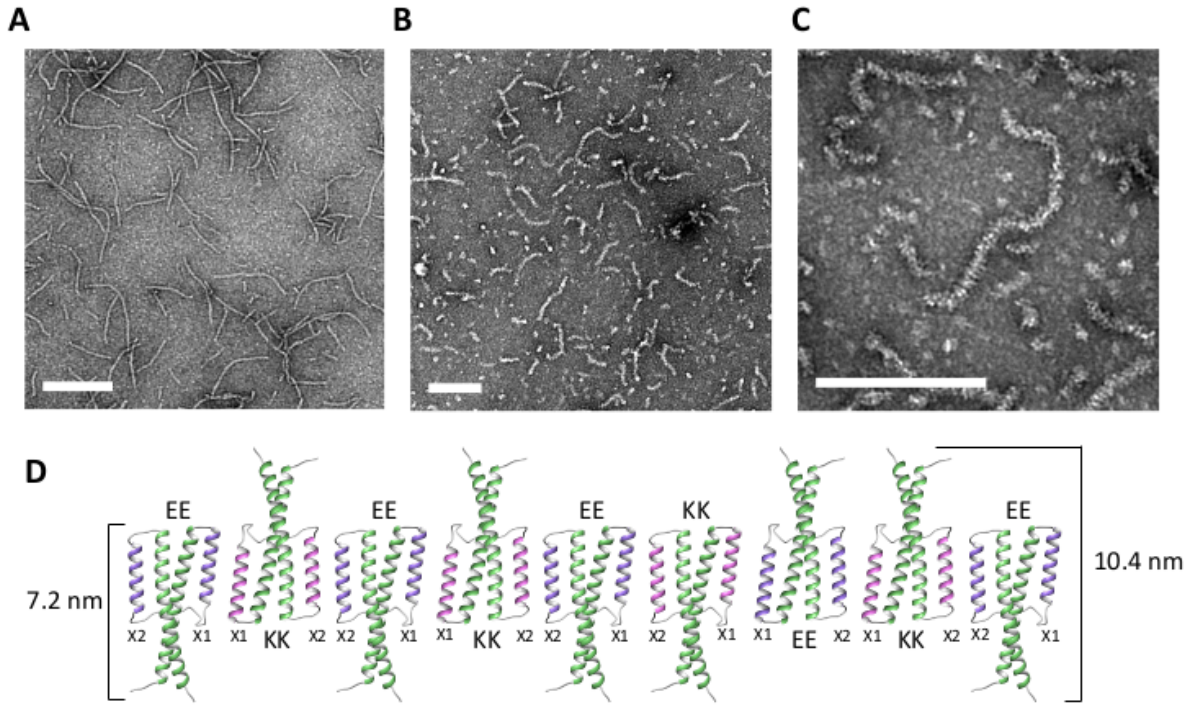

Figure 3.3: Assembly of γPFD or engineered subunits into filaments. Negative-stain TEM images of (A) wild-type γPFD, (B) EE-KK filaments, (C) EE-KK filament at higher resolution. All scale bars = 200 nm. (D) Model of the potential antipodal alignment of individual EE and KK subunits in the EE-KK filament.

ellipticity is consistent with an increase in coiled-coil structure that would occur when the EE and KK subunits associate together.

Subsequently, we imaged the EE and KK subunits individually or as a mixture by transmission electron microscopy (TEM) on carbon support. The wild-type γPFD was also imaged for comparison and was shown to form characteristically long and relatively straight filaments with an average length of 397 nm and width of 8.6 nm (Figure 3.3A). Filament formation was not observed with the EE or KK subunits by themselves. However, when combined and refolded together in an equimolar ratio, the EE-KK mixture formed filaments (Figure 3.3B). Measurement of the length of 500 filaments in the digitized TEM images in three separate experiments revealed an average length of 288 nm ± 28 nm. With a predicted diameter of each subunit of 3.85 nm along the filament, an average length filament would contain 75 individual subunits. To confirm that individual EE and KK subunits do not assemble into filaments alone, dynamic light scattering (DLS) was used to measure the size

distribution of EE and KK monomers and EE-KK filaments (Figure S3.1). The size of the EE and KK monomers was approximately 1 nm, demonstrating that individual subunits do not assemble into large structures. However, the EE-KK combination was observed to form structures approximately 310 nm in size. Considering DLS only measures the diameter of spherical particles, the DLS data for EE-KK should reflect the length of the filament, which matches our length measurement from TEM imaging (288 nm ± 28 nm).

The EE-KK filaments had a morphology that was "pipe cleaner-like" in appearance (Figure 3.3C) unlike the more uniform wild-type γPFD. It has been shown previously that the width of γPFD in TEM images is dependent on the surface orientation of the filament [25]. Wild-type γPFD filaments are deposited with their coiled-coils parallel to the surface. This was evidenced by the width of γPFD filaments in TEM (Figure 3.3A) equivalent to the predicted height of the subunit's coiled-coil of 9 nm. Filaments of EE-KK are also presumably deposited on the TEM grids with their coiled-coils parallel to the surface; however, the filaments had an average width of 11.6 ± 3.3 nm. This was greater than the predicted 7 nm height of individual EE or KK subunits. The EE-KK filament was imaged by atomic force microscopy to further characterize filament dimensions (Figure S3.2). The height of EE-KK filaments imaged using AFM images was 4.2 nm. The width of the half peak in the height profile plot of the EE-KK filament was 30.5 nm. However, considering the soft nature of protein-based materials, along with AFM tip-sample convolution effects (the width of the AFM tip is 7 nm), the corrected width of EE-KK fiber should be around 16 nm, which is close to the TEM result of 11.6 nm ± 3.3 nm for the average fiber width (Figure S3.2). The differences in morphology and width of the EE-KK filament compared with the wild-type γPFD suggest the EE-KK structure deviates from the ordered assembly of γPFD (Figure 1A). The subunits were engineered to assemble through antiparallel coiled-coils between the helices introduced into the X1 and X2 β-sheets. However, additional molecular modelling suggests that subunits could potentially assemble through antiparallel coiled-coils formed between the X1 of the EE and X1 of the KK, or X2 of the EE and X2 of the KK. This reversed assembly would result in the subunit pair rotated 180° relative to each other (Figure 3.3D).

The interactions between the various reversed and original E- and K-coil domains were modelled using CCBuilder 2.0 [18] to produce atomistic models of the heterodimer coiled-coil interfaces. Subsequently, the strength of interactions between the helices in each modelled coiled-coil was examined using CoilCheck+, which measures the strength of interactions between helices involved in coiled-coils [26]. The interaction strength between a reversed E- or K-coil and the non-reversed partner had a predicted stabilizing energy of -24.17 kJ/mol. This interaction strength was similar for interactions between anti-parallel coiled-coils formed between either the X1 of the EE and X1 of the KK, or the X2 of the EE and X2 of the KK, with a stabilizing energy of -23.74 kJ/mol. The similar stabilization energy for both assemblies suggests that either assembly is equally probable. Ultimately, the actual orientation of the subunits is most likely random, which may explain the pipe-cleaner appearance of the

filaments with individual subunits projecting outwards in opposing directions (Figure 3.3C). Furthermore, this antipodal assembly (Figure 3.3D) would result in filaments that have a predicted width of 10.4 nm when deposited on the TEM carbon support, which is closer to the observed width of the EE-KK filaments.

Characterizing the controlled two-component assembly using FRET assay

A ratiometric FRET assay was used to better understand the assembly of EE-KK filaments, and demonstrate the ability to position functional molecules at regular spacing along filaments. In this approach, two FRET fusion proteins were created with the cyan fluorescent protein mCerulean3 fused to the EE subunit and the yellow fluorescent protein mVenus fused to the KK subunit. These proteins were expressed natively in *E. coli* and purified using affinity chromatography. When mixed together and refolded, the EE-mCerulean3 and KK-mVenus should assemble and thereby bring the mCerulean3 and mVenus domains into sufficient proximity for FRET to occur (Figure 3.4A). If in sufficient proximity, excitation of the mCerulean3 will result in energy transferred to the mVenus for emission at its emission peak. The efficiency of this energy transfer is directly related to the distance between the donor and acceptor. As expected, the assembly of the fluorescent fusion proteins EE-mCerulean and KK-mVenus resulted in FRET with a decrease in emission of the mCerulean at 475 nm and an increase in mVenus emission at 528 nm (Figure S3.3). Analysis of the integrated intensities of the fluorescent protein spectrums enabled the FRET efficiency to be determined, which was 9.4%. With a Förster radius of 5.71 nm for the mCerulean3-mVenus pair [20], this FRET efficiency corresponds to a distance measurement of 8.3 nm. It was predicted that binding of the EE-mCerulean to KK-mVenus through the helices introduced into the X1 and X2 β-sheets will result in the fluorescent protein pair positioned at minimal distance of approximately 3.5 nm from the chromophore centers. The coiled-coils of γPFD have been shown to be flexible [27], which may result in the fluorescent pair further apart but still produce efficient FRET (Figure 3.4A). However, subunits that are rotated 180° relative to each other are predicted to be approximately 10.6 nm apart, thereby producing negligible FRET. The distance measurement of 8.3 nm suggests that the EE and KK are not continually aligned directly adjacent to each other, most likely due to antipodal assembly (Figure 3.4D). It is important to note, however, that the FRET distance measurement is not an average distance as FRET efficiency is related to the sixth power distance between the donor and acceptor. As the alignment of the fluorescently-fused EE and KK is most likely a distribution, fluorescent proteins in close proximity contribute significantly more to the FRET signal than fluorescent proteins spaced at greater distances.

The assembly of the EE and KK in repeating orders can also be probed using the FRET assay. Addition of EE and KK (not fused to a fluorescent protein) should result in the FRET fusion proteins spaced further apart, thereby leading to a decrease in FRET signal (Figure 3.4A). To verify this, molar ratios ranging from 0.1 to 16 μM of both the EE and KK proteins

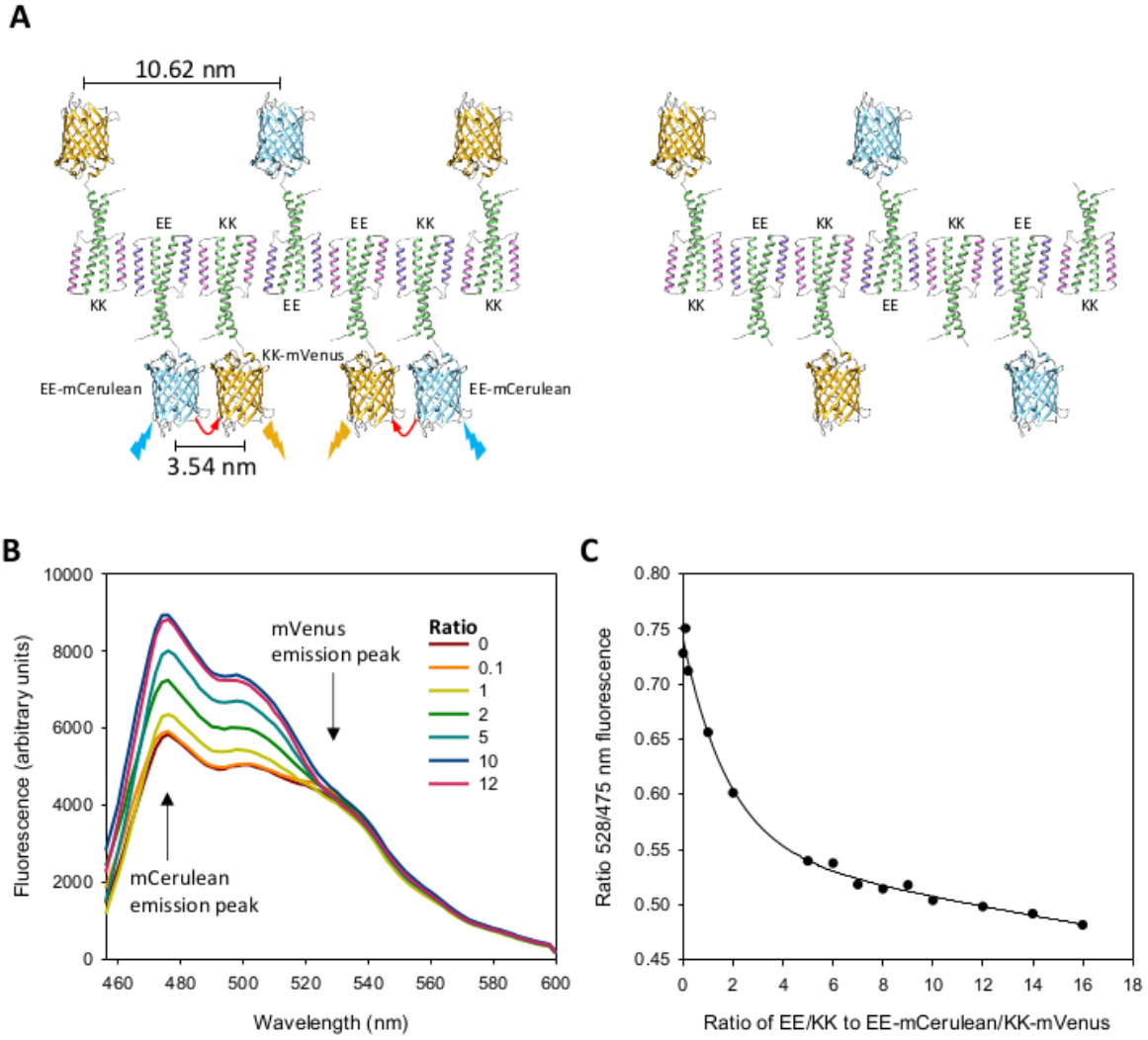

Figure 3.4: Heteromeric filament assembly and subunit positioning monitored by a FRET assay. (A) To monitor the position of individual subunits within the filament, a FRET pair was created by fusing mCerulean3, a cyan fluorescent protein to the EE subunit and fusing mVenus, a yellow fluorescent protein to the KK subunit. When refolded and assembled, the EE-mCerulean3 and KK-mVenus in close proximity will enable FRET to occur upon excitation of the mCerulean3. Altering the distribution of subunits by addition of the EE and KK subunits will space out the fluorescent subunits resulting in a decrease in FRET signal. (B) Fluorescence emission spectra of the EE-mCerulean3/KK-mVenus following titration of varying ratios of EE/KK and refolding. (C) FRET signal at varying ratios of the EE/KK subunits to the EE-mCerulean/KK-mVenus.

were mixed with 1 μM of both the EE-mCerulean3 and the KK-mVenus and refolded into filaments. As expected, addition of the EE and KK subunits relative to the FRET pair EE-mCerulean3/KK-mVenus was correlated with a significant reduction in FRET signal (Figure 3.4B). Ratiometric FRET activity was calculated in each sample by dividing the 475 nm mCerulean3 emission peak by the 528 nm emission peak of mVenus and plotted (Figure 3.4B). At a 1:1 ratio of EE/KK to EE-mCerulean3/KK-mVenus it would be expected that on average there would be one EE or KK subunit spaced between the FRET pair, which would result in negligible FRET (Figure 3.4A). However, as the assembly process results in a stochastic distribution of subunits along the polymer chain, some EE-mCerulean3 would be positioned adjacent to the KK-mVenus thereby enabling FRET to occur. Almost half of the FRET signal was lost in the presence of a two-fold excess of the EE/KK, and almost no FRET occurred at higher ratios as the fluorescent proteins are spaced too far apart. Our approach demonstrates that tuning the ratio of subunits enables control over the spatial distribution of functional molecules along templates in noncovalent synthesis. Developing templates with additional unique subunits will further expand this approach.

Chaperone activity of the multicomponent filaments

The wild-type γPFD has molecular chaperone activity that prevents thermal-induced aggregation of a variety of substrate proteins. We examined if our heteromeric filaments could also stabilize and prevent thermal-induced aggregation of citrate synthase (CS), a heat-labile protein that aggregates at 43°C. CS alone was shown to aggregate over time when heated; however, the inclusion of a 1:1 molar ratio of wild-type γPFD inhibited CS aggregation (Figure 3.5). Neither the EE or KK subunits alone exhibited chaperone activity or was able to prevent CS aggregation. Previous studies into the chaperone activity of the γPFD demonstrated that the protein must be in a filamentous state to exhibit chaperone activity [27]. Indeed, when the EE and KK are assembled into filaments, we observed chaperone activity comparable to the wild-type γPFD (Figure 3.5A).

The chaperone function of archaeal prefoldins has been shown to be closely linked to their quaternary structure [27]. Molecular dynamic (MD) simulations of the γPFD filament have previously revealed that the filament's coiled-coils align to form a hydrophobic cavity that captures and prevents denatured proteins from aggregating. This observation was supported by experimental data that showed a specific number of γPFD coiled-coils in close proximity are required to stabilize denatured proteins of various size. In the case of CS, six to eight γPFD coiled-coils are required to interact with the CS and prevent its aggregation [27]. A similar coiled-coil/substrate size dependence has been observed for other archaeal PFDs [28].

In the case of γPFD, the repeated assembly of dimeric subunits results in two lanes of coiled-coils aligned along the length of the filament that forms the hydrophobic cavity. On the other hand, the EE-KK filaments have single alignment of coiled coils and therefore lack a hydrophobic cavity. Intriguingly, the antipodal assembly of the EE-KK filament (Figure

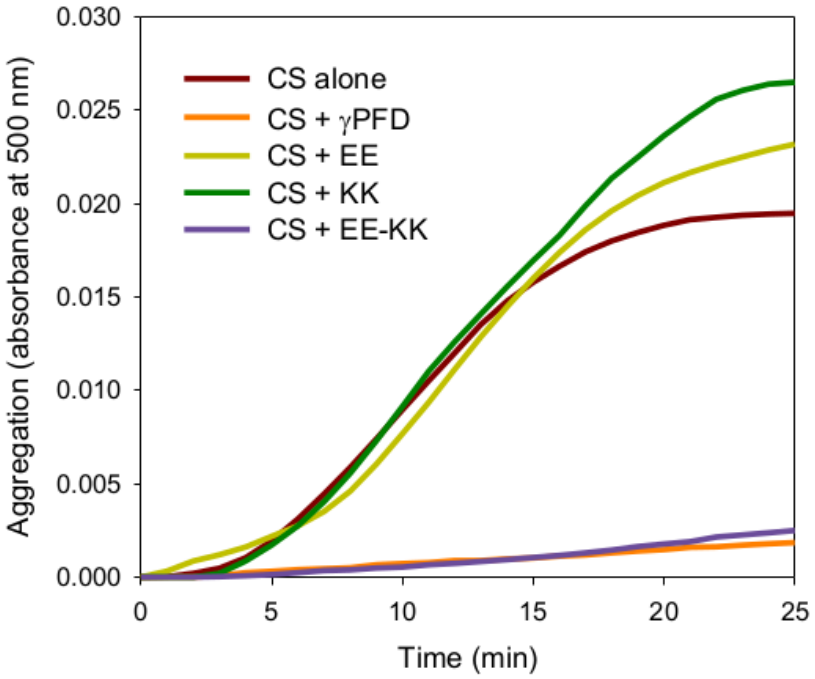

Figure 3.5: Heteromeric filaments decrease heat-induced aggregation of citrate synthase (CS). Chaperone activity was measured by the aggregation of citrate synthase (CS) at 45°C in the absence or in the presence of wild-type γPFD, the EE subunit, the KK subunit, and the EE-KK heteromeric filament. Aggregation of CS resulting from thermal denaturation was quantified by the changes in absorbance at 500 nm over time.

3.3D) may result in coiled-coils that project outwards at varying angles that are still able to capture denatured proteins, resulting in chaperone activity comparable to that of wild-type γPFD filaments. Ultimately, engineered PFD filaments such as the two-component filaments described here may be useful for probing and better understanding the structure-function relationship of molecular chaperones.

3.5 Conclusion

In conclusion, we present an approach for engineering the interface of protein subunits to create multicomponent filaments that enable control over the spatial distribution of functional molecules. Beginning with a two-component system, this approach can be further expanded. We believe there is sufficient diversity and uniqueness in designed coiled-coils

to expand the approach to five or six unique helical interfaces and subunits. Libraries of computationally-designed heterodimeric coiled-coils have been described that may be compatible with our approach, including longer six heptad coiled-coils that enable greater diversity in unique interactions [4, 8]. In addition, the availability of other coiled-coil pairs should enable selection of pairs that avoid the antipodal assembly observed for the EE-KK filament.

As the γPFD coiled-coil is physically separate from the engineered coiled-coil interfaces, the N- or C-terminal of the subunits are easily engineered to attach functional molecules, as was shown by the fusion of fluorescent proteins. One potential application is the attachment and alignment of multiple enzymes to facilitate substrate channelling, a process whereby the reaction product of one enzyme is transferred directly from the enzyme's active site into the active site of the next enzyme of a multistep reaction [1, 29]. Furthermore, the ATP-independent molecular chaperone activity of the multicomponent filaments may be beneficial for the protection and stabilization of attached enzymes. The coiled-coil regions of the subunits in the engineered filaments can be engineered to bind molecules to be aligned in specific ordered arrays, as has been shown with nanoparticles to create inorganic devices [21, 30, 31]. In this application, the coiled-coil domains could also serve to stabilize metal nanoparticles and prevent their salt-induced aggregation [32].

In addition to the assembly of linear templates, the engineered subunits are building blocks that could potentially be used to construct higher-order structures and functional assemblies. Previously, we have demonstrated the ability link multiple γPFD filaments using engineered connector proteins into geometrically-defined structures [21]. The unique interfaces in the multicomponent filaments could be used to assemble with the interfaces of angled connector proteins to gain greater control over the assembly and positioning of functional molecules for biological and material science applications.

3.6 References

1. Glover, D. J. & Clark, D. S. Protein calligraphy: a new concept begins to take shape. *ACS central science* **2,** 438–444 (2016).
2. Grigoryan, G. & Keating, A. E. Structural specificity in coiled-coil interactions. *Current opinion in structural biology* **18,** 477–483 (2008).
3. Bromley, E. H., Sessions, R. B., Thomson, A. R. & Woolfson, D. N. Designed α-helical tectons for constructing multicomponent synthetic biological systems. *Journal of the American Chemical Society* **131,** 928–930 (2008).
4. Reinke, A. W., Grant, R. A. & Keating, A. E. A synthetic coiled-coil interactome provides heterospecific modules for molecular engineering. *Journal of the American Chemical Society* **132,** 6025–6031 (2010).
5. Gradišar, H. & Jerala, R. De novo design of orthogonal peptide pairs forming parallel coiled-coil heterodimers. *Journal of Peptide Science* **17,** 100–106 (2011).
6. Fletcher, J. M. *et al.* A basis set of de novo coiled-coil peptide oligomers for rational protein design and synthetic biology. *ACS synthetic biology* **1,** 240–250 (2012).
7. Thompson, K. E., Bashor, C. J., Lim, W. A. & Keating, A. E. SYNZIP protein interaction toolbox: in vitro and in vivo specifications of heterospecific coiled-coil interaction domains. *ACS synthetic biology* **1,** 118–129 (2012).
8. Negron, C. & Keating, A. E. A set of computationally designed orthogonal antiparallel homodimers that expands the synthetic coiled-coil toolkit. *Journal of the American Chemical Society* **136,** 16544–16556 (2014).
9. Papapostolou, D. *et al.* Engineering nanoscale order into a designed protein fiber. *Proceedings of the National Academy of Sciences* **104,** 10853–10858 (2007).
10. Boyle, A. L. *et al.* Squaring the circle in peptide assembly: from fibers to discrete nanostructures by de novo design. *Journal of the american chemical society* **134,** 15457–15467 (2012).
11. Burgess, N. C. *et al.* Modular design of self-assembling peptide-based nanotubes. *Journal of the American Chemical Society* **137,** 10554–10562 (2015).
12. Small, L. S. *et al.* Construction of a chassis for a tripartite protein-based molecular motor. *ACS synthetic biology* **6,** 1096–1102 (2017).
13. Park, W. M., Bedewy, M., Berggren, K. K. & Keating, A. E. Modular assembly of a protein nanotriangle using orthogonally interacting coiled coils. *Scientific reports* **7,** 10577 (2017).
14. Gradišar, H. *et al.* Design of a single-chain polypeptide tetrahedron assembled from coiled-coil segments. *Nature chemical biology* **9,** 362 (2013).

15. Fletcher, J. M. *et al.* Self-assembling cages from coiled-coil peptide modules. *Science* **340,** 595–599 (2013).

16. Glover, D. J. *et al.* Assembly of multicomponent protein filaments using engineered subunit interfaces. *ACS synthetic biology* **7,** 2447–2456 (2018).

17. Lim, S., Clark, D. S. & Glover, D. J. in *Protein Nanotechnology* 101–115 (Springer, 2020).

18. Wood, C. W. & Woolfson, D. N. C CB uilder 2.0: Powerful and accessible coiled-coil modeling. *Protein Science* **27,** 103–111 (2018).

19. Roy, A., Kucukural, A. & Zhang, Y. I-TASSER: a unified platform for automated protein structure and function prediction. *Nature protocols* **5,** 725 (2010).

20. Markwardt, M. L. *et al.* An improved cerulean fluorescent protein with enhanced brightness and reduced reversible photoswitching. *PloS one* **6,** e17896 (2011).

21. Glover, D. J., Giger, L., Kim, S. S., Naik, R. R. & Clark, D. S. Geometrical assembly of ultrastable protein templates for nanomaterials. *Nature communications* **7,** 11771 (2016).

22. Lindhout, D. A., Litowski, J. R., Mercier, P., Hodges, R. S. & Sykes, B. D. NMR solution structure of a highly stable de novo heterodimeric coiled-coil. *Biopolymers: Original Research on Biomolecules* **75,** 367–375 (2004).

23. Pähler, G., Panse, C., Diederichsen, U. & Janshoff, A. Coiled-coil formation on lipid bilayers—implications for docking and fusion efficiency. *Biophysical journal* **103,** 2295–2303 (2012).

24. Zheng, T. *et al.* A non-zipper-like tetrameric coiled coil promotes membrane fusion. *Rsc Advances* **6,** 7990–7998 (2016).

25. Whitehead, T. A., Je, E. & Clark, D. S. Rational shape engineering of the filamentous protein γ prefoldin through incremental gene truncation. *Biopolymers: Original Research on Biomolecules* **91,** 496–503 (2009).

26. Sunitha, M. S. *et al.* Structural attributes for the recognition of weak and anomalous regions in coiled-coils of myosins and other motor proteins. *BMC research notes* **5,** 530 (2012).

27. Glover, D. J. & Clark, D. S. Oligomeric assembly is required for chaperone activity of the filamentous γ-prefoldin. *The FEBS journal* **282,** 2985–2997 (2015).

28. Kida, H. *et al.* Structural and molecular characterization of the prefoldin β subunit from Thermococcus strain KS-1. *Journal of molecular biology* **383,** 465–474 (2008).

29. Lee, H., DeLoache, W. C. & Dueber, J. E. Spatial organization of enzymes for metabolic engineering. *Metabolic engineering* **14,** 242–251 (2012).

30. Glover, D. J., Giger, L., Kim, J. R. & Clark, D. S. Engineering protein filaments with enhanced thermostability for nanomaterials. *Biotechnology journal* **8,** 228–236 (2013).

31. Slocik, J. M., Kim, S. N., Whitehead, T. A., Clark, D. S. & Naik, R. R. Biotemplated metal nanowires using hyperthermophilic protein filaments. *Small* **5,** 2038–2042 (2009).

32. Sakono, M. *et al.* Size-selective recognition of gold nanoparticles by a molecular chaperone. *Chemical Physics Letters* **501,** 108–112 (2010).

Appendix

3.A Supporting Figures for Chapter 3

Proteins	$[\theta]208^{a}$	$[\theta]222^{a}$	$[\theta]208/[\theta]222^{b}$
EE	-36.32	-35.21	0.97
KK	-32.47	-32.24	0.99
EE-KK	-33.97	-35.68	1.05

Table S3.1 Circular dichroism ellipticity ratios of EE, KK, and EE-KK filaments.

a Ellipticity [10-3 deg $dmol^{-1}$ cm^2] of proteins at 208 and 222 nm.
b Ellipticity ratio of 222/208 nm.

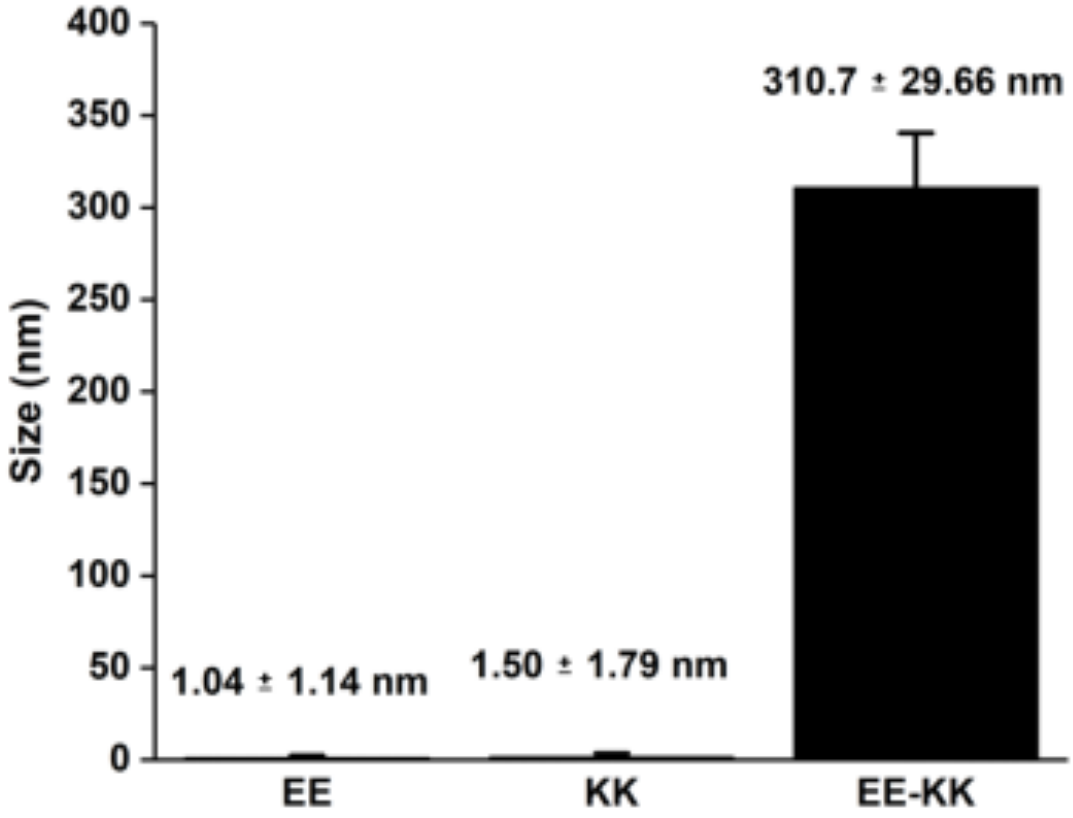

Figure S3.1: Dynamic light scattering (DLS) of EE and KK subunits, and the EE-KK filament.

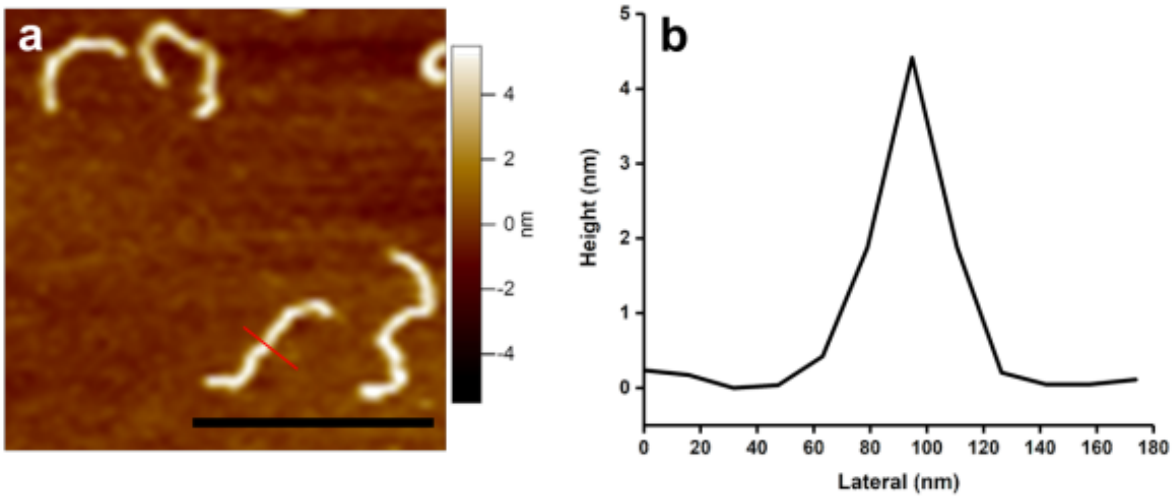

Figure S3.2: (A) Atomic force microscopy height images of EE-KK filaments. Scale bars = 500 nm. (B) Height profile of EE-KK filaments.

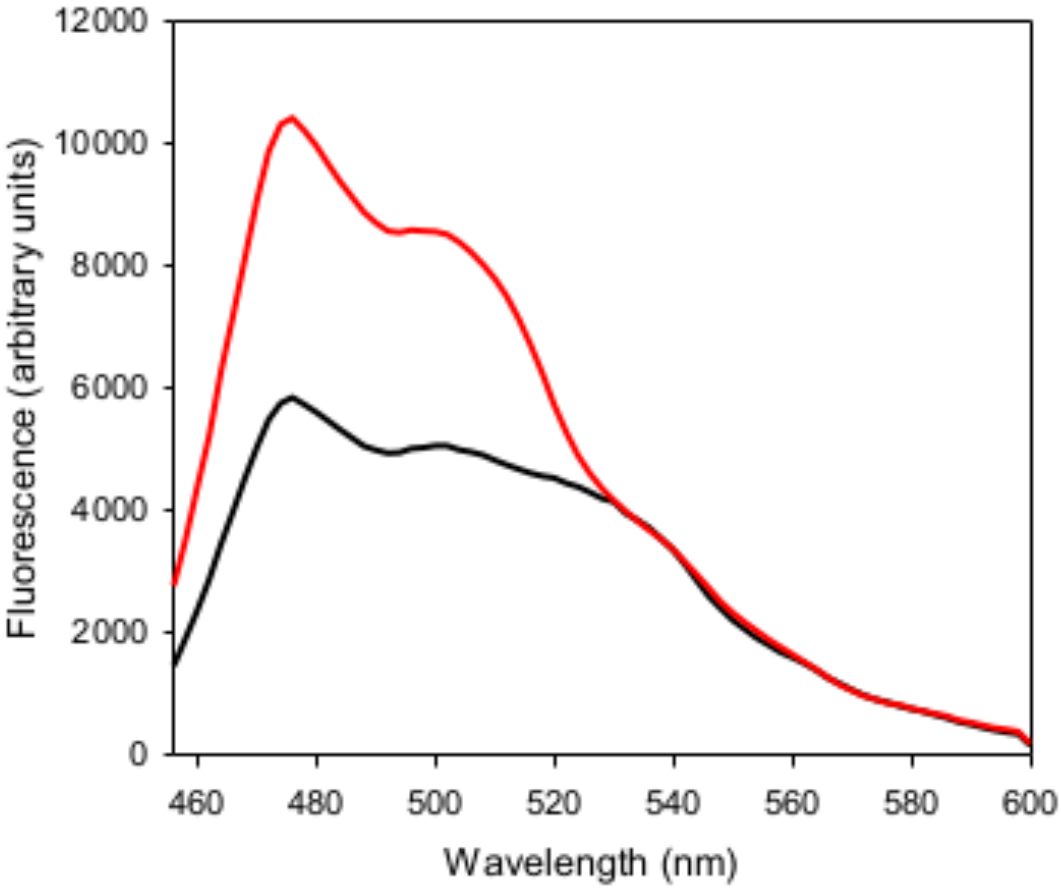

Figure S3.3: Fluorescent emission spectra of EE-mCerulean3 or an assembly of EE-mCerulean3-KK-mVenus after excitation at 400-nm.

Chapter 4

Synthesis of γPFD-based functional hydrogel with tunable properties

4.1 Abstract

In this chapter, we demonstrate the synthesis of protein-polymer hybrid hydrogel that can be used as a platform for immobilizing functional proteins. Orthogonal chemistry was employed for cross-linking the hybrid network and conjugating proteins to the gel backbone, allowing for the convenient, one-pot formation of a functionalized hydrogel. The resulting hydrogel had tunable mechanical properties, was stable in solution, and biocompatible.

4.2 Introduction

Hydrogels are three-dimensional networks of cross-linked macromolecules that can swell under aqueous conditions. Their high water content and resemblance to biological tissue render hydrogels attractive for applications in biotechnology, such as tissue culture scaffolds, wound adhesives, biosensing materials and drug delivery matrices [1–3]. Hydrogels created from synthetic polymers are particularly advantageous considering their low immunogenicity, ease of processing at large scale, and diverse range of crosslinking chemistries [4–6]. Despite such advantages, applications of synthetic hydrogels as biomaterials are limited by their absence of bioactivity [7]. To overcome this limitation, functional protein domains have been incorporated into polymeric hydrogel backbones to create protein-polymer hybrid networks, endowing the gels with complex abilities including stimuli-responsiveness, catalytic activity, or ability to regulate cell behaviors [8–11]. While a number of proteins have been utilized to fabricate functional synthetic hydrogels with hybrid structures, specific chemistries used to cross-link proteins with polymers are typically highly case-specific, reflecting a need for a generally applicable strategy to form hydrogels containing a variety of bioactive proteins [12–14].

In this work, we created a novel protein-polymer hybrid hydrogel as a customizable platform for the stable incorporation of functional proteins [15]. Within the hydrogel network, the protein component functions as a scaffold that captures functional proteins tagged with a specific recognition domain. As this attachment is orthogonal to the crosslink formation of the hydrogel backbone, the functionalized hydrogels can be conveniently and rapidly assembled via one-pot synthesis. Although the conjugation of functional proteins within hydrogels consisting purely of proteins has been reported previously [16, 17], we describe here a generalizable platform for incorporating functional proteins into protein-polymer hybrid hydrogels.

4.3 Methods

Protein expression and purification

The genes encoding SpyTag-γPFD-Cys, mCerulean3 and mVenus with and without SpyCatcher were synthesized as gBlocks gene fragments (Integrated DNA Technologies) and were inserted into the multiple cloning site of the pET-19b plasmid (Novagen) using the Gibson assembly (New England Biolabs). The assembled plasmids were transformed into T7 Express competent cells, which were grown at 37°C in Terrific Broth (IBI Scientific) at 100 μg mL^{-1}ampicillin up to OD 600 = 0.6. Protein expression was induced by adding IPTG to final concentration of 0.1 mM and cells were grown for an additional 15 hours at 25°C. The cells were harvested by centrifugation at 6000 g for 10 minutes, lysed by French press, and centrifuged at 22,000 x g for 50 minutes.

Since γPFD proteins are thermostable, the soluble protein lysate containing SpyTag-γPFD-Cys was placed in an 80°C oven for 30 minutes, and centrifuged at 22,000 x g for 50 minutes again to eliminate aggregated impurities. The resulting supernatant was then purified by anion exchange (Hitrap Q column, GE healthcare) using AKTA FPLC. The proteins were loaded on the column with the equilibrium buffer (100 mM NaCl, 50 mM NaH_2PO_4, 5 mM DTT, pH 7.4) and eluted using a gradient of 100 mM to 1 M of NaCl in 50 mM NaH_2PO_4, 5 mM DTT at pH 7.4. Each elution fraction was inspected using SDS-PAGE and SimplyBlue staining (Invitrogen), and the fractions containing the pure target protein were dialyzed overnight against dialysis buffer (100 mM NaCl, 50 mM NaH_2PO_4, pH 7.4). Finally, the purified proteins were concentrated using Amicon Ultra 15-mL centrifugal columns (10 kDa MWCO, Millipore) and lyophilized for storage at -20°C.

The fluorescent proteins (both with and without SpyCatcher) containing the N-terminal 6xHis tag were purified by binding to Ni-NTA resin (Life Technologies), washed with the equilibration buffer (20 mM imidazole, 50 mM NaH_2PO_4, 1 M NaCl, pH 8.0), and eluted using a gradient of 20 mM to 1 M imidazole in 50 mM NaH_2PO_4, 1 M NaCl at pH 8.0. Fractions containing the pure proteins were dialyzed, concentrated and lyophilized under conditions the same as above.

Hydrogel formation and swelling

Lyophilized SpyTag-γPFD-Cys was resuspended in phosphate buffer (100 mM NaCl, 50 mM NaH_2PO_4, pH 7.4; "phosphate buffer" will refer to this buffer composition in subsequent sections), and the concentration was measured using the Bradford reagent (Bio-Rad). Proteins were then concentrated to twice the desired final concentration using Amicon Ultra 0.5-mL centrifugal columns (10 kDa MWCO, Millipore). PEG-4MAL of 20,000 Da Mw (JenKem Technology) was dissolved in phosphate buffer to twice the desired final concentration. Each component (50 μL) was then mixed by pipetting several times to form the hydrogel with total volume of 100 μL, which was allowed to cure at room temperature for 6 hours. The molar stoichiometry between protein and polymer was always fixed at 4:1.

To measure swelling, formed and cured hydrogels were first weighed (W_i) and then incubated overnight in 900 μL phosphate buffer at room temperature. After removing the buffer, swelled hydrogels were weighed again (W_f). The swelling ratio was calculated as below [18].

$$\text{Swelling ratio } (\%) = \frac{W_f - W_i}{W_i} \times 100$$

Hydrogel erosion

Hydrogels of 100-μL volume were formed and cured as described above. Phosphate buffer (900 μL) was added and incubated at room temperature or at 37°C. At each time point of measurement, a small aliquot of buffer was removed and its protein concentration was measured using the Bradford method to calculate the amount of protein released.

Rheology tests

Oscillatory shear rheology tests were performed with a Physica MCR 301 parallel plate rheometer (Anton Paar), using an 8-mm diameter top plate. Hydrogels of total volume 40 μL were formed *in situ* between the parallel plates at a gap width of 0.8 mm and were allowed to cure in the humidified chamber. Time sweep experiments were conducted at the fixed frequency and applied strain of 1 Hz and 1%, respectively. Amplitude sweep tests were performed at 1 Hz frequency, while frequency sweep runs were performed at 1% applied strain; for all hydrogel samples tested in this study, 1% applied strain was within the linear viscoelastic range.

Fluorescent gel formation and leaching measurements

SpyTag-γPFD-Cys solution at twice the desired final concentration was prepared in phosphate buffer as described above. PEG-4MAL and fluorescent protein (both with and without SpyCatcher) solutions were prepared in phosphate buffer at 4 times the desired final

concentration. 25 μL of the PEG-4MAL and fluorescent protein solutions were mixed to yield 50 μL solution; this mixture was then blended with 50 μL SpyTag-γPFD-Cys solution by pipetting several times to form 100 μL of the fluorescent protein-incorporated hydrogel, which was allowed to cure at room temperature for 6 hours. Hydrogel erosion studies were performed as described above. To confirm the conjugation between SpyTag-γPFD-Cys and SpyCatcher-FPs, mixed samples were loaded onto Bolt 4-12% Bis-Tris SDS-PAGE gels (Invitrogen) containing Spectra BR protein ladder (Thermo Scientific). Separated protein bands were visualized by SimplyBlue staining (Invitrogen).

In order to study leaching of the fluorescent proteins, gels of 100-μL volume were formed and cured as described above, followed by addition of 900 μL phosphate buffer and incubation at room temperature. At each time point of measurement, a small aliquot of buffer was removed and the fluorescence was measured at the maximum emission peaks of mCerulean3 and mVenus (475 nm and 528 nm) using a Spectramax M2 plate reader (Molecular Devices) to determine the amount of leached proteins.

FRET measurements

Hydrogels containing the same amounts of mCerulean3 and mVenus were formed *in situ* on a black 96-well plate. Control hydrogels containing only one of the fluorescent proteins were also formed. The fluorescence was measured with the Spectramax M2 plate reader (Molecular Devices) using a 412-nm excitation, 430-nm cutoff filter and emission scan of 450 – 600 nm. A buffer blank was subtracted from all samples. FRET spectra were deconvoluted using the control spectra as references. The isolated mCerulean3 components of the FRET spectra as well as the control mCerulean3 spectra were integrated to calculate the fluorescence intensities. FRET efficiencies were calculated from the equation below:

$$\text{FRET efficiency } (\%) = (1 - \frac{I_{\text{DA}}}{I_{\text{D}}}) \times 100$$

where I_{DA} is the integrated fluorescence intensity from the decomposed FRET spectrum, and I_D is that calculated from the mCerulean3 spectrum. Spectral decomposition and integration were performed using a/e UV-Vis-IR Spectral Software 2.2 (Fluortools). Measurements were only made for the concentration range in which the fluorescence intensity increased linearly with the protein concentration.

Human pluripotent stem cell culture

Human embryonic stem cells (H9s, NIH Stem Cell Registry 0062) were subcultured in monolayer format on a layer of 1% Matrigel (354277, Corning) and maintained in Essen-

tial 8 medium (A1517001, ThermoFisher) during expansion. At 80% confluency, H9s were passaged using Versene solution (15040066, Thermo Fisher) and re-plated at a 1:8 split.

Viability assays

H9s were dissociated into single cells using Accutase solution (A6964, Sigma-Aldrich) and resuspended in Essential 8 medium containing 10 μM Y-27632 (Rock Inhibitor, 1254, Tocris). H9s were counted and resuspended at defined densities and mixed 1:1 with PEG-4MAL solution. Suspended H9s were mixed 1:1 with SpyTag-γPFD-Cys in a μClear 96-well plate (655090, Greiner Bio-One). At specific time points, wells with H9s in hydrogels were incubated in 250 μL of Calcein AM solution (C3100MP, Thermo Fisher) diluted 2,000 times from the stock solution using sterile PBS for 20 minutes. After staining, cells were imaged using a confocal microscope.

Confocal microscopy and image processing

Stained cultures were imaged with a 5x objective using an Opera Phenix automated confocal fluorescence microscope (Perkin Elmer) available in the High-Throughput Screening Facility at UC Berkeley. Laser exposure time and power were kept constant for a fluorescence channel within an imaging set. Fluorescent images were processed in ImageJ where background fluorescence was removed using a rolling bar radius algorithm and z-stacks were imported into 3D viewer for visualization [19].

MTT assay

Cells encapsulated in hydrogel were first cultured in 96-well plates as described above. At particular time points, 100 μL culture medium was replaced with new medium containing 1.1mM MTT (Thermo Fisher Scientific) and incubated for 4 hours at 37°C. Subsequently, 100 μL DMSO was added to each well, incubated for 10 min at 37°C, and the absorbance at 540 nm was measured using a Spectramax M2 plate reader.

4.4 Results

Design of the γPFD-PEG hybrid hydrogel

We chose the dimer-forming variant of γPFD (TERM) as the protein component of the hybrid hydrogel backbone. Since the distal regions of the helical coils corresponding to the N- and C-termini of each monomer are physically separate from the central barrel structure, engineering the tips of the helices to enable fusion with foreign proteins does not affect the dimeric assembly.

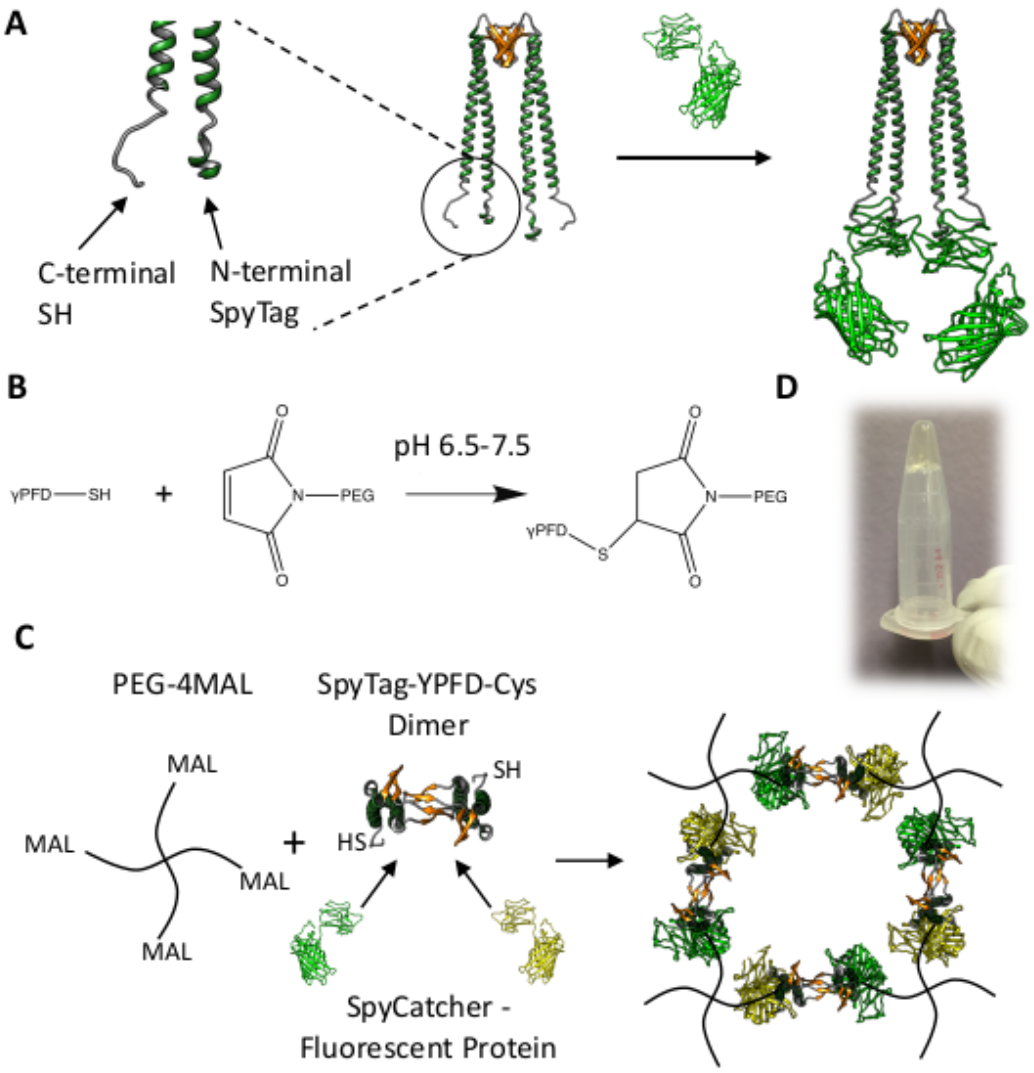

Figure 4.1: Design of γPFD-PEG hybrid hydrogel. (A) Cartoon depiction of the SpyTag-PFD-Cys dimer, before and after binding the fluorescent proteins through SpyTag-SpyCatcher interaction. N-terminal and C-terminal ends of one monomer are depicted in larger scale to the left. (B) Michael-type addition between thiol and maleimide groups. (C) Scheme of the bioorthogonal one-pot synthesis of the functionalized hybrid hydrogel network. Note that each dimer can contain either two of the same type of SpyCatcher-bound fluorescent protein, or one of each type (as shown). (D) Hybrid hydrogel formed in a microcentrifuge tube; the gel does not flow upon inverting the tube.

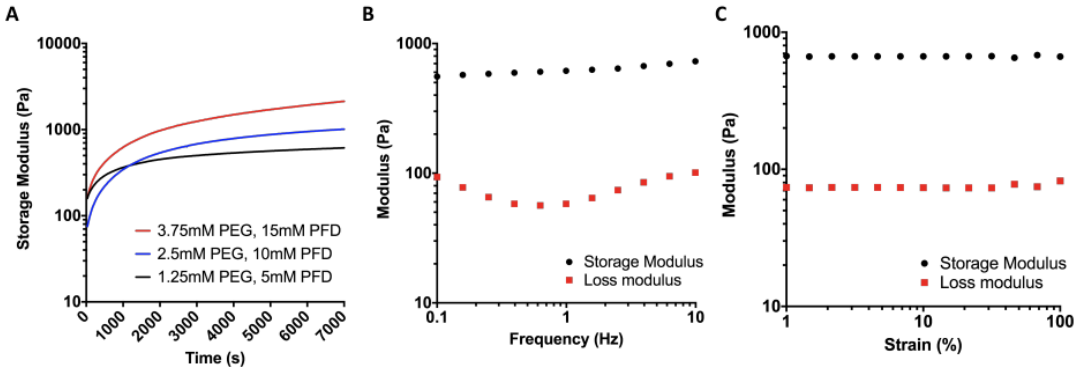

Figure 4.2: Rheology of γPFD-PEG hybrid hydrogel. (A) Change in storage modulus as a function of time after mixing the protein and polymer components. Measurements were performed at fixed frequency of 1 Hz and strain of 1%. (B) Frequency sweep of the hydrogel formed at 1.25 mM PEG and 5 mM γPFD, measured at fixed strain of 1%. (C) Amplitude sweep of the hydrogel formed at 1.25 mM PEG and 5 mM γPFD, measured at fixed frequency of 1 Hz.

The recently developed SpyTag-SpyCatcher chemistry allows for highly efficient and precise conjugation between proteins tagged with the 13-residue SpyTag peptide and the counterpart proteins fused to the 12 kDa SpyCatcher domain [20]. We genetically fused the SpyTag peptide to the N-terminal end of the γPFD monomer, and a cysteine residue to the C-terminal end to create SpyTag-γPFD-Cys, which was subsequently expressed and purified from an *E. coli* host. Thus, the dimers assembled from this modified subunit can scaffold two functional proteins of interest through SpyTag-SpyCatcher interaction, while forming chemical cross-links with polymer chains at both ends (Figure 4.1A, Figure S4.1). The polymer component that constitutes the hydrogel backbone was composed of maleimide-activated 4-arm polyethylene glycol (PEG-4MAL). The maleimide groups undergo Michael-type addition reactions to rapidly form cross-links with the C-terminal thiols of SpyTag-γPFD-Cys, (Figure 4.1B) resulting in formation of a regular two-component hybrid network (Figure 4.1C). The presence of the SpyTag domains in the hydrogel should enable efficient and specific incorporation of functional proteins fused to SpyCatcher. Thus, bioactive hydrogels can be formed in an orthogonal manner by mixing all three components (PEG-4MAL, SpyTag-γPFD-Cys and SpyCatcher-target protein) simultaneously in a single step.

Hydrogel formation and characterization

Gelation was observed upon mixing the solutions of PEG-4MAL and SpyTag-γPFD-Cys prepared in a physiological phosphate buffer at a 1:4 molar ratio (Figure 4.1D). Owing to

the fast kinetics of the thiol-maleimide reaction, the gel formed almost immediately after the two parts were combined, making manual pipetting impossible after a few seconds. The formed gel swelled up by 60% (mass increase) after being submerged in phosphate buffer for 48 hours (Figure S4.3).

We performed oscillatory rheology experiments to characterize the mechanical properties of the hybrid hydrogel. The time sweep results depicted in Figure 4.2A, which were measured at a fixed strain and frequency of 1% and 1 Hz, respectively, show that the storage modulus increased rapidly and reached a plateau after 2 hours of curing. As the total polymer and protein concentration was raised from 10 wt% (1.25 mM polymer and 5 mM protein) to 30 wt% (3.75 mM polymer and 15 mM protein), the plateau storage modulus increased from 600 Pa to 2000 Pa, demonstrating the tunability of the hydrogel's mechanical strength. The storage modulus remained largely constant over a broad range of frequencies from 0.1 to 10 Hz during the frequency sweep tests, (Figure 4.2B, Figure S4.2A) and the gel moduli remained constant up to ∼100% of the applied strain (Figure 4.2C, Figure S4.2B). Moreover, the storage modulus was higher than the loss modulus by roughly an order of magnitude over the entire range of measured frequencies and strains, indicating that the hybrid hydrogel displayed highly elastic behavior [21]. For subsequent experiments, PEG-4MAL was used at the final concentration of 1.25 mM, along with 5 mM of γPFD (total solid content of 10 wt%).

The stability of the hydrogels was investigated under aqueous conditions. Gels were cured for 6 hours and submerged in a phosphate buffer to test for the degree of erosion based on the amount of protein released to the solution. At room temperature, ∼25% of total protein was released after 2 weeks (Figure 4.3A). The hydrogel also exhibited stability at the elevated temperature of 37°C, which is required for applications such as cell culture or drug delivery (Figure 4.3A).

Synthesis of functional hydrogel

Having confirmed the mechanical tunability and stability of the "blank state" gel, we then synthesized bioactive hydrogels by incorporating SpyCatcher-bound functional proteins into the hybrid hydrogel network. As model proteins, fluorescent proteins mCerulean3 and mVenus were chosen for their stability, ease of quantification through fluorescence, and ability to interact with each other through fluorescence resonance energy transfer (FRET). The SpyCatcher domain was genetically fused to the N-terminal end of each fluorescent protein to create SpyCatcher-mCerulean3 and SpyCatcher-mVenus, which were subsequently expressed and purified from an *E. coli* host.

Theoretically, the maximum amount of SpyCatcher-bound protein that can be conjugated to the hydrogel is 5 mM, which is the molar equivalent of the available SpyTag domains. However, the fluorescent protein solution at such high concentration was too viscous to be

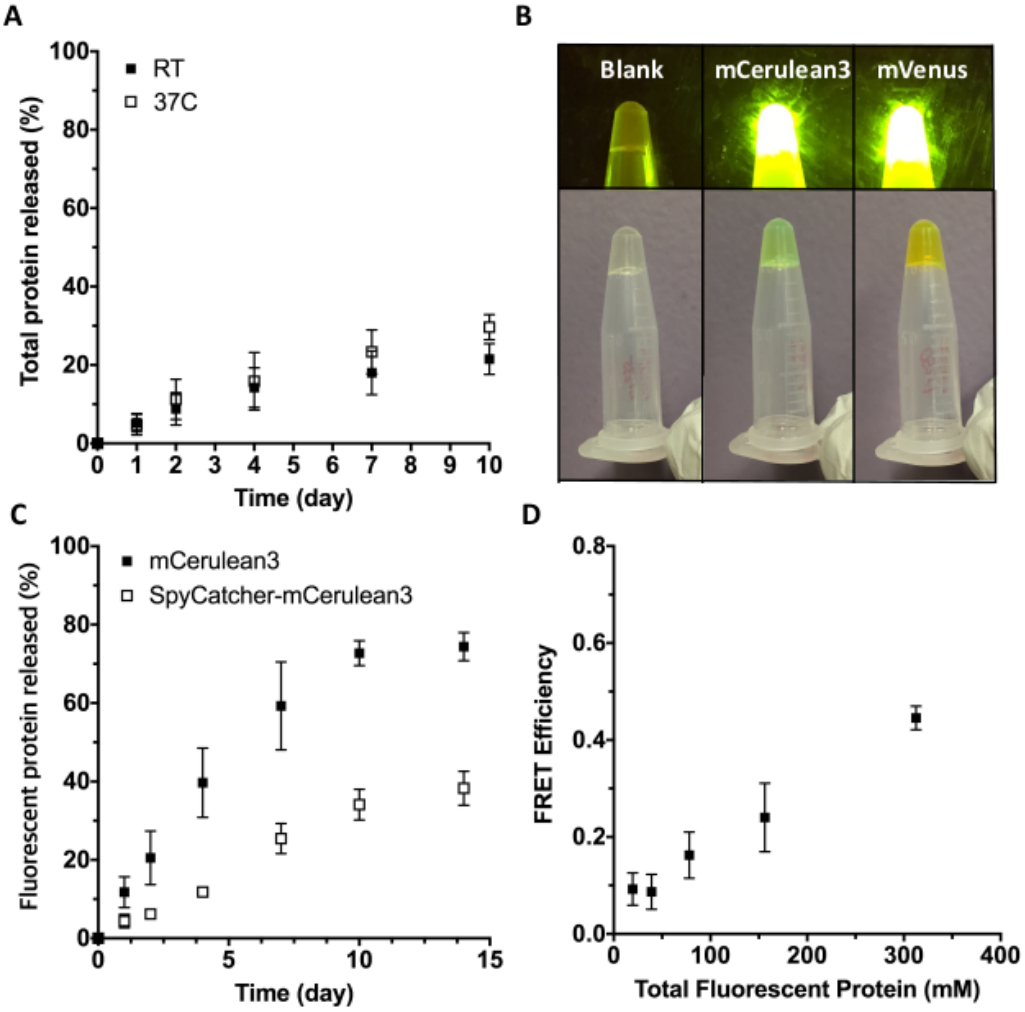

Figure 4.3: Stability of γPFD-PEG hybrid hydrogel under aqueous condition. (A) Total protein erosion profile of the hybrid hydrogels at room temperature and 37°C. (B) Hydrogels containing no fluorescent protein (left), mCeruluean3 (middle), and mVenus (right). The top images were taken under blue light, and the bottom images were taken under normal conditions. (C) Leaching profile of fluorescent proteins from the hybrid hydrogels formed with unmodified and SpyCatcher-fused mCerulean3. (D) FRET efficiencies of the hydrogels containing equal amounts of mCerulean3 and mVenus. The x-axis refers to the total fluorescent protein concentration, which was limited to a range showing a linear concentration-fluorescence behavior. All of the above experiments were performed at least twice, and the error bars represent the standard deviation. In some cases the error bars were smaller than the size of the symbols.

pipetted even before being mixed with the other components to form the gel. Thus, we chose the final concentration of the fluorescent proteins within the gel to be 1.25 mM, which corresponds to 25% of the total available conjugation sites. Upon mixing the three components PEG-4MAL, SpyTag-γPFD-Cys and either SpyCatcher-mCerulean3 and SpyCatcher-mVenus, hydrogels were formed with colors indicative of fluorescent protein incorporation, with fluorescence emission upon exposure to blue light (Figure 4.3B).

Isopeptide bond formation from the SpyTag-SpyCatcher interaction was confirmed by the upward shift of the protein bands from SDS-PAGE (Figure S4.4). The rheology, swelling behaviour, and total protein erosion profile of the gel containing SpyCatcher-mCerulean3 were comparable to those of the gel formed without any additional incorporation of proteins, indicating that the presence of SpyCatcher-mCerulean3 did not affect the viscoelastic properties of the hydrogel or its integrity in solution (Figure S4.5, S4.6). However, gels containing mCerulean3 without SpyCatcher fusion lost more than 70% of the total protein, suggesting that most of the non-covalently entrapped proteins leaked out of the gel (Figure S4.6). Examining the extent of leaching based on the fluorescence measurement of the buffer also yielded consistent results; ¿80% of the native mCerulean3 was lost to the buffer after two weeks, whereas only ∼35% of the SpyCatcher-mCerulean3 leached out (Figure 4.3C). These observations demonstrate that the γPFD-PEG hybrid hydrogel can provide a general scaffold to stably attach bioactive proteins.

To non-invasively investigate the distribution of functional proteins immobilized in the hydrogel, equal amounts of SpyCatcher-mCerulean3 and SpyCatcher-mVenus were incorporated together into the gels; their total concentration was varied within the range in which the fluorescence intensity increases linearly with the concentration. When mCerulean3 and mVenus are positioned in close proximity (¡ 10 nm), the excited mCerulean3 transfers energy to mVenus, which results in a decrease in mCerulean fluorescence emission at 475 nm and an increase of mVenus emission at 528 nm. As the total concentration of the fluorescent proteins increased from 20 μM to 320 μM, the FRET efficiency increased from almost zero to ∼45% (Figure 4.3D, S4.7, S4.8). These results suggest that multiple types of bioactive proteins can be simultaneously incorporated into the hydrogel, and that they can interact with each other if spaced in close proximity at high concentration. Thus, the hybrid hydrogel platform may prove particularly advantageous when close spatial proximity of multiple bioactive epitopes or enzymes is desired [22, 23].

3D cell culture in hydrogel

Finally, the hydrogel's ability to support growth of mammalian cells in 3D culture was assessed using human embryonic stem cells (hPSCs). The hydrogel was prepared by adding SpyTag-γPFD-Cys into a solution of PEG-4MAL with hPSCs and triturated with a micropipette to achieve adequate cell encapsulation. After visually confirming gel formation and cell encapsulation with phase contrast microscopy, E8 maintenance media supplemented

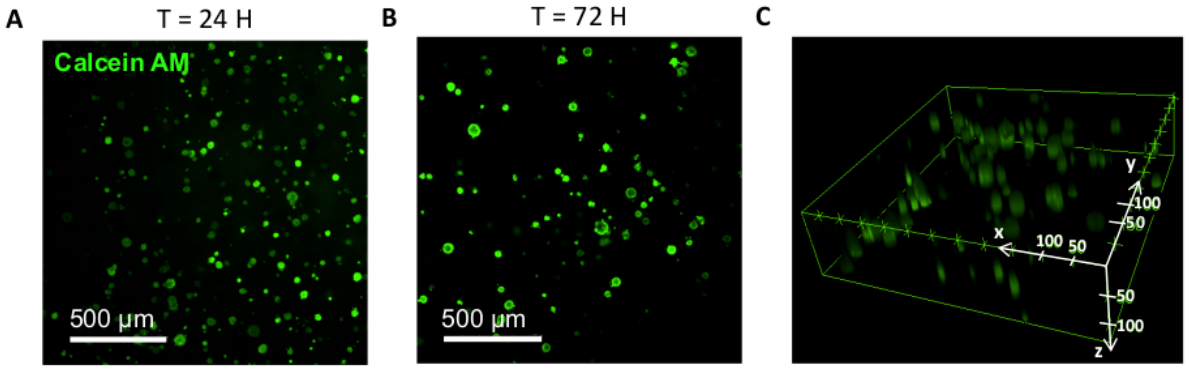

Figure 4.4: hPSC viability assay in hybrid hydrogel 3D culture system. Maximum intensity projection of confocal fluorescence microscopy stacks of human embryonic stem cells stained with calcein AM after (A) 24 hours and (B) 72 hours of encapsulation in hybrid hydrogel. (C) 3D depiction of viable hPSCs distributed across the hydrogel matrix at 24 hours.

with Y-27632 was added to the 3D cell cultures, which were then incubated at 37°C and 5% CO_2. Fluorescence-based live-cell staining as well as MTT assays revealed that ∼90% of the seeded cells remained viable over a 72-hour culture period (Figure 4.4A, 4.4B, S4.9. Further, the hPSCs were found to be distributed fairly evenly across x, y, and z dimensions of the gel (Figure 4.4C). Overall, these data support that our γPFD-based hybrid hydrogel is non-cytotoxic, and can potentially be applied as a fully defined 3D culture system for delicate cell types, such as human embroyonic stem cells.

4.5 Conclusion

In conclusion, we have developed a general strategy for the convenient, one-step immobilization of bioactive proteins into hydrogel. The gel network is formed by cross-linking PEG polymers with γPFD dimers via thiol-maleimide reaction, while the functional components are conjugated through SpyTag-SpyCatcher chemistry. Such bioorthogonal design allows for the one-step synthesis of the functionalized hydrogel by simply mixing three components under physiological conditions, providing an advantage over conventional methods to incorporate proteins into hydrogel networks. The resulting hydrogel is tunable in its mechanical properties, stable under aqueous conditions, and highly biocompatible. Furthermore, the strategy demonstrated here is applicable to any proteins or enzymes of interest by simple genetic fusion to the docking domain. Thus, we envision that our hybrid hydrogel can be used as a versatile platform for designing biomaterials for a wide variety of applications including multi-step biocatalysis and stem cell culture.

4.6 References

1. Webber, M. J., Appel, E. A., Meijer, E. & Langer, R. Supramolecular biomaterials. *Nature materials* **15,** 13–26 (2016).
2. Teixeira, L. S. M., Feijen, J., van Blitterswijk, C. A., Dijkstra, P. J. & Karperien, M. Enzyme-catalyzed crosslinkable hydrogels: emerging strategies for tissue engineering. *Biomaterials* **33,** 1281–1290 (2012).
3. Ghobril, C. & Grinstaff, M. The chemistry and engineering of polymeric hydrogel adhesives for wound closure: a tutorial. *Chemical Society Reviews* **44,** 1820–1835 (2015).
4. Li, Y., Rodrigues, J. & Tomas, H. Injectable and biodegradable hydrogels: gelation, biodegradation and biomedical applications. *Chemical Society Reviews* **41,** 2193–2221 (2012).
5. Naahidi, S. *et al.* Biocompatibility of hydrogel-based scaffolds for tissue engineering applications. *Biotechnology advances* **35,** 530–544 (2017).
6. Phelps, E. A. *et al.* Maleimide cross-linked bioactive peg hydrogel exhibits improved reaction kinetics and cross-linking for cell encapsulation and in situ delivery. *Advanced materials* **24,** 64–70 (2012).
7. Cambria, E. *et al.* Covalent modification of synthetic hydrogels with bioactive proteins via sortase-mediated ligation. *Biomacromolecules* **16,** 2316–2326 (2015).
8. Matsumoto, T., Isogawa, Y., Tanaka, T. & Kondo, A. Streptavidin-hydrogel prepared by sortase A-assisted click chemistry for enzyme immobilization on an electrode. *Biosensors and Bioelectronics* **99,** 56–61 (2018).
9. Ito, F. *et al.* Reversible hydrogel formation driven by protein–peptide–specific interaction and chondrocyte entrapment. *Biomaterials* **31,** 58–66 (2010).
10. Sui, Z., King, W. J. & Murphy, W. L. Protein-Based Hydrogels with Tunable Dynamic Responses. *Advanced Functional Materials* **18,** 1824–1831 (2008).
11. Esser-Kahn, A. P., Iavarone, A. T. & Francis, M. B. Metallothionein-cross-linked hydrogels for the selective removal of heavy metals from water. *Journal of the American Chemical Society* **130,** 15820–15822 (2008).
12. Ramirez, M., Guan, D., Ugaz, V. & Chen, Z. Intein-triggered artificial protein hydrogels that support the immobilization of bioactive proteins. *Journal of the American Chemical Society* **135,** 5290–5293 (2013).
13. Kopeček, J. & Yang, J. Smart self-assembled hybrid hydrogel biomaterials. *Angewandte Chemie International Edition* **51,** 7396–7417 (2012).
14. Sheldon, R. A. Enzyme immobilization: the quest for optimum performance. *Advanced Synthesis & Catalysis* **349,** 1289–1307 (2007).

15. Lim, S., Jung, G. A., Muckom, R. J., Glover, D. J. & Clark, D. S. Engineering bioorthogonal protein–polymer hybrid hydrogel as a functional protein immobilization platform. *Chemical communications* **55,** 806–809 (2019).

16. Gao, X., Lyu, S. & Li, H. Decorating a blank slate protein hydrogel: A general and robust approach for functionalizing protein hydrogels. *Biomacromolecules* **18,** 3726–3732 (2017).

17. Guan, D. *et al.* Two-component protein hydrogels assembled using an engineered disulfide-forming protein–ligand pair. *Biomacromolecules* **14,** 2909–2916 (2013).

18. Gao, X., Fang, J., Xue, B., Fu, L. & Li, H. Engineering protein hydrogels using SpyCatcher-SpyTag chemistry. *Biomacromolecules* **17,** 2812–2819 (2016).

19. Bankhead, P. Analyzing fluorescence microscopy images with ImageJ. *ImageJ* **1,** 195 (2014).

20. Zakeri, B. *et al.* Peptide tag forming a rapid covalent bond to a protein, through engineering a bacterial adhesin. *Proceedings of the National Academy of Sciences* **109,** E690–E697 (2012).

21. Partlow, B. P. *et al.* Highly tunable elastomeric silk biomaterials. *Advanced functional materials* **24,** 4615–4624 (2014).

22. Kim, Y. H., Campbell, E., Yu, J., Minteer, S. D. & Banta, S. Complete oxidation of methanol in biobattery devices using a hydrogel created from three modified dehydrogenases. *Angewandte Chemie International Edition* **52,** 1437–1440 (2013).

23. Pashuck, E. T. *et al.* Controlled sub-nanometer epitope spacing in a three-dimensional self-assembled peptide hydrogel. *ACS nano* **10,** 11096–11104 (2016).

Appendix

4.A Supporting Figures for Chapter 4

SpyTag-γPFD-Cys:
MAHIVMVDAYKPTKGSVNEVIDINEAVRAYIAQIEGLRAEIGRLDATIATLRQSLATLKSLKTLGE
GKTVLVPVGSIAQVEMKVEKMDKVVVAAAAAAAAELEYEEALKYIEDEIKKLLTFRLVLEQAIAE
LYAKIEDLIAEAQQTSEEEKAEEEENEEKAEC

mCerulean3:
MHHHHHHGGVSKGEELFTGVVPILVELDGDVNGHKFSVSGEGEGDATYGKLTLKFICTTGKLP
VPWPTLVTTLSWGVQCFARYPDHMKQHDFFKSAMPEGYVQERTIFFKDDGNYKTRAEVKFE
GDTLVNRIELKGIDFKEDGNILGHKLEYNAIHGNVYITADKQKNGIKANFGLNCNIEDGSVQLA
DHYQQNTPIGDGPVLLPDNHYLSTQSKLSKDPNEKRDHMVLLEFVTAAGITLGMDELYKGS

mVenus:
MHHHHHHGGVSKGEELFTGVVPILVELDGDVNGHKFSVSGEGEGDATYGKLTLKLICTTGKLP
VPWPTLVTTLGYGLQCFARYPDHMKQHDFFKSAMPEGYVQERTIFFKDDGNYKTRAEVKFEG
DTLVNRIELKGIDFKEDGNILGHKLEYNYNSHNVYITADKQKNGIKANFKIRHNIEDGGVQLAD
HYQQNTPIGDGPVLLPDNHYLSYQSKLSKDPNEKRDHMVLLEFVTAAGITLGMDELYKGS

SpyCatcher-mCerulean3:
MGHHHHHHGSAMVDTLSGLSSEQGQSGDMTIEEDSATHIKFSKRDEDGKELAGATMELRDS
SGKTISTWISDGQVKDFYLYPGKYTFVETAAPDGYEVATAITFTVNEQGQVTVNGKATKGSSK
GEELFTGVVPILVELDGDVNGHKFSVSGEGEGDATYGKLTLKFICTTGKLPVPWPTLVTTLSWG
VQCFARYPDHMKQHDFFKSAMPEGYVQERTIFFKDDGNYKTRAEVKFEGDTLVNRIELKGIDF
KEDGNILGHKLEYNAIHGNVYITADKQKNGIKANFGLNCNIEDGSVQLADHYQQNTPIGDGPV
LLPDNHYLSTQSKLSKDPNEKRDHMVLLEFVTAAGITLGMDELYK

SpyCatcher-mVenus:
MGHHHHHHGSAMVDTLSGLSSEQGQSGDMTIEEDSATHIKFSKRDEDGKELAGATMELRDS
SGKTISTWISDGQVKDFYLYPGKYTFVETAAPDGYEVATAITFTVNEQGQVTVNGKATKGSSK
GEELFTGVVPILVELDGDVNGHKFSVSGEGEGDATYGKLTLKLICTTGKLPVPWPTLVTTLGYGL
QCFARYPDHMKQHDFFKSAMPEGYVQERTIFFKDDGNYKTRAEVKFEGDTLVNRIELKGIDFK
EDGNILGHKLEYNYNSHNVYITADKQKNGIKANFKIRHNIEDGGVQLADHYQQNTPIGDGPVL
LPDNHYLSYQSKLSKDPNEKRDHMVLLEFVTAAGITLGMDELYK

Figure S4.1: Amino acid sequences of the recombinantly expressed proteins used in this study.

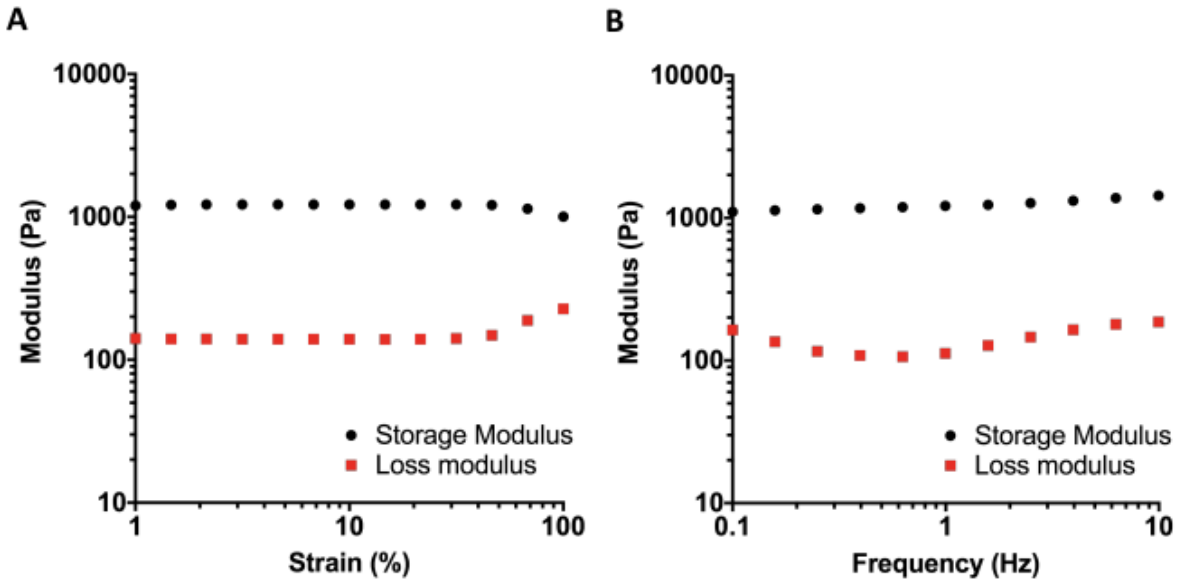

Figure S4.2: Rheology of γPFD-PEG hybrid hydrogel. (A) Frequency sweep of the hydrogel formed at 2.5 mM PEG and 10 mM γPFD, measured at fixed strain of 1%. (B) Amplitude sweep of the hydrogel formed at 2.5 mM PEG and 10 mM PFD, measured at fixed frequency of 1 Hz.

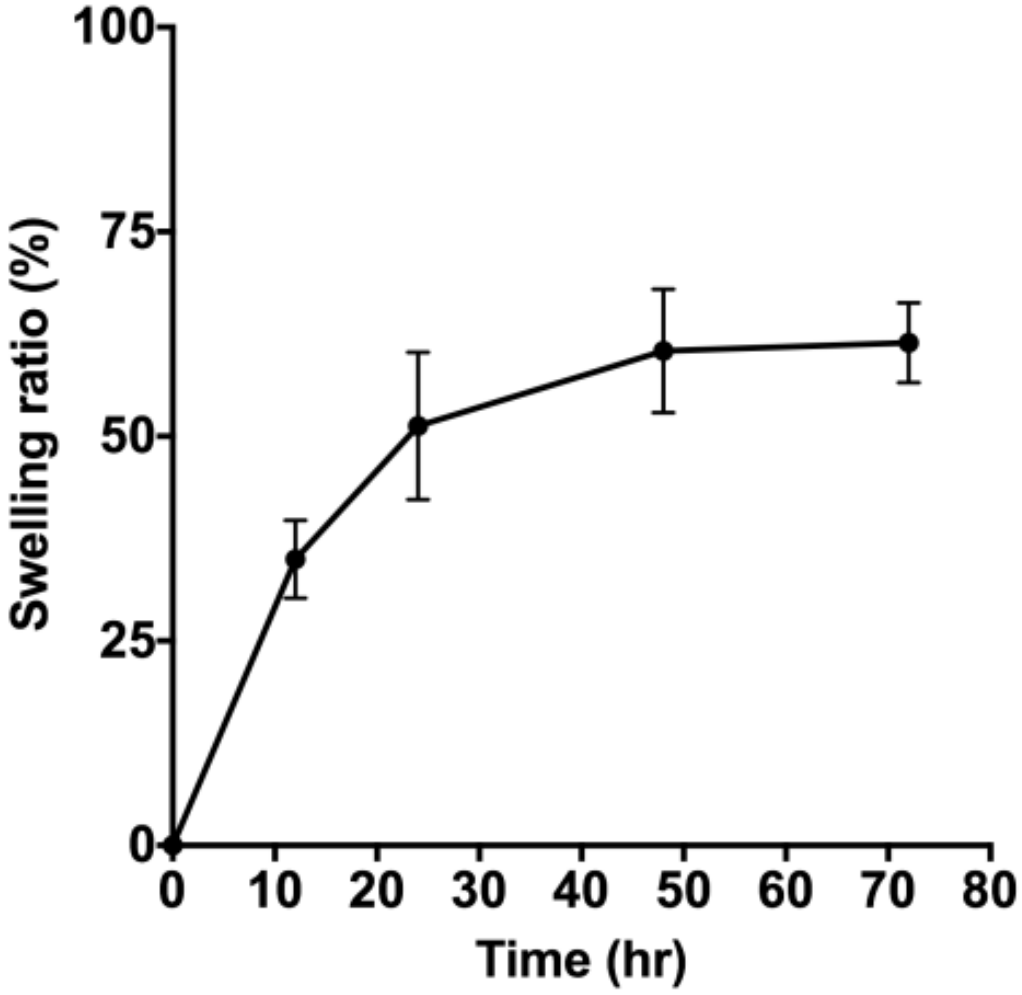

Figure S4.3: Swelling of the hybrid hydrogels formed at 1.25 mM PEG and 5 mM γPFD, after submerging the formed hydrogel in phosphate buffer. Experiments were performed at least twice, and the error bars represent the standard deviation (SD).

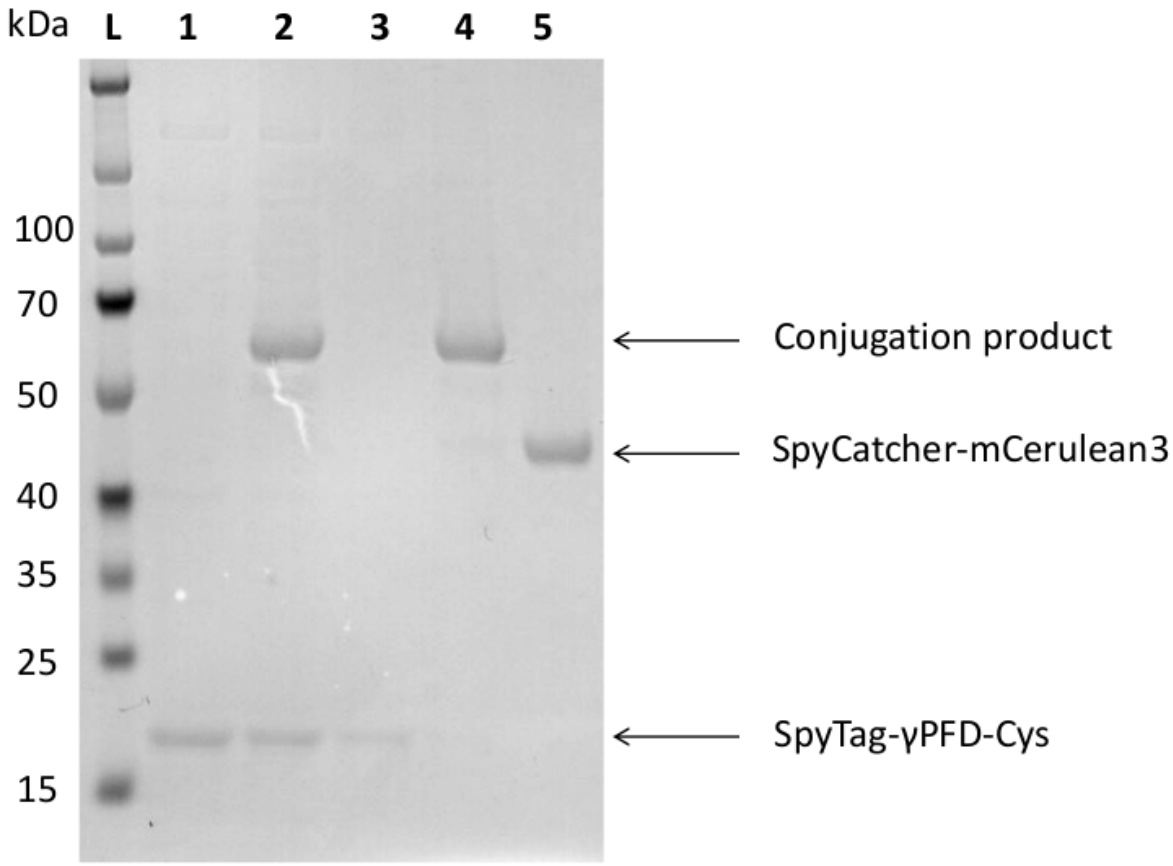

Figure S4.4: SDS-PAGE results showing the conjugation between SpyTag-γPFD-Cys (18 kDa) and SpyCatcher-mCerulean3 (40 kDa). Loaded samples were 8 μM γPFD (lane 1), 2 μM SpyCatcher-mCerulean3 mixed with 8 μM γPFD (lane 2), 2 μM γPFD (lane 3), 2 μM SpyCatcher-mCerulean3 mixed with 2 μM γPFD (lane 4) and 2 μM SpyCatcher-mCerulean3 (lane 5). Hydrogel samples could not be loaded onto SDS-PAGE, and thus diluted samples were used to confirm the conjugation.

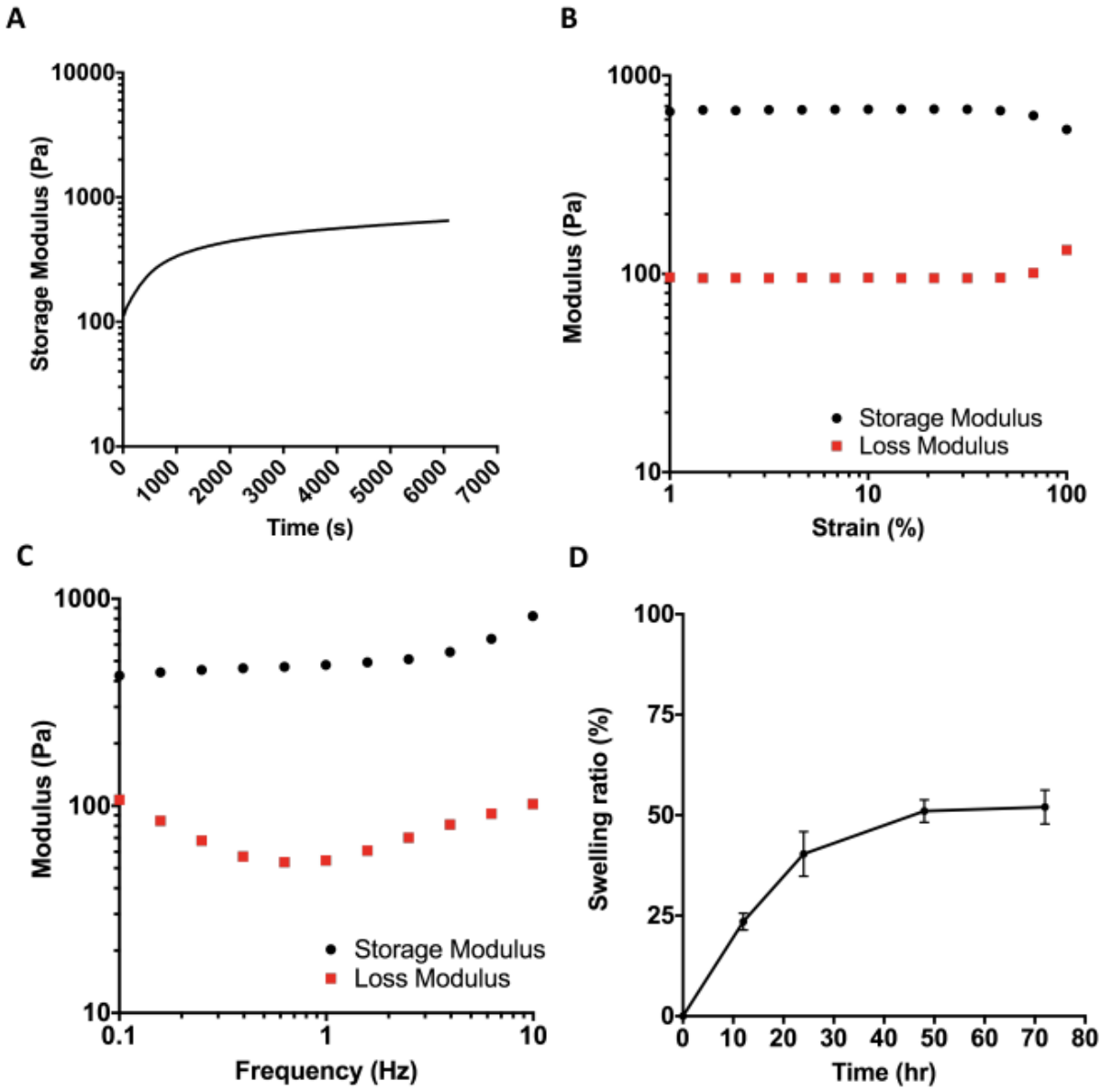

Figure S4.5: Properties of the functional hybrid hydrogels formed with 1.25 mM PEG and 5 mM PFD containing 1.25 mM SpyCatcher-mCerulean3. (A) Change in storage modulus as a function of time after mixing the protein and polymer components. Measurements were performed at fixed frequency of 1 Hz and strain of 1%. (B) Amplitude sweep of the hydrogel, measured at fixed frequency of 1 Hz. (C) Frequency sweep of the hydrogel, measured at fixed strain of 1%. (D) Swelling of the hydrogel after submerging in phosphate buffer. Experiments were performed at least twice, and the error bars represent the SD.

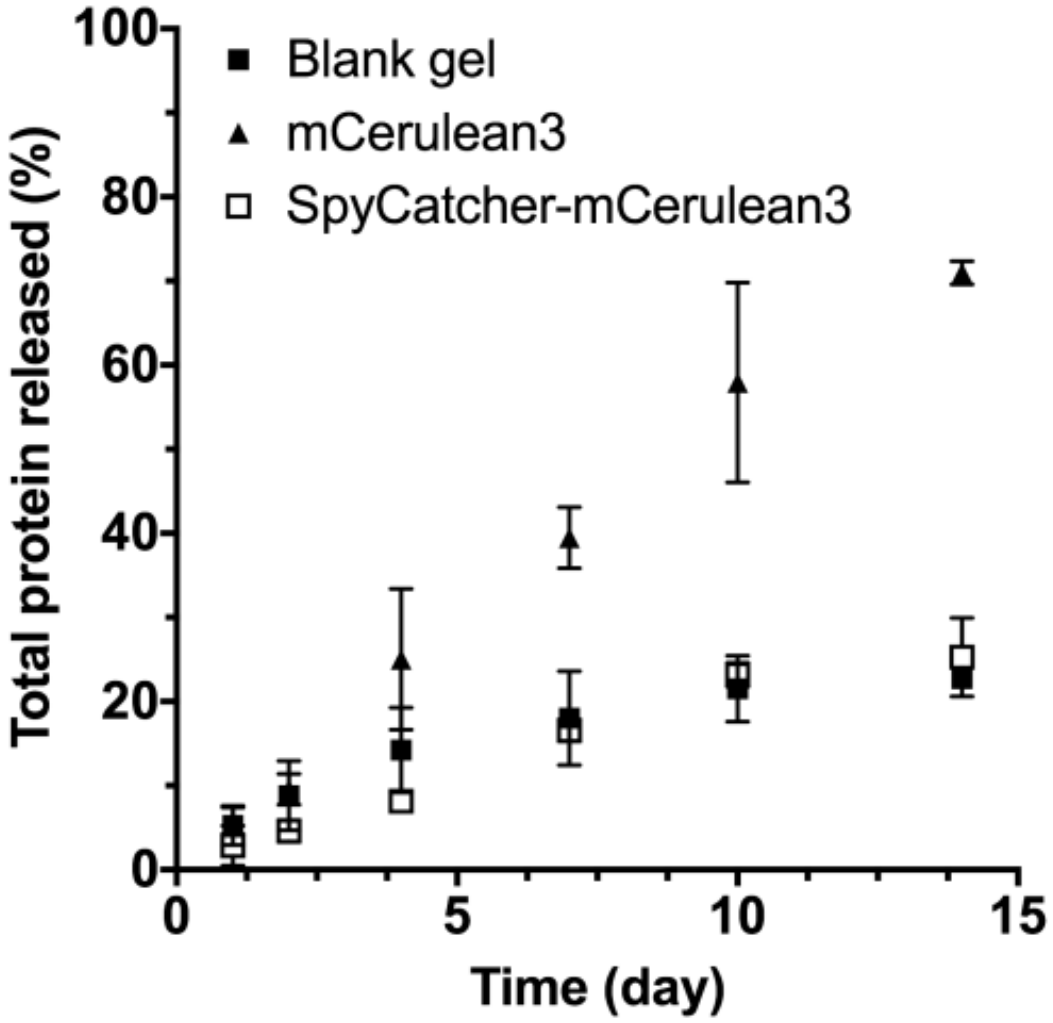

Figure S4.6: Total protein erosion profile of the hybrid hydrogels formed at 1.25 mM PEG and 5 mM γPFD without any fluorescent protein, with 1.25 mM native mCerulean3, and with 1.25 mM SpyCatcher-mCerulean3. Experiments were performed at least twice, and the error bars represent the SD.

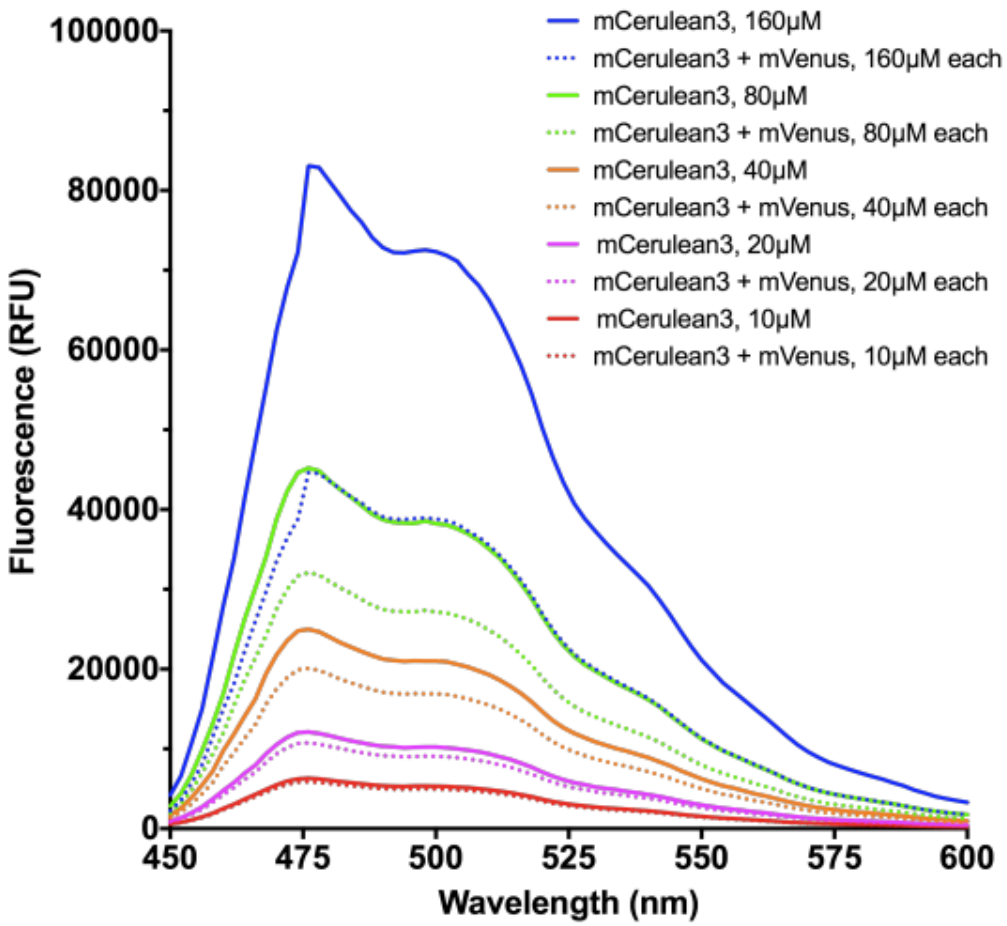

Figure S4.7: Emission spectra of the hydrogels containing both mCerulean3 and mVenus, compared to those containing only mCerulean3. Total fluorescent protein concentrations were varied within a linear concentration-fluorescence range. The samples were excited at 412-nm, using a 430-nm cutoff filter. Solid lines represent the emission spectra from the gels containing only mCerulean3. Dotted lines represent the mCerulean3 component of the decomposed emission spectra from the gels containing equal amounts of mCerulean3 and mVenus.

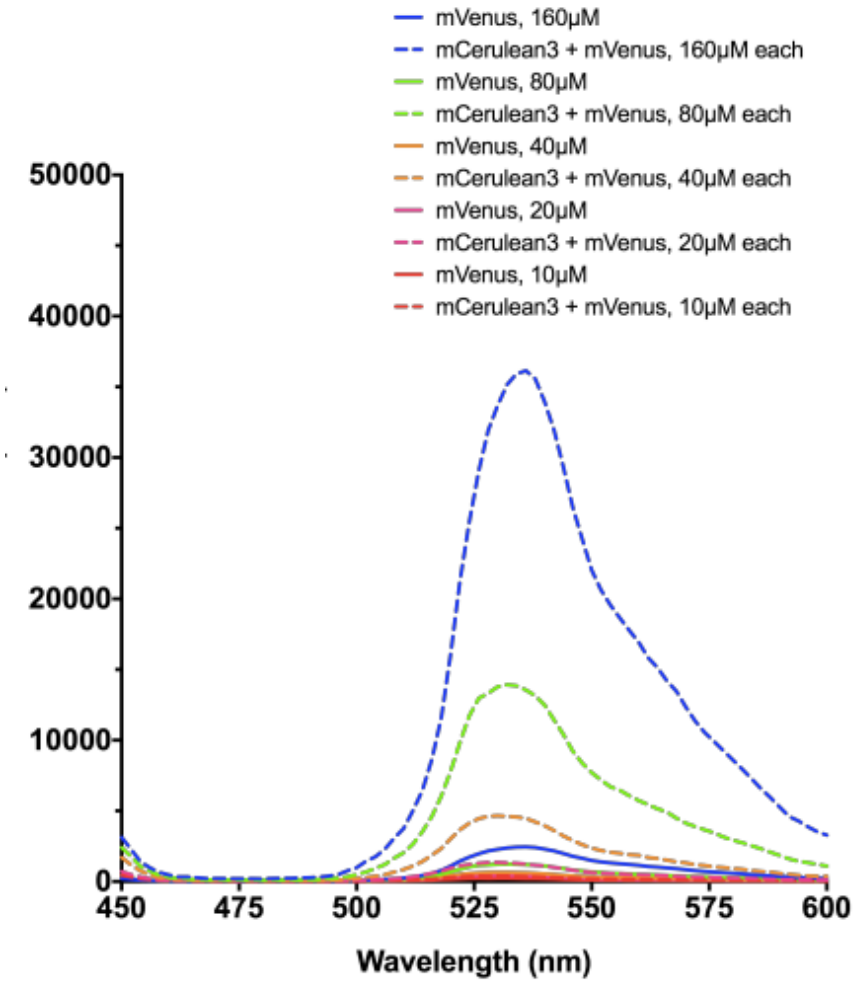

Figure S4.8: Emission spectra of the hydrogels containing both mCerulean3 and mVenus, compared to those containing only mVenus. Total fluorescent protein concentrations were varied within a linear concentration-fluorescence range. The samples were excited at 412-nm, using a 430-nm cutoff filter. Solid lines represent the emission spectra from the gels containing only mVenus; note that the signals are very low because mVenus without a donor (mCerulean3) cannot be excited at this wavelength. Dotted lines represent the mVenus component of the decomposed emission spectra from the gels containing equal amounts of mCerulean3 and mVenus.

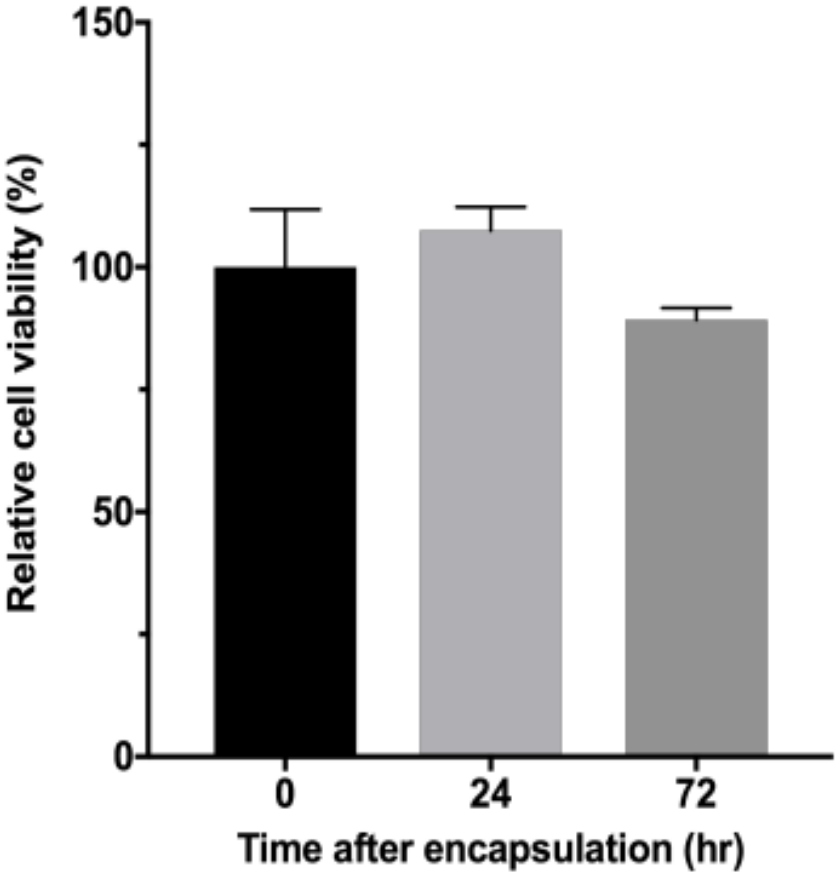

Figure S4.9: Viability of the hPSCs encapsulated in hydrogel over 72-hour culture period. Absorbance values at 540 nm were normalized to the value at time zero, which was measured immediately after gel formation. The error bars represent the SD from triplicate measurements. At 24 and 72 hours after encapsulation in hydrogel, relative cell viabilities were ∼100% and ∼90%, respectively. The results indicate that most of the seeded cells survived both the initial processing condition and subsequent culturing.